Synthesis of Nano-Particles in Flames

Johannessen, Tue

Publication date:
1999

Synthesis of Nano-Particles in Flames

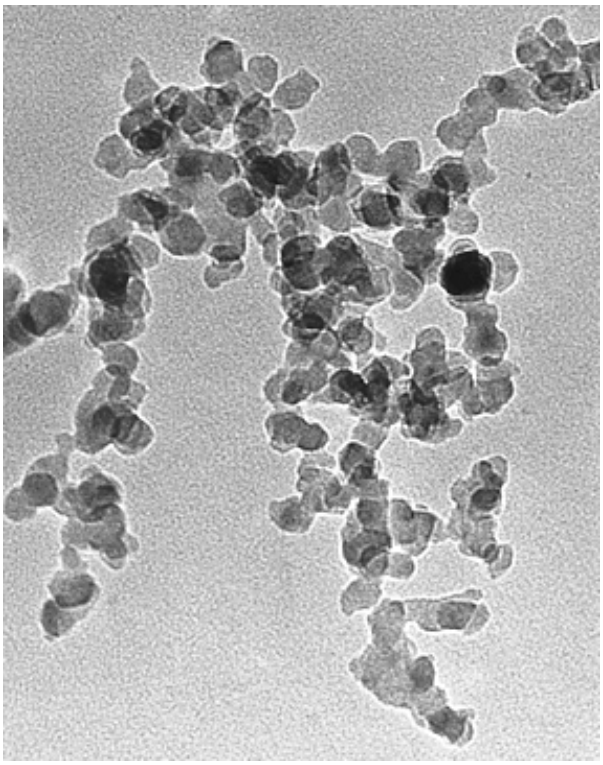

Tue Johannessen

1999

The Aerosol Laboratory
Department of Chemical Engineering
Technical University of Denmark
DK-2800 Lyngby, Denmark

Preface

This dissertation is a partial fulfilment of the requirements of the Ph.D degree. The work was mainly carried out at The Aerosol Laboratory, Department of Chemical Engineering, Technical University of Denmark with Dr. Hans Livbjerg as my supervisor. Part of the work was carried out at the Department of Chemical Engineering, University of Cincinnati, during a five-months stay (June-November, 1997) with Dr. Sotiris E. Pratsinis.

My sincere thanks to Hans Livbjerg for enthusiastic guidance, many discussions and for always providing an invaluable research foundation of chemical engineering background and overview. Also, my thanks to Stig Wedel for useful comments and discussions.

I would like to thank my past and present colleagues, Lars B. Nielsen, Sune K. Andersen and, in the final period, Morten T. Nielsen and Joakim R. Jensen for providing a pleasant working environment, personally as well as professionally. Assistance of the Department Workshop regarding the experimental setups and of Allan Henschel in doing transmission electron microscope analysis is gratefully acknowledged.

Regarding the visit at University of Cincinnati, the valuable outcome could not have been achieved without the energetic guidance of my temporary supervisor, Sotiris E. Pratsinis. Furthermore, thanks to Stavros Tsantilis, Jürgen Flesch and Andreas Schild for inspiring discussions and for making the five months at UC feel like home.

I am also grateful to Kari J. E. Lehtinen, VTT, for suggestions and discussions and to Philip Murtagh and David Jones from Fluent Europe for hardware/software support.

Finally, I would like to thank The Technical University of Denmark for providing the Ph.D-grant and the Danish Council of Technological Research (STFV) for financial support.

Tue Johannessen
Lyngby, Denmark
July 1998

Summary

The scope of this work is to investigate the synthesis of aluminum oxide particles in flames from the combustion of an aluminum alkoxide precursor.

A general introduction to particles formation in the gas phase is presented with emphasis on the mechanisms that control the particle morphology after the initial formation of the monomers. Among those are Brownian coagulation of particles and the coalescence mechanism where collided particles fuse together thereby forming a sphere. Some existing models in the field are presented and compared.

Two different burner systems are used in this study: A diffusion flame burner and a premixed burner with a precursor jet. The experimental setups and results are shown and discussed in detail. Alumina powder with specific surface area between 45 m^2/g and 190 m^2/g was obtained.

Temperature and flow fields of the flame processes are analysed by numerical simulations (Computational Fluid Dynamics) where the fundamental equation for flow, heat- and mass transfer are solved numerically in computational domains similar to the real systems.
A model describing the particle dynamics in the flame is coupled with the flow-field information in order to compute effluent particle characteristics, e.g. primary particle size and aggregate size. The accuracy of the model depends highly on the expression for the characteristic coalescence time for aggregates. The results indicate that the large variations in particle size and crystallinity are too complex to be described by a single activation energy expression.

Furthermore, the model is validated by comparison with experimental data of the flame synthesis of titania by combustion of $TiCl_4$ previously presented by Pratsinis et al. (1996).

The combination of particle dynamics and CFD simulations has proved to be an efficient method for the analysis of particle formation in flames. Good results for a wide range of operating conditions were obtained. Therefore, the method should be useful as a tool for the optimization and/or design of flame processes for particle production.

Resumé (summary in Danish)

Formålet med dette arbejde er at undersøge fremstillingen af aluminiumoxid partikler ved forbrænding af en aluminium-alkoxid forbindelse i flammer

Der indledes med en generel introduktion til partikeldannelse i gasfase med vægt på de mekanismer, som styrer morfologien af partiklerne efter dannelsen ved dekomponeringen af udgangsstoffet. Eksempler på disse mekanismer er koagulering ved Brownske bevægelser og sintring af aggregater bestående af flere mindre partikler, som resulterer i dannelse af større sfæriske partikler. Visse eksisterende modeller for disse processer præsenteres og sammenlignes.

To forskellige brændersystemer er anvendt i dette arbejde: En diffusionsflamme og en forblandet flamme med precursor jet. Laboratorieopstillinger og forsøgsresultater præsenteres og diskuteres. Der blev fremstillet Al_2O_3 partikler med specifikt overfladeareal mellem 45 og 190 m^2/g.

Temperatur- og strømningsbilleder i flammerne er undersøgt ved simulering (numerisk fluid dynamik), hvor de fundamental ligninger for strømning-, stof- og varmetransport løses numerisk i et matematisk netværk, som er identiske med de fysiske systemer.
Informationen om strømningsbillederne kobles med partikelmodellen, hvorved variable som f.eks. størrelse af primærpartikler og aggregatstørrelse i procesudgangen kan beregnes. Nøjagtigheden af modelberegningerne afhænger i høj grad af udtrykket for sintringen af partikler. Resultaterne tyder på, at sintringsprocessen er for kompliceret til at blive beskrevet med en enkelt aktiverings energi.

Modellen er yderligere efterprøvet ved sammenligning med eksperimentelle data fra fremstilling af titan-dioxid partikler ved forbrænding af $TiCl_4$ (Pratsinis et al., 1996)

Kombinationen af partikeldynamik med fluid-dynamiske beregninger har vist at være en effektiv metode til undersøgelse af partikelproduktion i flammer. Der er opnået gode resultater for et bredt spektrum af forsøgsbetingelser. Denne metode må derfor anses for at være værdifuld under optimering og/eller design af flammeprocesser til partikelproduktion.

Table of Contents

List of Symbols

The following symbols are used in the text most frequently.

a	Surface area of a particle or an aggregate [m^2]
a_s	Surface area of a completely coalesced (spherical) particle [m^2]
c_p	Specific heat capacity [J/mole/K] or [J/kg/K]
D_f	Fractal dimension of aggregates, dimensionless
$D_{i,m}$	Molecular diffusion coefficient for species *i* [m^2/s]
d_p	Primary particle diameter [m]
d_c	Particle collision diameter [m]
D_p	Particle diffusion coefficient [m^2/s]
E_A	Activation energy [J/mole]
f_D	Dilution ratio, dimensionless
$\boldsymbol{g}$	The gravitational acceleration vector [m/s^2]
h	Enthalpy [J/mole] or [J/kg]
$\boldsymbol{j}^t_i$	Turbulent mass flux vector of species *i* [kg/m^2/s]
J	Mass flux (kg/m^2/s]
$\boldsymbol{j}_i$	The molecular diffusive mass flux [kg/m^2/s]
k	Turbulent kinetic energy [m^2/s^2]
k_0	Parameter in expression for the characteristic coalescence time [m^{-4}/s]
k_b	Boltzmanns constant, $1.308 \cdot 10^{-23}$ J/K
k_c	Thermal conductivity [J/m/s/K]
Kn	Knudsen number
M	Molar mass [kg/mole]
m_i	Mass fraction of species *i*
m_p	Number of primary particles per group in an aggregate
m_{PM}	Mass fraction of the PM pseudo gas component
N	Particle number concentration pr. volume of gas [m^{-3}]
N_{mass}	Particle number concentration pr. mass of gas [kg^{-1}]
n_p	Number of primary particles in an aggregate
p	Pressure [Pa]
$\boldsymbol{q}$	Molecular diffusion flux of heat [J/m^2/s]
$\boldsymbol{q}^t$	Turbulent diffusion flux of heat [J/m^2/s]
r	Radial coordinate [m]
R	Gas constant = 8.314 J/mole/K
r_c	Particle/aggregate collision radius [m]
R_{ij}	Number of collisions pr. volume pr. time between particle *i* and *j* [$m^{-3}s^{-1}$]
r_p	Primary particle radius [m]
$\boldsymbol{s}$	Position in (*r*, *z*) space
S	Source term for heat or mass [J/m^3/s] or [kg/m^3/s]

S_A	Specific surface area [m^2/g]
S_h	Heat source term (chemical reactions, radiant heat absorption)
S_i	Net rate of production of species *i* per unit volume by chemical reactions
t	Time [s]
T	Temperature [K]
T_0	Parameter in expression for the characteristic coalescence time
T_D	Decomposition temperature for precursor [K]
$\boldsymbol{u}$	Velocity vector [m/s]
u_i	Linear velocity in the i-direction [m/s]
u_x'	Fluctuating component of the instant velocity in the x-direction [m/s]
v	Solid volume of a particle/aggregate [m^3]
v_{D0}	Molecular diffusion volume [m^3]
v_p	Primary particle volume [m^3]
w_{PM}	Total particle mass flow [kg/s]
x_i	i'th spacial direction
z	Axial coordinate [m]
∇	The differential operator nabla

Greek letters

α	Fraction of total particle mass flow
β	Collision frequency function [m^3/s]
ϵ	Dissipation rate of turbulent kinetic energy [m^2/s^3]
λ_g	The mean free path of the gas [m]
μ	Viscosity [kg/m/s]
μ_t	The turbulent viscosity [kg/m/s]
ρ	Density [kg/m^3]
σ	Surface tension [N/m]
$\boldsymbol{\tau}$	Stress tensor [$kg/s^2/m$]
$\boldsymbol{\tau}^{(t)}$	The turbulent momentum flux tensor [$kg/s^2/m$]
τ_f	Characteristic coalescence time [s]
ϕ	Solid volume fraction or a scalar in turbulence models

Subscripts

c	Collision
g	Gas
i	Component no.*i*, particle no. *i*, direction no. *i*
p	(Primary) particle
s	Spherical (e.g. a_s, the area of a spherical particle with equal solid volume)
t	turbulent
w	Wall property

Superscripts

´	Turbulent fluctuating value
¯	Time averaged value

$\log = \log_{10}$
$1\ \text{nm} = 1 \cdot 10^{-9}\text{m}$
$1\ \mu\text{m} = 1 \cdot 10^{-6}\text{m}$

Commonly used abbreviations

ATSB	Aluminum-tri-sec-butoxide
CFD	Computational fluid dynamics
CPC	Condensational particle counter
DMA	Differential mobility analyser
PC	Personal computer
POC	Points-of-Contact model for coalescence
RSM	Reynolds stress model
SA	Surface area
SMPS	Scanning mobility particle sizer
SSA	Specific surface area
TEM	Transmission electron microscope

1 Introduction

The manufacture of particles in flames is widely used in the industry. Several commodities like carbon black, fumed silica and titanium dioxide (titania) are produced in large scale flame processes. These powders are usually used as pigments in paints or as reinforcing agents in polymers (Pratsinis, 1998).

Particle formation in flames is a complicated process, involving both chemical reaction, transport phenomena and aerosol dynamics. Because of that, most processes are mostly empirically designed.

Since the early 1970's when Ulrich (1971) investigated the formation of TiO_2-particles in a premixed flame, the understanding of the flame process has come a long way. Still, predicting the properties of the effluent aerosol for a given flame process with a reasonable degree of accuracy is not possible.

This work is concentrated on the formation of aluminum oxide (alumina, Al_2O_3) particles in diffusion flames and in jets entering premixed flames.

Alumina powders have several applications ranging from cutting tools and heat- and wear-resistant materials to high temperature catalyst carriers and membranes but compared with e.g. titania it is still a more specialty type chemical manufactured on a smaller scale basis.

Micro-porous alumina membranes can be manufactured from nanometre-sized particles deposited on a porous support layer from a liquid suspension. However, when the particles are made in aqueous solution by the sol-gel technique, the crystal structure of the porous layer becomes unstable when heated for sintering or high temperature applications. The accompanying recrystallization results in a considerable decrease in specific surface area and an increase in pore size (Tranto, 1997). The synthesis of nanometre-sized alumina particles at high temperatures in flames provides an interesting alternative for producing particles with high thermal stability.

2 Methods for particle production in flames

Several types of flame processes have been used to synthesize alumina powders. Sokolowski et al. (1977) prepared mixtures of α-alumina and γ-alumina particles by combustion of aluminum-acetylacetonate ultrasonically sprayed from benzene-ethyl alcohol solution. Alumina particles with 20-80 % α-alumina were manufactured from combustion of $AlCl_3$ vapour with H_2-CO fuel in a combustion tube heated at 1200-1300 °C, (Sextl et al., 1990). The average particle size was rather large (150 nm). Wu et al. (1993) produced alumina particles in a turbulent free jet in a premixed CH_4/air burner. Here, the precursor was tri-methyl-aluminum.

Windeler et al. (1997) used a free jet in a premixed flame similar to the work Wu et al. (1993). They studied the effect of material properties (Niobium oxide/alumina/titania) on primary particle size and aggregate structure.

Diffusion flames have been used to investigate the effect of gas mixing in the flame synthesis of titania (Pratsinis et al., 1996). Operating conditions such as flame configuration and flow rates of fuel and oxidant have a significant impact on the specific surface area of the produced powder.

Irrespective of the differences between the processes mentioned above, the residence time/temperature history of the particles may be the most important factor for determining the particle characteristics in all flames.

For numerous references to various flame processes, see the review by Pratsinis (1998).

3 Aerosol dynamics in flames

This section provides an overview of the important processes during particle formation in flames. The path from precursor molecules to particles and aggregates is described.

3.1 Gas-to-particle conversion

Gas-to-particle conversion is the production of particles from individual atoms or molecules in the gas phase. In the following, both solid particles and droplets are referred to as particles. Usually, formation of particles or condensation on existing particles initiates when the gas is sufficiently supersaturated with respect to one or more components. This initial supersaturation can be obtained in several ways:

- By cooling.
- By a chemical reaction that generates atoms or molecules with low vapour pressure.

Several types of reacting systems exist:

- The injection of a precursor into a reaction zone.
- The ignition of a premixed reactant mixture, where the precursor is present in the mixture.
- The initiation of a reaction in a gas mixture by photolytic excitation.

Examples of the processes above are:

- The formation of fine mode combustion aerosols from chemical gas reactions in the combustion zone and/or by subsequent cooling of the flue gas.
- A flame reactor in which a metallic alkoxide compound or metal-halide is oxidized to Me_xO_y.
- The conversion of SO_2 to SO_3 by use of UV-light with NH_3 as catalyst (Christensen et al., 1995)

Figure 3.1 shows a schematic of the gas-to-particle path. The gas mixture reaches a state of supersaturation with respect to the B-molecules. Particle formation then takes place by either of the two following mechanisms.

Evaporation-condensation controlled homogeneous nucleation: For compounds with a "normal" vapour pressure level, like water, sulfuric acid or organic vapour, nucleation is controlled by formation of stable molecular clusters. For a given supersaturation, a critical cluster size exists. Above this size, the cluster is stable and will continue to grow. Below the critical size, the cluster is unstable and will evaporate. The dynamics of the cluster size

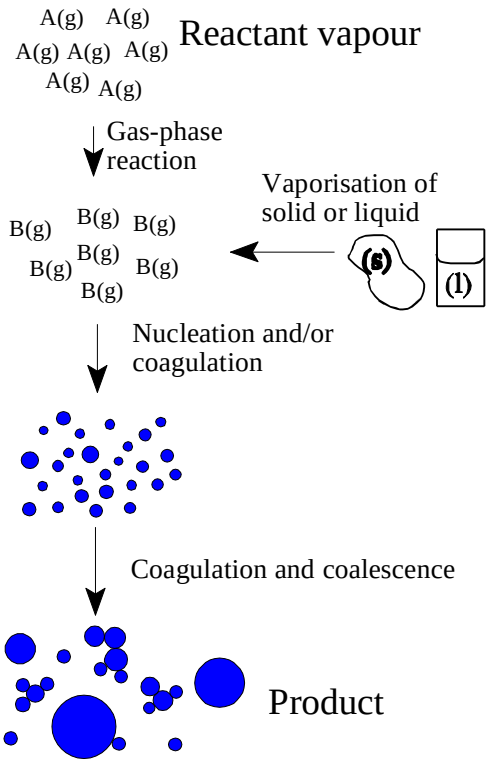

Figure 3 *The fundamentals of gas-to-particle conversion.*

distribution is determined by the condensation/evaporation processes. If the supersaturation is sufficiently high, the critical cluster size is small and homogenous nucleation will occur. This mechanism is called evaporation-condensation controlled because of the influence of evaporation and condensation dynamics on the cluster distribution below the critical size (e.g. Friedlander, 1977).

Collision controlled nucleation: If the supersaturation is extremely high, two molecules sticking together form a stable particle. Particle formation/growth is then controlled by collision of B-molecules. This is the case if the gas molecule, B(g), has an extremely low vapour pressure. Metal oxides like Al_2O_3, TiO_2, SiO_2 etc. belong to the group of compounds with very low vapour pressure (e.g. Ulrich, 1971; Bolsaitis et al., 1987).

3.2 Coagulation by Brownian motion

For an aerosol, the coagulation of particles becomes important at high concentrations, above say 10^6 cm^{-3}. It is highly influenced by the concentration, with a second order dependence of concentration on the coagulation rate. For a system of initially spherical 0.2 μm particles, the

time to reduce the concentration by a factor of 10 by Brownian coagulation is approximately 2 min when the initial concentration is 10^8 cm^{-3} and 20 min when the initial concentration is 10^7 cm^{-3} (Friedlander, 1977).

Particle collisions occur because of differences in particle velocities and several different mechanisms may lead to that. Brownian motion, velocity gradients in shear flow systems and external force fields are among the important mechanisms. Examples of external force fields are gravity or electric fields.

Velocity gradients in shear flow cause particles to move relative to each other, which can result in collision. This is also the case for gravitational settling. Large particles will "catch up" with smaller particles because of a difference in terminal velocity. For particles in the submicron range, Brownian motion is the dominant coagulation mechanism with a collision frequency function several orders of magnitude larger than those of gravitational settling and shear (Christensen, 1995).

For Brownian motion, collision rates are calculated as a function of particle size and concentration.

The number of collisions, R_{ij}, per unit time per unit volume between two different particle classes of size d_{p1} and d_{p2} with corresponding volume-based concentrations N_1 and N_2 is given by (Friedlander, 1977)

$$R_{12} = \beta(d_{p1}, d_{p2}) N_1 N_2 \qquad \textbf{(3)}$$

In this equation, $\beta(d_{p1}, d_{p2})$ is the collision frequency function, having the dimension [$m^3 s^{-1}$].

For particles much smaller than the mean free path of the gas, the collision frequency function is calculated from the kinetic theory of gases. In the continuum regime, the collision rate is calculated from the continuum diffusion theory.

Fuchs (1964) proposed an interpolation form of the collision frequency function, β, which is valid over the entire particle size range:

$$\beta = 2\pi(D_{p1}+D_{p2})(d_{p1}+d_{p2})\left(\frac{d_{p1}+d_{p2}}{d_{p1}+d_{p2}+2g_{12}} + \frac{8(D_{p1}+D_{p2})}{\bar{c}_{12}(d_{p1}+d_{p2})}\right)^{-1} \qquad \textbf{(3)}$$

$$g_{12} = (g_1^2 + g_2^2)^{1/2} \quad , \quad g_i = \frac{\left(d_{pi} + l_i\right)^3 - \left(d_{pi}^2 + l_i^2\right)^{3/2}}{3 d_{pi} l_i} - d_{pi} \quad , \quad l_i = \frac{8 D_{pi}}{\pi \bar{c}_i} \qquad \textbf{(3)}$$

$$\bar{c}_{12} = (\bar{c}_1^{\,2} + \bar{c}_2^{\,2})^{1/2} \quad , \quad \bar{c}_i = \left(\frac{8 k_b T}{\pi m_{pi}} \right)^{\frac{1}{2}} \quad , \quad m_{pi} = \rho_{pi} \frac{\pi}{6} d_{pi}^3 \ , \ i = 1,2 \qquad \textbf{(3)}$$

In equations 3.2 to 3.4, d_{p1} and d_{p2} are the diameters of the colliding particles, $\bar{c}_i$ is the mean particle speed. The particle diffusion coefficient, D_p, is calculated from the Stokes-Einstein expression with a Cunningham slip correction factor by Phillips (1975):

$$D_{pi} = \frac{k_b T}{3 \pi \mu d_{pi}} \left[\frac{5 + 4 Kn_i + 6 Kn_i^2 + 18 Kn_i^3}{5 - Kn_i + (8 + \pi) Kn_i^2} \right] \qquad \textbf{(3)}$$

The Knudsen number, *Kn*, is the ratio of the mean free path of the gas, λ_g , and the particle radius:

$$Kn_i = \frac{2 \lambda_g}{d_{pi}} \quad , \quad \lambda_g = \frac{\mu_g}{\rho_g} \sqrt{\frac{\pi M_g}{2 R T_g}} \qquad \textbf{(3)}$$

where μ_g, ρ_g and M_g are the gas viscosity, gas density and molar mass of the gas respectively. The mean free path of the gas is the average distance travelled by a molecule between two successive collisions.

3.3 Structure of flame generated aggregates

In aerosol terms, an aggregate is a cluster of many smaller primary particles. Aggregates are formed by collisions, usually caused by Brownian motion. The strength of the bond between the individual particles in the aggregate may vary.

In flame processes, the primary particles are formed at high temperature, whereas most of the aggregate formation by coagulation takes place at lower temperature. This type of process often results in complicated dendritic structures, which can be described by a power-law relationship between the solid volume of the aggregate and a characteristic aggregate size: The collision radius, r_c. The collision radius is equal to the true radius for a solid sphere. For an aggregate of

volume v consisting of n_p identical primary particles of volume v_p , the collision radius is calculated by (Matsoukas and Friedlander, 1991):

$$r_c = r_p\left(\frac{v}{v_p}\right)^{\frac{1}{D_f}} = r_p(n_p)^{\frac{1}{D_f}} \quad \textbf{(3)}$$

D_f is called the fractal dimension, which is equal to three for a solid sphere. For D_f decreasing below a value of three, the corresponding aggregate becomes increasingly dendritic. For cluster-cluster coagulation, a value of D_f close to 1.8 has often been observed (Kaplan and Gentry, 1988).

The rate of Brownian coagulation for aggregates can be computed by replacing the particle diameter in equations 3.2 to 3.6 by the collision diameter, d_c, where $d_c = 2r_c$ (Matsoukas and Friedlander, 1991). For a dendritic aggregate, a collision diameter equal to the diameter of a sphere with the same solid volume would underestimate the effective collision diameter for the aggregate.

3.4 Coalescence of aggregates

During the first stages of the nucleation/coagulation process, the particles are very small. When two particles/aggregates collide and stick together, they can either retain their individual shape or fuse/diffuse together thereby forming a spherical particle. The latter sintering process is usually called coalescence. The driving force for coalescence is the surface tension, which strives to reduce the aggregate surface area. The surface Gibbs free energy, which governs the coalescence process, is at minimum when the particle has relaxed to a spherical shape. Growth and coalescence can occur simultaneously and two limiting cases exist.

Collision limited growth: The time between two successive collisions is much larger than the time needed for the aggregate to coalesce to a sphere. An aggregate formed by collision between smaller particles/aggregates immediately reshapes to a spherical particle.

Coalescence limited growth: For this case, coalescence is slow compared with growth by coagulation. The resulting particles form complex, dendritic aggregates, each consisting of numerous smaller primary particles.

3.5 Models for particle dynamics

When particle coagulation and coalescence occur simultaneously and with comparable characteristic times, one can no longer assume a system of spherical particles. Two models both describing the basic particle morphology are presented below.

3.5.1 Self-preserving size distribution model

Lehtinen et al. (1996), proposed a model for particles undergoing simultaneous coagulation and sintering. The model will be presented below along with some references to the single model elements. The purpose of the model is to estimate the average aggregate (solid) volume, v, and the primary particle volume, v_p, of aerosol particles/aggregates. Collision between particles/ aggregates increases the particle volume but not the primary particle size. Coalescence reduces the excess surface area, which affects v_p without any effect on v.

The aggregate volume is calculated using the self-preserving theory for fractal-like structures by Matsoukas and Friedlander (1991). Assuming a constant fractal dimension, the following expression for the change in v is obtained:

$$\frac{dv}{dt} = \frac{1}{2}\alpha\sqrt{\frac{6k_bT}{\rho_p}}\left(\frac{3v}{4\pi}\right)^{\frac{1}{6}}\varphi n_p^{2/D_f-2/3} \qquad \textbf{(3)}$$

where k_b is Boltzmann's constant, T is the temperature, ρ_p is the particle (solid) density, ϕ is the volume fraction of particulate matter (volume of particles/volume of gas), n_p is the average number of primary particles per aggregate and α is a constant depending on D_f. The relation for α is approximated by:

$$\alpha = 6.548 + 112.1 \cdot D_f^{-7.883} \qquad \textbf{(3)}$$

An equation describing the final stages of coalescence of a slightly non-spherical particle was derived by Friedlander and Wu (1994):

$$\frac{da}{dt} = -\frac{1}{\tau_f}(a - a_s) \qquad \textbf{(3)}$$

where a is the surface area of the particle and a_s is the surface area of a solid sphere with

the same volume. The characteristic coalescence time, τ_f, base on solid state diffusion is given by (Friedlander and Wu, 1994):

$$\tau_f = \frac{3k_b T v}{64\pi D_s \sigma v_{D0}} \quad \textbf{(3)}$$

where v is the particle volume, σ is the surface tension (assumed constant), D_s is the solid state diffusion coefficient and v_{Do} is the molecular volume for diffusion.
The notation with subscript "*f*" arrises from fusion. Subscript "*c*" is not used to avoid confusion with characteristic collision time, τ_c.
Lehtinen et al. (1996) modified equations 3.10 and 3.11 to give a more realistic expression for the coalescence of large aggregates.

For an aggregate consisting of n_p primary particles, equation 3.10 is assumed to hold for a group of m_p particles within the aggregate, where m_p-1 is the average coordination number of a primary particle. The entire aggregate thus consists of n_p/m_p groups of m_p particles. All groups will coalesce with the same rate irrespective of the number of groups within the aggregate, which for the whole aggregate yields:

$$\frac{da}{dt} = \frac{n_p}{m_p}\left(-\frac{1}{\tau_{fm}}(a_m - a_{sm}) \right) \quad \textbf{(3)}$$

Here a_m is the surface area of m_p primary particles and a_{sm} is the surface area of a solid sphere with the same solid volume as m_p primary particles. The characteristic sintering time τ_{fm} for the group of m_p particles follows from equation 3.11:

$$\tau_{fm} = \frac{3k_b T m_p v_p}{64\pi D \sigma v_{D0}} \quad \textbf{(3)}$$

When the number of primary particles, n_p, is smaller than m_p, m_p becomes equal to n_p and equations 3.12 and 3.13 reduces to 3.10 and 3.11.
This is an improvement for the sintering prediction of aggregates. Coalescence in a large aggregate does not occur "from one end to another" but between the neighbouring primary

particles in the aggregate.

The physical picture behind this approach is illustrated below.

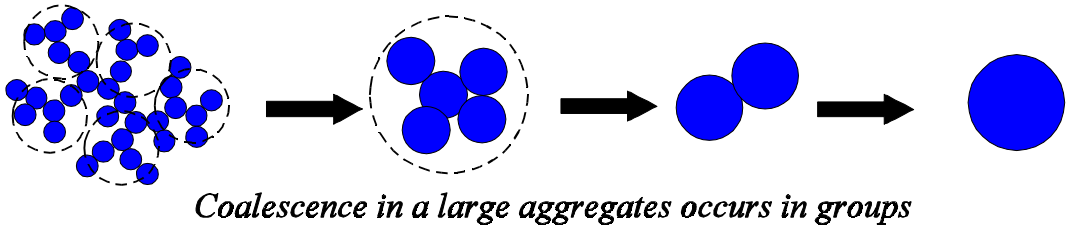

Figure 3 *Coalescence of aggregates as proposed by Lehtinen et al. (1996). The coalescence of large aggregates occurs group-wise.*

In complete form, the primary particle growth is calculated by (Lehtinen et al., 1996):

$$\frac{dv_p}{dt} = \begin{cases} \dfrac{64\pi D_s \sigma v_{D0}}{k_b T}\left(m_p^{-1} - m_p^{-4/3}\right), & n_p = \dfrac{v}{v_p} > m_p \\ \dfrac{64\pi D_s \sigma v_{D0}}{k_b T}\left(n_p^{-1} - n_p^{-4/3}\right), & n_p = \dfrac{v}{v_p} \le m_p \end{cases} \qquad \textbf{(3)}$$

This equation is written in terms of primary particle volume, v_p, and not the aggregate surface area.

Equation 3.8 and 3.14 are coupled through $n_p = v/v_p$. The two equations are solved with initial values of primary particle volume, $v_{p,o}$ and the average aggregate volume, v_o. Furthermore one must know the functions $T(t)$ and $\phi(t)$ and the material properties ρ_p, σ, $D_s(T)$ and v_{Do} and the fractal dimension D_f. The function, $T(t)$, is the temperature profile and $\phi(t)$ is a measure of dilution as a function of time. For a system without dilution, $\phi(t)$ is a constant.

3.5.2 Monodisperse model

One can also describe the evolution of primary particle size and number concentration of aggregates by the approximative model of Kruis et al. (1993). This model predicts the average primary particle size well, as verified by comparison with the detailed sectional models of aggregate dynamics by Xiong and Pratsinis, 1993.

The important assumptions for the model are:

- All aggregates contain the same number of equally sized primary particles

- The initial monomers are stable particles. If the monomers are molecules, then the supersaturation must be well above the point where evaporation-condensation controlled homogeneous nucleation is significant.

The model comprises differential equations with the number concentration, *N*, the surface area, *a*, and the volume, *v*, of the aggregates as dependent variables, i.e.:

$$\frac{dN}{dt} = -\frac{1}{2}\beta N^2 \qquad \textbf{(3)}$$

where β is the collision frequency function and *t* is time. The particle concentration, *N*, is per unit volume of gas.

The surface area of an aggregate, *a*, increases by coagulation and decreases by coalescence:

$$\frac{da}{dt} = -\frac{1}{N}\left(\frac{dN}{dt}\right)a - \frac{1}{\tau_f}\left(a - a_s\right) \qquad \textbf{(3)}$$

where a_s is the surface area of a spherical particle with the same solid volume as the aggregate and τ_f is a characteristic sintering time, which depends on aggregate size and gas temperature. The growth rate of the aggregate volume, *v*, is proportional to the rate of coagulation:

$$\frac{dv}{dt} = -\frac{1}{N}\left(\frac{dN}{dt}\right)v \qquad \textbf{(3)}$$

The evolution of particles follows 3.15 to 3.17 with N_0 and v_0, the concentration and volume, respectively, of the initial monomers as initial values. The initial value for *a* is $6v_0/d_{p0}$, where d_{p0} is the diameter of the initial monomer. The primary particle size for any values of *a* and *v* is $d_p = 6v/a$, and the number of primary particles in an aggregate is $n_p = v/v_p$, where v_p is the primary particle volume.

3.5.3 Differences between the two models

The main differences between the two models are:

- The Structure-Dependent Self-Preserving model (SDSP) is derived based on the collision frequency function for particles in the free molecule regime.
- The Structure-Dependent Monodisperse (SDM) model neglects the spread of the size distribution but the collision frequency function can be calculated for particles either in

the free molecule or the continuum regime.

- The present SDM-model calculates the coalescence rate of a large aggregate as a rate for the entire aggregate. The SDSP-model uses a rate based on coalescence of small groups of neighbouring primary particles. The SDM-model can however be modified to include this aspect.

In both models, the dependence of structure is accounted for by the fractal dimension, D_f.

In the initial part of the particle formation process in the flame, the particles are in the free molecule regime, but once particles/aggregates grow to beyond 50 nm in size, deviations from the free molecule theory are unavoidable. The mean free path of a gas at normal pressure and temperature is approximately 65 nm.

The SDSP-model will deviate from the real system when particles are no longer much smaller than the mean free path of the gas whereas the SDM-model deviates from the real system because of an underestimation of the decay of particle concentration. The latter is caused the coagulation rate of particles of size d_{p1} and d_{p2} , which is at a minimum, when d_{p1} is equal to d_{p2} (e.g. Seinfeld, 1986).

Kruis et al. (1993) showed that the total particle concentration calculated by the SDM-model compared with a two-dimensional sectional model deviated less than 40% after a concentration decay of seven orders of magnitude.

3.5.4 The characteristic coalescence time

An important parameter in both of the models above is the characteristic coalescence time, τ_f. The coalescence of nano-sized particles is a complicated process, highly influenced by particle size and temperature. The coalescence mechanism is a mixture of surface diffusion, grain boundary diffusion, solid state diffusion and viscous flow. Viscous flow is only significant above or close to the melting point of the particles. An estimate of the order of magnitude of τ_f can be obtained from (Lehtinen, 1997):

$$\tau_f \approx r_p^{\,m} / C(T) \qquad \textbf{(3)}$$

where r_p is the particle radius and *C(T)* is a temperature function (Table 3.1). The functional form of *C(T)* depends on the coalescence mechanism.

Table 3.1 *Model parameters for estimation of characteristic coalescence times for different coalescence mechanisms (Lehtinen, 1997).*

Coalescence mechanism	C(T)	m
Viscous flow	$\frac{3\sigma}{2\mu}$	1
Evaporation-condensation	$\frac{6\sigma p M^{3/2}}{\sqrt{2\pi}\rho_p^2 (RT)^{3/2}}$	2
Lattice diffusion/ Bulk diffusion	$\frac{64 D_b \sigma M}{\rho_p R T}$	3
Surface diffusion	$\frac{225 \delta D_s \sigma M}{\rho_p R T}$	4
Grain boundary diffusion	$\frac{192 w D_b \sigma M}{\rho_p R T}$	4

σ = surface tension	R = gas constant	ρ = particle density
μ = viscosity	T = temperature	D = diffusion coefficient
p = pressure	δ = surface layer thickness	(l = bulk, s = surface
M = molar mass	w = grain boundary width	and b = grain boundary)

Most expressions for τ_f encountered in the literature are based on an assumed diffusion mechanism. The choice of a diffusion mechanism determines the value of the activation energy and dependence of particle size on the coalescence rate.

Several expressions, mostly empirically based on table 3.1, have been proposed for τ_f for different materials. In some cases, information from table 3.1 is used to predict coalescence rates based on "known" physical parameters. In other cases the τ_f -expression is the subject for parameter fitting. In the section regarding the self-preserving model, equation 3.11 shows an expression for τ_f for the case of solid state diffusion. Uncertainties in the physical parameters involved such as surface tension, diffusion vacancy volume, grain boundary width and various activation energies tend to counteract reliable results.

For aluminum oxide particles, the surface diffusion may not be determined by the surface diffusion coefficient of pure alumina. The surface, in the presence of water, is most likely covered with hydroxyl groups (Peri, 1960). Oberlander (1984) reports that the rate of calcination of alumina is affected by the composition of the surrounding air. In the presence of water vapour, the surface area during calcining decreases more than in dry atmosphere. Therefor we expect the presence of water to influence the coalescence rate.

Lunden (1995) reported a drastic change in coalescence rate for silicon particles when oxygen by accident contaminated the silicon particles. Furthermore, the results showed that surface diffusion was the dominant coalescence mechanism for silicon.

Surface diffusion might be the dominant coalescence mechanism for nano sized particles independent of the material involved. In the nano size range, a large fraction of the molecules are located at the surface. Furthermore, the high curvature at the surface makes the surface molecules even more mobile.

Based on the considerations above, it seems unlikely, that the coalescence of aggregates accurately can be predicted based on literature data for physical properties. Another approach is to use the experimental data with the model and adjust the coalescence parameters to match the data. The parameters for the coalescence rate can then be used for a similar system to predict particle dynamics for different operating conditions.

4 Laboratory equipment

The experiments with the diffusion flame burner are carried out at University of Cincinnati during a 5-month stay. All other experiments are carried out at the Aerosol Laboratory at the Technical University of Denmark.

4.1 The burners

The essential part of this work is the design of the burners in which the particles are produced. Two entirely different burners are used. One is a premixed flame with a precursor jet, the other diffusion flame burner. They are both described below.

4.1.1 Premixed flame with a free jet

The premixed flame with a free jet is a modification of the burner used by Wu et al. (1993) and Windeler et al. (1997). A drawing of the burner is shown on figure 4.1. The combustion reaction takes place just above the flame arrestor, which is a metal plate with small holes to distribute the premixed fuel and oxidant, e.g. methane and air, evenly and to prevent flashback.

The distribution of holes in the arrestor is shown on figure 4.2. The diameter of the arrestor is 4 cm and the height is 0.5 cm.

A minor pressure-drop through the arrestor yields a well-distributed flow of the feed gasses.

The precursor is fed to the flame through the jet entering the flame in the centre of the arrestor. The gaseous precursor is diluted in a carrier gas, e.g. nitrogen. To prevent condensation of the precursor inside the burner, the jet tube is contained in a heated brass jacket all the way to the burner mouth. The brass jacket has a heating element and a thermocouple inserted and the temperature of the jacket is kept constant by a temperature controller.

The flame reactants are fed to the burner through the spacing between the burner wall and the outer side of the brass jacket through small holes to ensure high degree of mixing between fuel and oxidant. All reactant gases then flow through the arrestor to the flame zone.

An important modification of the premixed burner is the quenching ring above the flame used for rapid cooling of the flame product gasses. It consists of a hollow metal ring with two internally separated spaces: One for the quenching air and one for cooling water. The quenching air, which is particle-free atmospheric air, flows horizontally into the hot gasses upstream from the flame through five small nozzles, each 1mm in diameter.

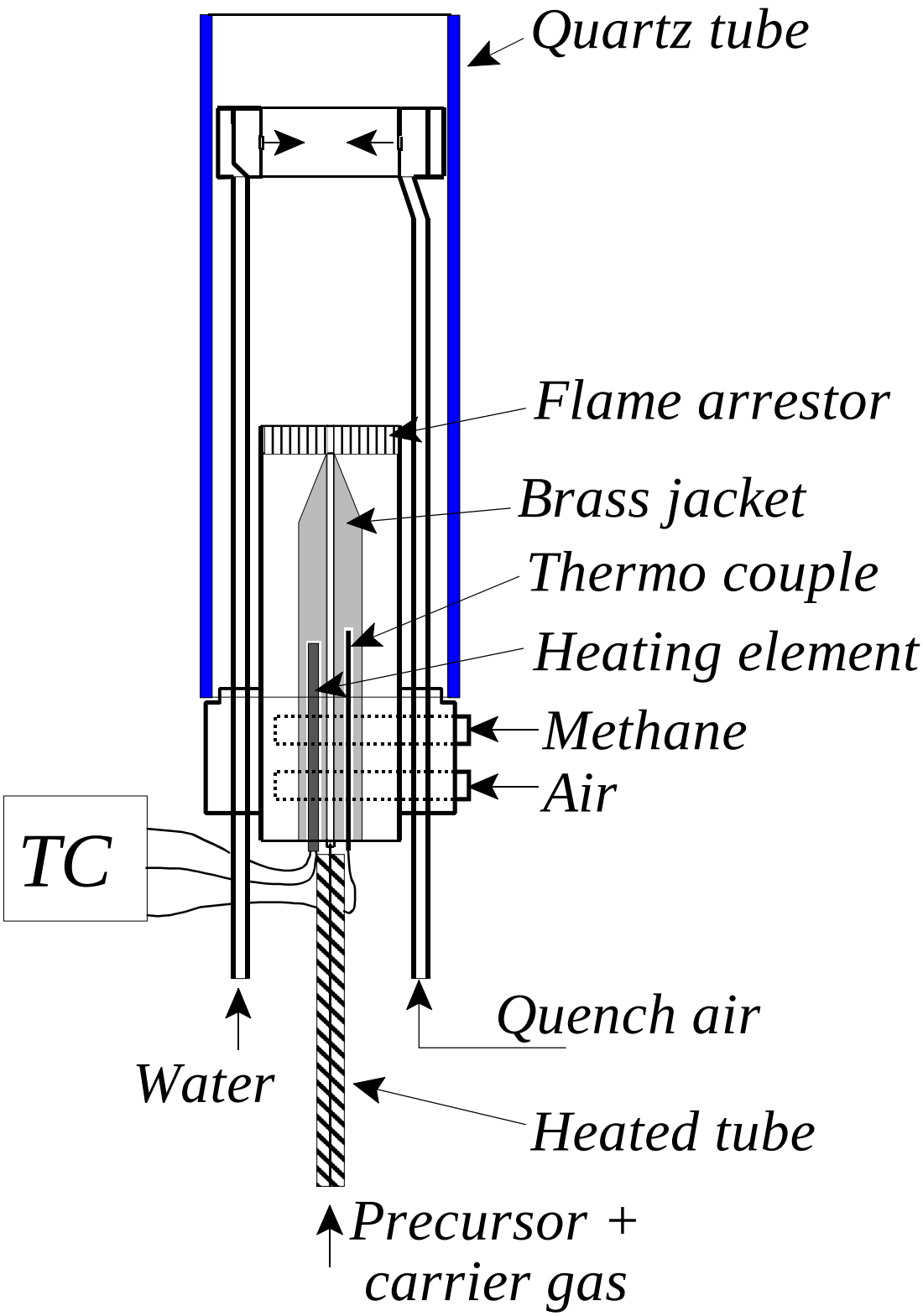

Figure 4 *A schematic of the burner consisting of a premixed flame and a free jet. (TC = temperature controller).*

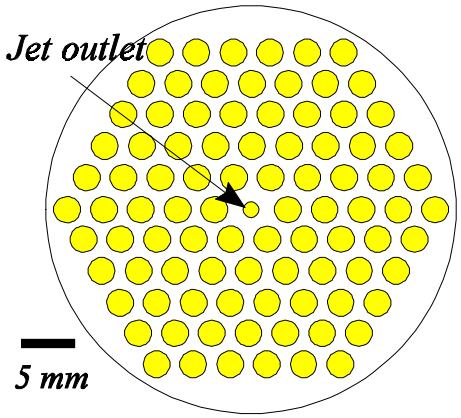

Figure 4 *Top view of the flame arrestor. The precursor flows in the centre jet. All other holes are for the fuel mixture.*

A 3D drawing of the quenching device is shown on figure 4.3. Three tubes are connected to the quenching ring: Quenching air inlet and cooling water inlet and outlet. The three tubes support the ring and the tubes can slide vertically. This enables the quenching to take place at different heights above the flame.

The purpose of the cooling water is to avoid that the hot combustion gasses heat the metal ring to the flame temperature level. This could raise the temperature of the quenching air

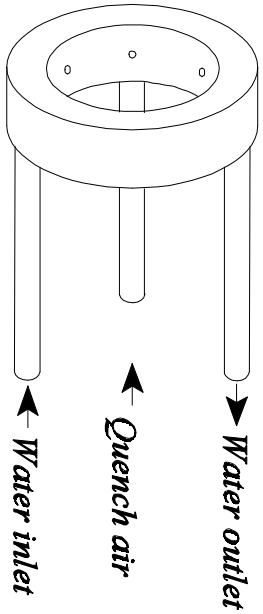

Figure 4 *A 3D drawing of the quenching device. The inlets are: Quenching air and cooling water*

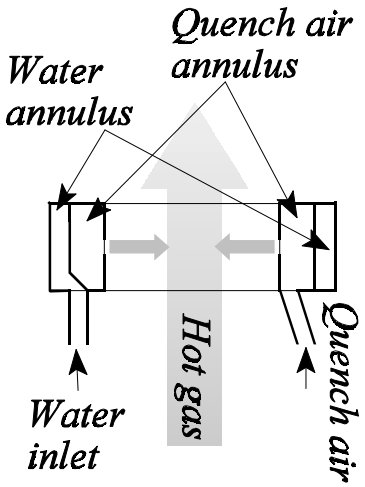

Figure 4 *Side view of the quenching device. The cooling water flows in the outer annulus, quenching air flows in the inner annulus and exits through five small nozzles into the combustion product gases.*

significantly. The result of quenching would then only be dilution, not a temperature drop. A cross section view of the quenching ring is shown on figure 4.4. The separation of the internal space for cooling water and the quench air is clearly seen. The quenching device at the injection point provides a rapid cooling of the upcoming hot combustion gasses and the particle containing jet. Particle coalescence, as described above, is highly dependent on temperature, and the objective of the quenching is to disrupt all particle coalescence at a specific point. Furthermore, the dilution provided by the quenching air will lower the coagulation rate of aggregates above the quenching point.

The important parameters to be investigated are the flow rate of quenching air and the vertical position of quenching. Especially the influence of those parameters on the aggregate structure, i.e. primary particle size and aggregate size is of interest. As shown on figure 4.1, the flame, jet and quenching ring are enclosed in a quartz tube, which is sealed at the bottom and open at the top. In that way the flame is not disturbed by the surroundings. In the experiments by Wu et al. (1993) and Windeler et al (1997), the bottom of the chimney was not sealed thus allowing outside air to cool and dilute the product gasses/particles.

The particles generated in the present burner are used for subsequent formation of porous membranes that must not be polluted by alien particles from the surrounding air. This is avoided by sealing the chimney at the bottom.

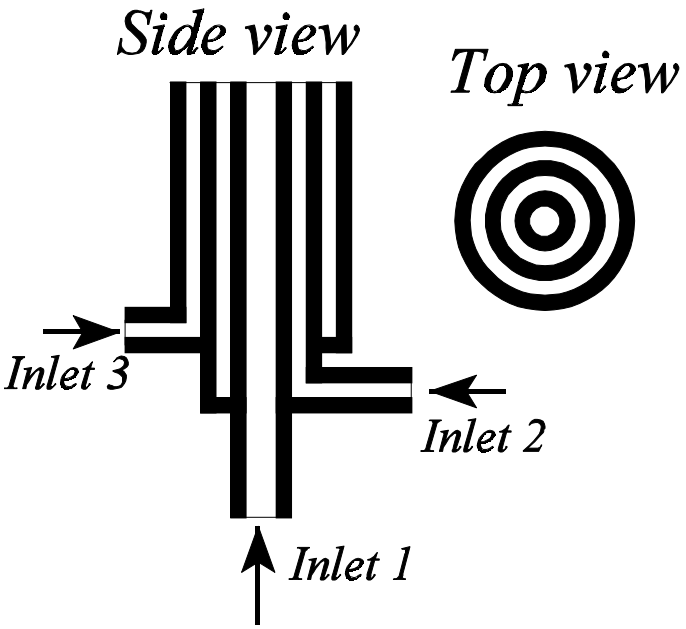

Figure 4 *The Diffusion flame burner consists of three concentric quartz tubes.*

4.1.2 Diffusion flame burner

The diffusion flame burner consists of three concentric quartz tubes. The inner tube has an outer diameter of 4 mm and the spacing between the following tubes is 1 mm. All tubes have a wall thickness of 1 mm (Vemury and Pratsinis, 1995). The feed gasses flow in the central tube and in the spacing between the surrounding tubes.

Figure 4.5 shows a side- and top-view of the burner. The length of the tubes from above Inlet 3 to the burner mouth is approximately 10 centimetres. This ensures that the velocity profiles in each tube/annulus has sufficiently large residence time to develop the velocity profiles fully. The inlet gasses are methane, air and carrier gas with the precursor. Different combinations of the feed gasses and the burner inlets are possible. Changing these combinations has shown to affect the specific surface area of flame produced titania particles significantly (Pratsinis et al., 1996).

4.1.3 Precursor

Examples of volatile aluminium containing precursors are: $AlCl_3$, $Al(CH_3)_3$ and Al-tri-sec-butoxide. In the present work, the aluminum alkoxide compound, Al-tri-sec-butoxide (ATSB), is chosen as precursor. ATSB is not as unstable and hazardous as other volatile aluminum compounds, but the vapour pressure is lower than those of $AlCl_3$ and $Al(CH_3)_3$. Therefore,

heating to 120-160 °C is necessary to obtain adequate production rates of alumina powder.
To avoid condensation of the precursor in the tubes, heating above the dewpoint is necessary. However, to minimize the thermal decomposition, the temperature must be kept below 200°C. Below approximately 200°C and in inert atmosphere, ATSB is stable (Haanappel et al., 1994). Even at low temperature, it decomposes when water vapour or oxygen is present.
An expedient procedure for feeding a liquid precursor to the flame is to saturate an inert carrier gas with the precursor in a bubble bottle heated to a temperature level, where the precursor has the desired vapour pressure. The equipment for this saturation is presented below in the description of the experimental setups.
Data for ATSB are listed in Appendix A.

4.2 Experimental setups

The experimental setups used in connection with the two burners will be presented separately. The main difference is of course the burner, but the accessories are not identical, since the experiments were carried out in both the US and Denmark. The experimental part at the Technical University of Denmark includes all work on the premixed burner. A separate setup was constructed for the diffusion flame burner during a five-month stay at The Chemical Engineering Department, University of Cincinnati with Dr. Sotiris Pratsinis as temporary supervisor. However, a few additional experiments with the diffusion flame were carried out at Technical University of Denmark after the return from Cincinnati. For those experiments, the diffusion flame burner was connected to the setup already constructed at the Technical University of Denmark.

4.2.1 Premixed flame setup

In the initial part of this work, an experimental setup with the premixed burner was designed. Though the precursor, ATSB, was believed to be less dangerous compared with other aluminum precursors, great care was taken in the design phase to prevent contact between the saturator bottle and the flame.

Figure 4.6 shows the experimental setup as it was initially created. The premixed burner is as described above. The saturator unit was constructed to protect the person operating the equipment from any type of explosion originating from thermal decomposition of ATSB, which is contained in two bubble bottles in series. The bottles are placed in a compartment made of stainless steel, which is sealed of from the ambient air. In the compartment, an inert gas, nitrogen, is recirculated past the bubble bottles and a heating element. The nitrogen temperature is kept constant by a temperature controller connected to a thermocouple placed in the heating zone. The temperature of ATSB in the second bottle is measured by a thermocouple inserted in a glass pocket extending into the centre of the bottle. In separate measurements it was ensured that the pocket thermocouple shows the actual temperature of the liquid.

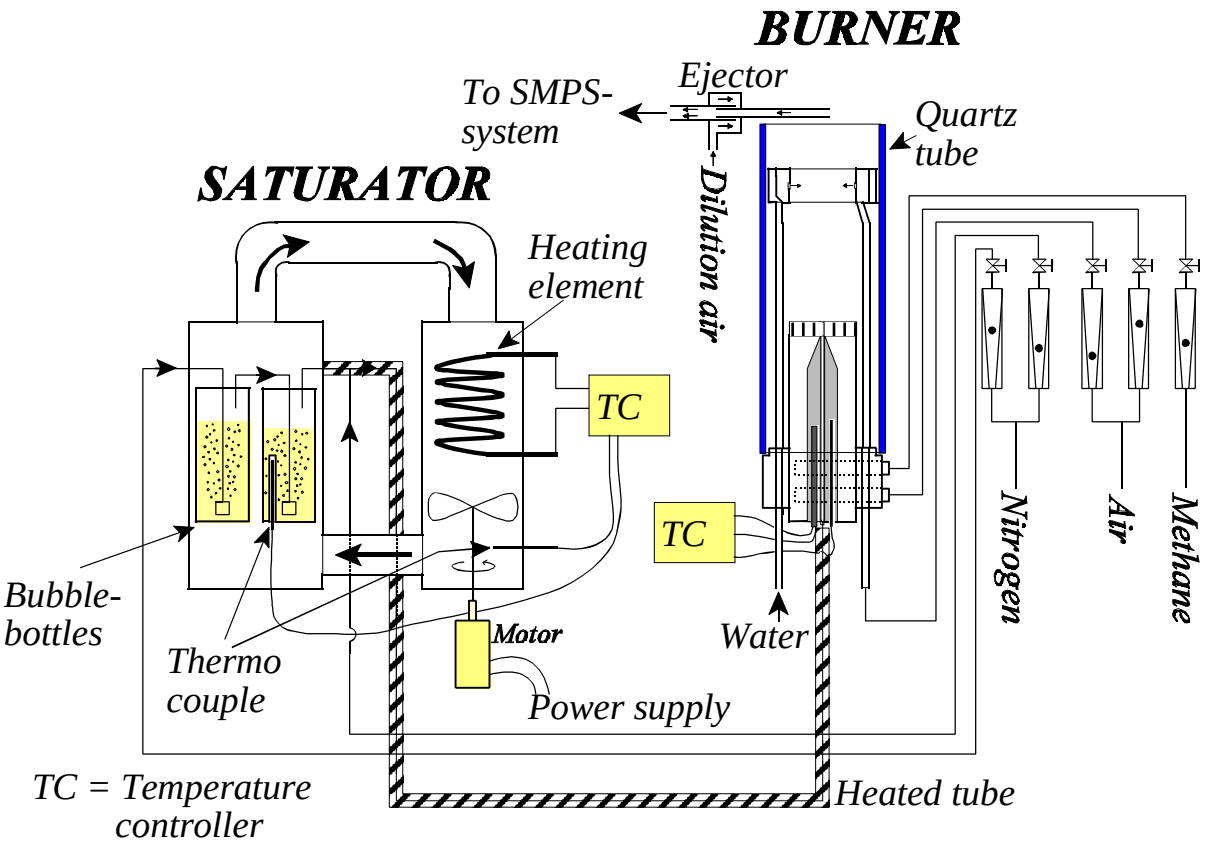

Figure 4 *A schematic of the initial premixed flame setup. The saturator unit is constructed to protect from effects of rapid thermal decomposition of the heated liquid precursor.*

The carrier gas, which is fed to the bubble bottles, is also nitrogen. To avoid any condensation of the precursor, the pipe from the outlet of the second bubble bottle to the bottom of the burner is heated by heating tape. Optional dilution of the saturated carrier gas from the second bubble bottle is mixed just outside the saturation unit. The diluter-gas is preheated nitrogen. Without preheating, supersaturation can occur by the mixing of the saturated precursor gas with cold dilution gas.

As mentioned in the description of the burner, the precursor pipe is also heated inside the burner by a brass heating jacket with a heating element inserted.

The flow of feed gasses to the burner and saturator is controlled by calibrated rotameters.

The flame process is kept inside a quartz tube (6 cm inner diameter) to avoid disturbances from the surrounding air. Furthermore, the schematic of the setup also shows a gas ejector at the burner process outlet. This device is used to sample the effluent aerosol for particle size

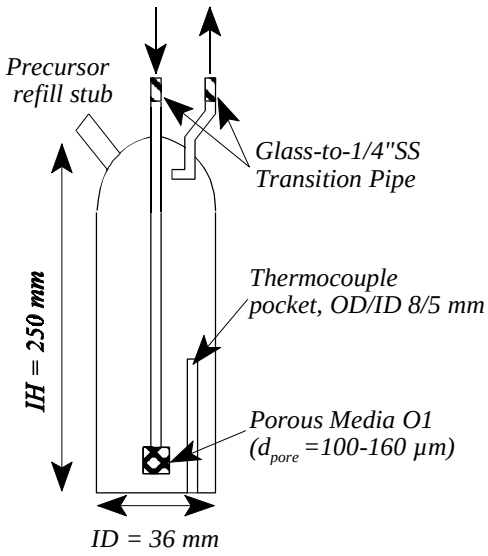

Figure 4 *The modified saturator unit.*

distribution measurements in an SMPS system. This will be further commented in a succeeding section on aerosol characterisation methods. After the initial tests of the whole setup, the safety hazards regarding ATSB were less critical than expected. Furthermore, the operation of the setup was complicated by difficulty of controlling the temperature of the bubble bottles because of very large time constants. Therefore, a more simple saturator unit was constructed. The modified saturator, shown on figure 4.7, is a single bubble bottle with a thermocouple pocket at the bottom.

The nitrogen inlet/outlet is 1/4''swagelock to glass transition pipe. In addition, there is a sealable stub for refill of ATSB. Figure 4.8 shows the setup, which uses the modified saturator. The electric power in the heating tape serves as an actuator for controlling the temperature of the precursor. The modified saturator operates flawlessly and the temperature stays within ±0.1°C of the set point.

The temperature of the heating tape enclosing the pipes from the saturator to the burner is kept above the dewpoint of the precursor and is controlled manually. Up to the burner exit, the temperature of the gases is kept suitably high, i.e. approximately 10-20°C above the dew-point.

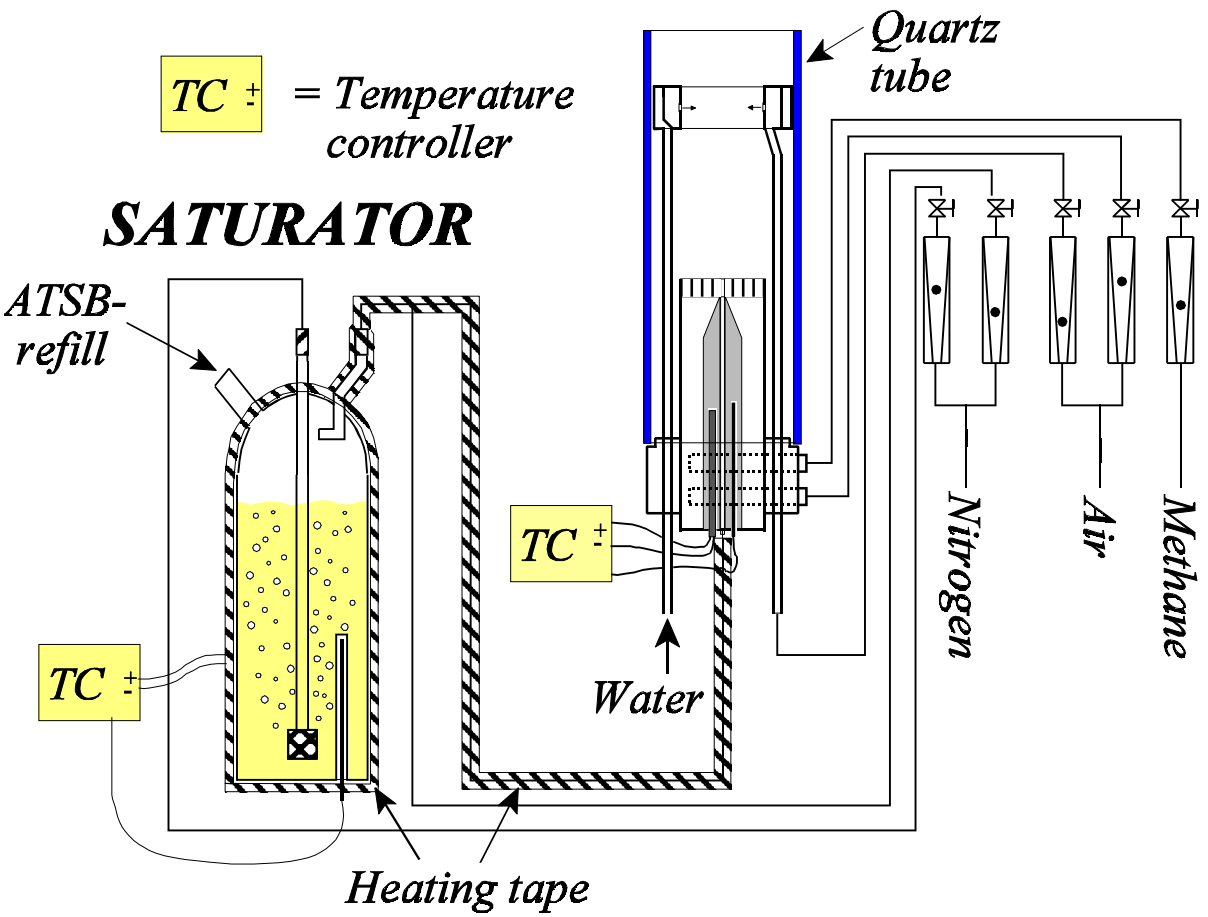

Figure 4 *The premixed burner experimental setup with the modified saturator*

4.2.2 Diffusion flame setup

Figure 4.9 shows a schematic of the experimental setup used for the experiments with the diffusion flame burner.

The apparatus consists of two parts, the saturator and the diffusion flame burner. The saturator is a 250 ml glass bottle with pure liquid ATSB heated with heating tape. Nitrogen bubbles through the hot ATSB through a distributor, which provides very small bubbles. They rise slowly through a liquid height of 10-12 cm, which ensures that the gas becomes saturated with ATSB. The liquid temperature is controlled by a thermocouple inserted in a glass pocket extending into the centre of the bottle and hinged to a temperature controller. In separate measurements it was ensured that the pocket thermocouple shows the temperature of the liquid. After saturation, the precursor-gas flows through a short tube to the burner. To avoid condensation of the precursor, the tube and the burner are heated by heating tape. To minimize unnecessary heat loss, insulating material is used to cover the heated parts of the setup. The

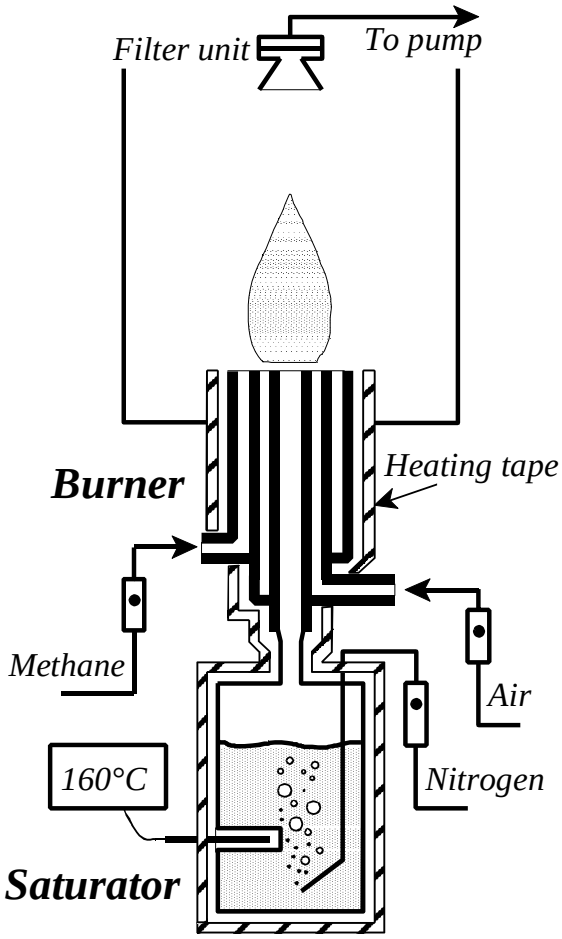

Figure 4 *A schematic of the diffusion flame burner setup.*

temperature of the gases up to the burner exit is kept suitably high, i.e. approximately 10-20°C above the dew-point as with the premixed burner setup. To prevent the surrounding air from disturbing the flame, the burner is placed in a compartment, which is only open at the top, and the whole system is placed in a fume hood. The flow of feed gases to the burner is controlled by calibrated rotameters.

For measuring the specific surface are of the powder, particles are collected on glass fibre filter mats (Gelman Scientific, 47 mm) placed in a filter holder fixed 20 cm above the burner. The product gas is sucked through the filter by a vacuum pump.

An SMPS system (scanning mobility particle sizer) measures the aggregate size distribution at the process outlet.

4.3 Aerosol characterisation methods

The following sections provide an overview of the methods used for measuring aerosol properties of relevance to this work.

4.3.1 The SMPS-system and the gas ejector

Size distributions of aggregates based on the mobility in air is measured by a scanning mobility particle sizer (SMPS). The SMPS system, figure 4.10, consists of a differential mobility analyser (DMA 3071A, TSI) and a condensational particle counter (CPC 3022, TSI). The DMA charges the polydisperse inlet aerosol sampled from the flame process. The charged particles pass through a variable electrostatic field, where aggregates with a preselected mobility will pass through a small slit at the bottom of the DMA. The monodisperse outlet from the DMA flows to the condensational particle counter (CPC) where the concentration of the monodisperse outlet is measured. By changing the voltage of the electrostatic field in the DMA, the particle concentration of many small mobility channels is measured and the whole distribution, within a certain size range, is determined. The SMPS system is connected to a PC, which controls the voltage in a continuous scanning mode thereby shortening the time for a single measurement from around 20 minutes for the non-scanning mode to around 2-4 minutes for the scanning mode. The polydisperse inlet to the SMPS system is continuously sampled from the flame process outlet by a gas ejector.

The gas ejector on figure 4.11 uses a high flow-rate of particle-free dilution gas to withdraw a small sample flow of the product gas through the sampling tube by the ejector action of the dilution gas. This sampling technique has the advantage of a low residence time (< 20 ms) of the hot and concentrated aerosol in the sample probe, and the subsequent immediate cooling and

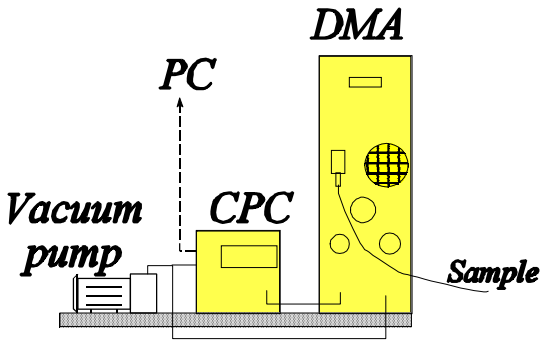

Figure 4 *The SMPS system for measuring particle/aggregate size distributions.*

dilution of the sample stream effectively quench further particle sintering and reduces the rate of coagulation of aggregates. The characteristic collision time is reduced from the order of seconds to the order of minutes.

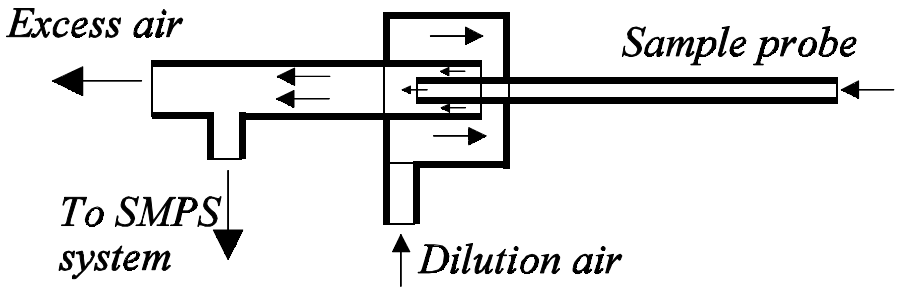

Figure 4 *A schematic of the gas ejector used to continuously sample and dilute from the flame process outlet. The sampling probe is a 1/8'' SS pipe, approximately 10 cm long*.

4.3.2 Characterisation of the gas ejector

The dilution ratio in the ejector is highly dependent on the inner diameter of the sampling tube and the velocity of the dilution gas in the annulus. The velocity of the dilution gas is a function of the volume flow rate and the width of the annulus at the outer side of the sampling tube.
The high velocity of the dilution gas creates a low-pressure zone at the end of the sampling tube inside the ejector. The pressure difference drives the flow of the sampling gas into the ejector. The volumetric flow through the tube is proportional to the pressure drop in the tube, which depends on viscosity, inner diameter and linear velocity.
The viscosity of a gas changes with temperature approximately with the square root of the temperature. Therefore, we cannot expect the dilution ratio to be independent of the temperature of the gas at the sampling point. This is important when the hot gas from the flame process is sampled with the ejector.

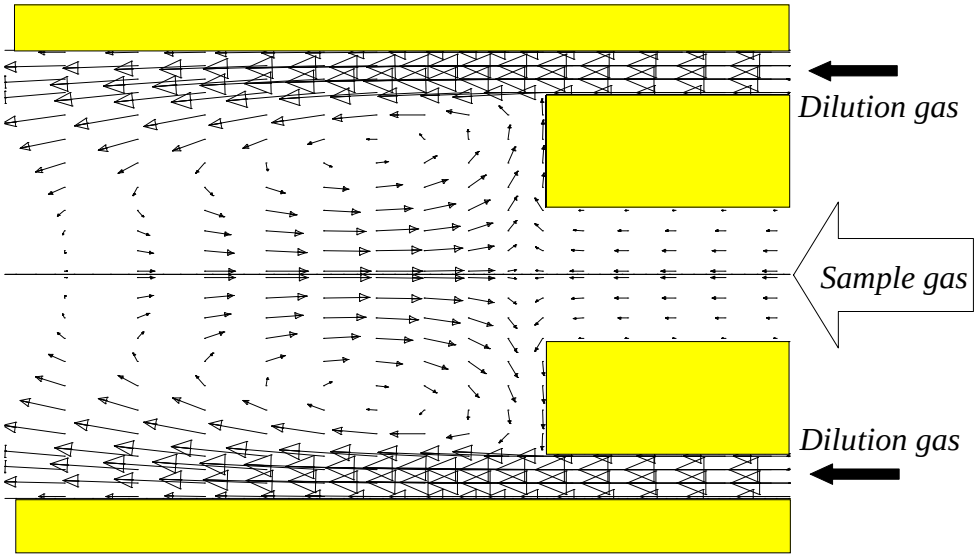

Figure 4 *CFD-simulation of the gas ejector: A blow-up of the velocity vectors at the mixing point. The high velocity dilution gas creates a low pressure zone at the sampling tube end, thereby "sucking" gas through the sampling tube. Vectors are only shown for every third computational cell in each direction*

The performance of the ejector has been investigated by simulating the gas flow by computational fluid dynamics. This numerical method, which solves the fundamental equation for flow in a computational grid similar to the physical system, will be described later, and we will only discuss the simulation results in this section.

Figure 4.12 shows the gas velocity vectors inside the ejector at the end of the sampling tube. The dilution gas, which creates the flow in the sampling tube, has a mean velocity of 40 m/s. Inside the ejector, the geometry causes the flow to form large eddies. In this simulation, the temperature of both dilution and sampling gas is 298K.

Additional simulations were carried out in which the temperature of the sampling gas was increased to 600K and 900K with the dilution gas fixed at 298K. The temperature of the sample gas is assumed to remain constant up to the tube exit at the mixing point, i.e. the temperature of the inner wall is assumed to be equal to that of the gas.

Figure 4.13 shows the dilution ratio from the CFD-simulations as a function of the sample temperature. The dimensions of the sample tube: ID: 1.5mm,OD: 3mm, length: 10 cm. The width of the annulus is 0.4mm.

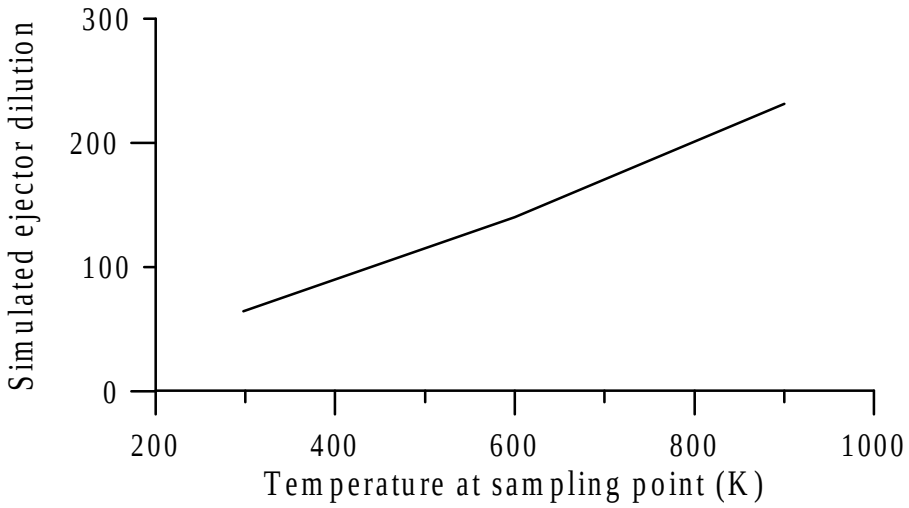

Figure 4 *Simulated ejector dilution factor as a function of gas temperature at sampling point. The temperature of inner wall of the sampling tube is assumed to be equal to the sample-gas temperature*

In the temperature range of 298K to 900K the dilution ratio varies approximately linearly from 65 (289K) to 231 (900K). These calculations are, despite the accuracy of the CFD-method, still approximative, since the wall boundary temperature in the tube is assumed constant.

An additional simulation at 298K with the same geometry but with half the inner diameter of the sample tube resulted in an increase in the dilution ratio from 64 to 680. The pressure drop in a tube is very dependent on the tube radius, as is seen here.

The main conclusions based on the analysis of the ejector are:

- Large variations in the dilution ratio can be obtained by changing the tube radius, the dilution flow annulus and the flow rate of dilution air.
- The temperature of the gas at the sampling point (and through the tube) affects the dilution ratio. Any calibration of the dilution at room temperature is not applicable at higher temperatures.

4.3.3 Specific surface area measurements

The specific surface area of the powder collected on filters is measured by multi-point nitrogen adsorption (Gemini 2360, Micromeritics) at 77 K in combination with the BET-equation. By assuming spherical particles, one can calculate a BET equivalent primary particle size, d_{BET}, from:

$$d_{BET} = \frac{6}{\rho_p S_A} \qquad \textbf{(4)}$$

where ρ_p is the solid volume density and S_A is the specific surface area. In the text, the specific surface area will often be abbreviated as *SSA* also.

The measurement of specific surface area is a robust integral method of particle characterisation. When experiments are planned, one must consider the mass of particles needed to ensure that the total surface area of the particles is well above the detection limit for the BET-apparatus.

4.3.4 TEM images

Transmission electron microscope (TEM) images are suited for investigating the microstructure of aggregates. Still, drawing conclusions based on TEM images must be done with great care. Aggregates on a TEM-image only represent a momentary picture of a minute fraction of aggregates. However, with homogeneity of the process taken into account, TEM images provide valuable information about particle morphology, which cannot be obtained otherwise.

The TEM-grids, which consist of a fine Cu-mesh covered with carbon film, are prepared exposing the cold, clean grids to the hot product gas for 5-10 seconds. Thermophoresis is the dominant deposition mechanism. Pictures of sampled grids are prepared in a Phillips 300kV transmission electron microscope.

5 Experimental results

The presentation of the experimental results is divided into two sections: The diffusion flame experiments and premixed burner experiments.

5.1 Diffusion flame experiments

Before the actual experiments were carried out, stable operating conditions of the diffusion flame were determined. Several combinations of feed gases are possible.

Figure 5.1 shows four different burner modes, labelled A -D, following the notation of Pratsinis et al. (1996). Mode B with nitrogen and precursor in the central tube, air in the second tube and

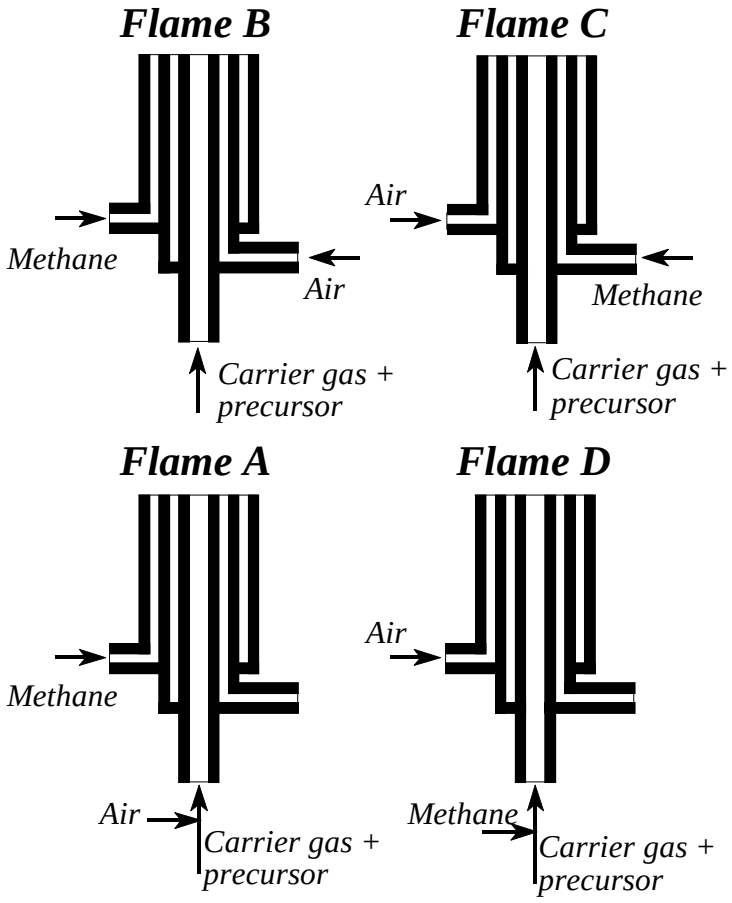

Figure 5 *A schematic of different flame configurations. Flames B and C are used for the production of alumina in the present study, while all flames are used by Pratsinis et al. (1996) for the production of titania.*

methane in the third (double diffusion flame) and mode C with methane in the second tube and air in the third (single diffusion flame) are used in this study for the production of alumina. All four flame modes are used in the TiO_2-study by Pratsinis et al. (1996).

Since ATSB is unstable in the presence of oxygen or water, using mode A in this study is not possible. Decomposition of ATSB when air and precursor gas is mixed below the burner would disturb the measurements, making it impossible to determine the initial point of particle dynamics. Coagulation of Al_2O_3 monomers in the jet tube below the flame would occur.

Flame D is not as critical as flame A in terms of precursor decomposition, since ATSB should be stable in methane atmosphere. However, the purity of methane could affect the quality of the measurements. Therefore, only flames B and C are used in the alumina experiments.

Twelve measurements of Al_2O_3 synthesis were made with burner modes B and C. The experimental design, shown in table 5.1, comprises a constant air feed rate, three levels of methane feed rate, and two levels of nitrogen, in pairs identical for the two burner modes. The feed rates were chosen so that stable flames, based on visual observation, are obtained. For the two highest methane flows, the flame is sub-stoichiometric with respect to oxygen from the air feed. Additional oxygen is provided from the surrounding still air. The flames are all blue in colour, indicating total fuel combustion.

Table 5.1 *Operating conditions for the Al_2O_3 experiments. The series 1-3 and 4-6 differ with respect to N_2-flow, while methane flow is varied within each series. For all conditions the air flow rate is 1.8 l/min and the saturator temperature is 160 °C. At that saturation temperature, the mole-fraction of ATSB in the N_2 carrier gas is 0.0046.*

Flame	B1	B2	B3	B4	B5	B6
N_2 (l/min)	0.38	0.38	0.38	0.26	0.26	0.26
CH_4 (l/min)	0.38	0.27	0.145	0.38	0.27	0.145
Flame	C1	C2	C3	C4	C5	C6
N_2 (l/min)	0.38	0.38	0.38	0.26	0.26	0.26
CH_4 (l/min)	0.38	0.27	0.145	0.38	0.27	0.145

For flame C, a single flame front between the methane and the supplied air exists. Flame B has two flame fronts, an internal one between the supplied air and the methane and an external one between the methane and the surrounding air. The difference between B and C is clearly visible. The procedure for depositing particles on filters is as follows:

- Initially the temperature controllers of the units are switched on. Because of the large time constant, it takes approximately one hour for the saturator to reach the steady state. Meanwhile, the temperatures of the burner and the tube from the saturator to the burner reach the desired level, slightly above the saturation temperature.
- All flows are set to the desired values and the flame is ignited.
- After 1 min., particle collection by filtration starts. Particles are collected for approximately 30 minutes.

Particle mass from each experiment is obtained by carefully scraping powder of each filter. Samples for the BET instrument are prepared in glass tubes with a weighed mass of particles. The specific surface area is then determined by the measured surface area divided by the mass of particles.

TEM-grids are prepared by exposing cold, clean grids to the hot product gas for 5-10 seconds, using thermophoresis as the dominant deposition mechanism.

The aggregate size distribution is measured "on-line" downstream from the ejector sampler, from where a side stream is fed to the SMPS system. Several distributions were measured for each configuration.

The dilution ratio in the ejector operating at room temperature was approximately 1:16. This was calculated by measuring the total particle concentration in the surrounding air with and without ejector dilution. Since the dilution gas is particle-free (less than 10 cm^{-3}), the dilution ratio is simply the ratio of the measured concentrations with and without the ejector. The total number concentration was measured directly in the CPC (condensational particle counter). However, the dilution ratio will increase when the ejector samples at higher temperatures. Therefore, we cannot expect the dilution ratio to be constant for all experiments. The flow rate of methane will influence the outlet temperature and therefore also the ejector dilution.

The ejector sampling system is useful for measuring the average aggregate size and the normalized size distribution in the flame by the SMPS even if the dilution ratio is not known precisely. For example, if the dilution in the ejector varies between 1:30 and 1:40, the dilution ratio in both cases is sufficient for freezing the aggregate sizes due to the rapid reduction in total concentration after the ejector. The subsequent coagulation during the short residence time in the

transport tube to the SMPS system does not change the shape of the size distribution. Therefore, if the same distribution is measured with two slightly different dilutions ratios in the ejector, the difference is only a concentration factor multiplied on each size section. The average size and the normalized distributions are the same.

If the absolute size distribution is to be measured, the dilution ratio has to be determined accurately, either by measurements or detailed calculations.

5.1.1 Flame photographs

Figure 5.2 shows photographs of flames B1, B3, C1 and C3. The flame configurations are listed in table 5.1. Number "1" corresponds to high methane flow rate while "3"is the low methane flow rate. The difference between single (C) and double diffusion (B) flames is easiest seen for the cases with low methane flow rate. The reaction zone for flame B3 forms a ring around the nitrogen jet. Viewed from the top, a "hole" extends through the reaction zone. This is not so for flame C3.

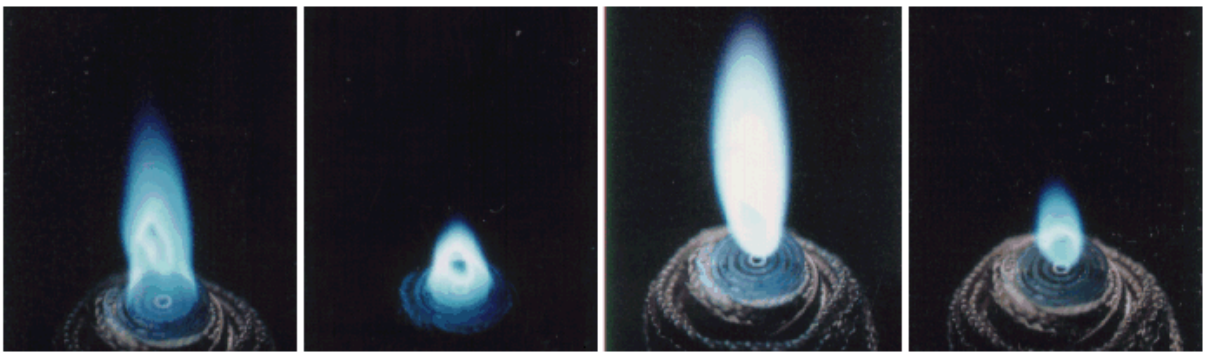

Figure 5 *Photographs of flames at different operating conditions. The B-flames are double diffusion flames and C- flames are single diffusion. The difference is clearly visible. Operating conditions are listed in table 5.1.*

5.1.2 Temperature profiles

For selected operating conditions, temperature profiles along the vertical axis of the central jet and the radial peak temperatures as a function of height were measured with a 0.008" Pt/10%Rh-Rh, Type S, thermocouple (Omega Engineering) insulated with an alumina sheath tube (ID 1/32", OD 1/8"). The last centimetre of the two thermocouple wires up to the welded connection point was not insulated. The measured temperatures were corrected for radiation loss according to Collis and Williams, 1959. All profiles were measured without the precursor. Measurements with particles present in the gas would result in deposition of particles on the wire by thermophoresis and diffusion, causing a change the emissivity of the wire. The oxidation of the precursor will provide a minor heat contribution to the flame, which will be discussed later. For flame configurations B4 and C4, two sets of temperature measurements were carried out. First, the temperature profile along the central jet axis as a function of height above the burner was measured.

The measurements are shown on figure 5.3.

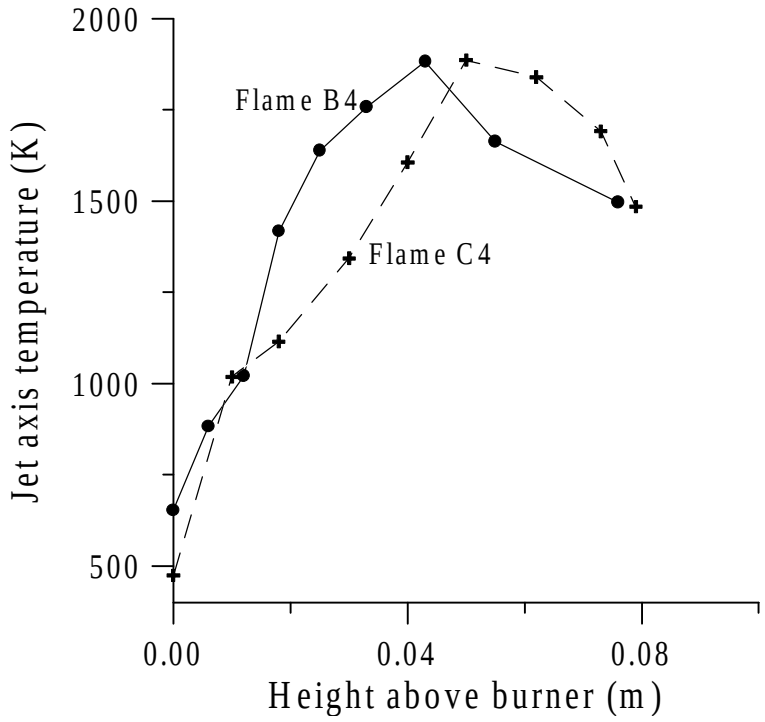

Figure 5 *Temperature profiles measured at the symmetry axis of the jet for two different operating conditions: Flame B4 and C4*

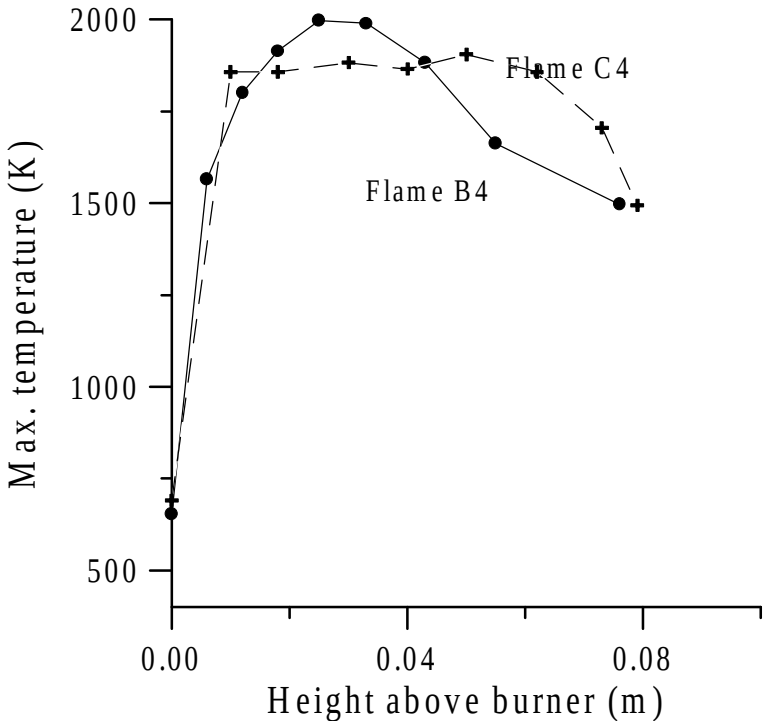

Figure 5 *The maximum temperature is shown as a function of height above the burner. Below the tip of the flame, the maximum temperature is located away from the jet axis.*

The value of the peak temperature is almost the same for the two selected cases, but the position of the peak is slightly closer to the burner mouth for flame B4.

Another type of profile measurement was also carried out. Below the flame tip, the maximum temperature of a given vertical position was found. It is normally located away from the vertical symmetry axis.

Figure 5.4 shows the maximum temperature as a function of height. For flame C4 there is a large plateau at high temperature. The temperature plateau at the high temperature level corresponds to the temperature of the reaction zone along the single flame front. Flame B4 appears more intense because of the double diffusion flame structure, which provides a more effective mixing of the air and methane and this flame shows a one-peak temperature curve at a slightly higher temperature level.

5.1.3 Specific surface area measurements

A graph of the specific surface area of the alumina particles from each of the twelve experimental conditions of table 5.1 is shown on figure 5.5.

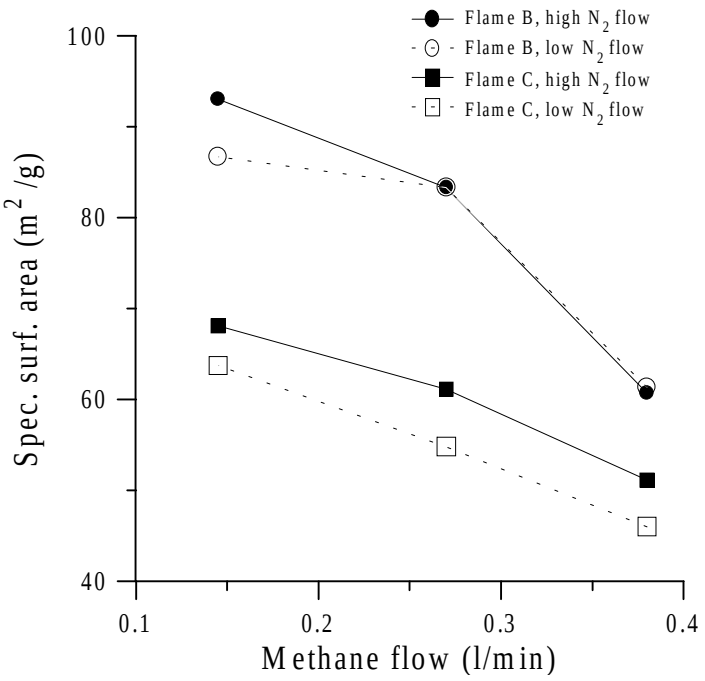

Figure 5 *The points on the graph represents experimental values of the specific surface area of the Al_2O_3 powder manufactured at the set of operating conditions shown in table 5.1.*

The specific surface area varies from approximately 45 m^2/g to 95 m^2/g. In terms of BET-equivalent primary particle diameter, calculated from equation 4.1 , the corresponding range is 16 nm to 34 nm, based on an alumina density of 3.97 g/cm^3 (Handbook of Chemistry and Physics, 1977). The BET-measurements of powders made on separate days but at the same operating conditions were reproducible with a deviation on the specific surface area of 2-5%. Variations in the methane flow rate and the flame configuration (B vs. C) have the largest effect on the specific surface area. In the investigated range, the effect of the nitrogen flow rate is only significant for flame C. As expected, the specific surface area decreases with increasing methane flow. The higher the temperature, the lower the specific surface area. For given flow rates, configuration C yields lower specific surface area than configuration B.

5.1.4 TEM images

Though the results from TEM images represent only a minute fraction of the particles, the information gathered from these high magnifications is important for this work, due to the precise revelation of the morphology of the dendritic aggregates.

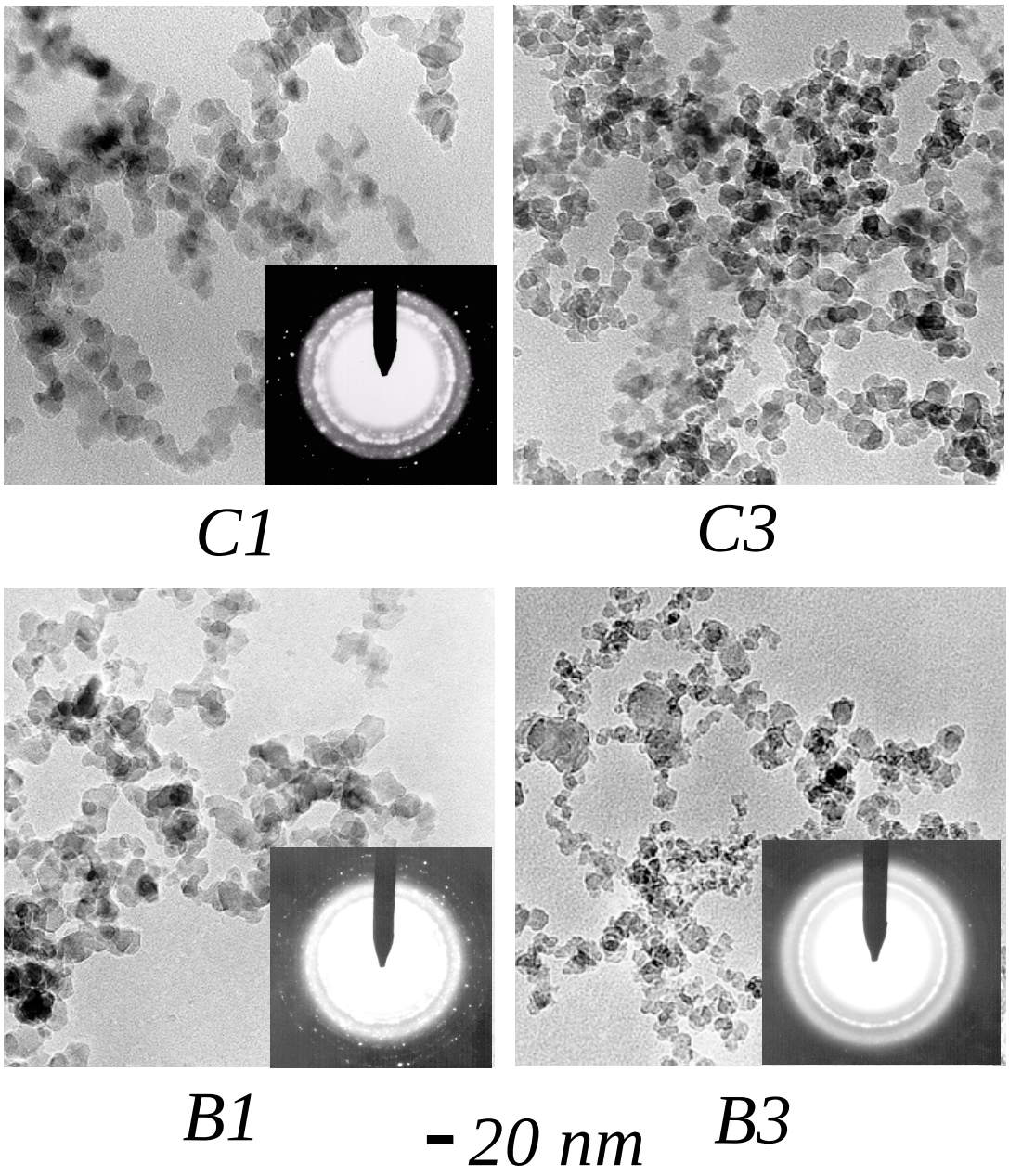

Figure 5 *TEM images of alumina particles from different flame operating conditions. Large aggregates of primary particles are seen for all conditions. The size distribution of the primary particles seems quite narrow for flames C1 and C3, whereas flames B1 and especially B3 have a wide range of primary particle sizes. For three of the four images, the diffraction images have been inserted. The spots and formation of rings show that at least some of the particles are crystalline*

This section will show TEM images from several flame configurations and relevant information will be discussed. Figure 5.6 consists of TEM images of four different operating conditions. As the results of the specific surface area showed, the methane flow and flame configuration had the largest effect. TEM-grids with particles from all twelve operating conditions have been prepared. However, only results from the high nitrogen flow rate cases (numbers 1-3) are shown here, since the images from the low nitrogen flow rate cases (numbers 4-6) are similar to those presented here, only shifted slightly towards smaller particles.

The TEM-images reveal some interesting features of the flames. As expected from the specific surface area measurements, the TEM's from flames B1 and C1 show larger particles compared with B3 and C3 respectively. However, there is another important difference between B and C. The primary particles from the C-flames are, at least on the images, quite homogeneous in size for both C1 and C3. This is not so for the B-flames. The primary particle size varies much more and especially flame B3 has a large variation of primary particle sizes.

This can be explained based on the photograph of the flames in figure 5.2. Flame B3 is very heterogeneous in structure. Since the reaction zone almost forms a ring around the precursor containing nitrogen jet, a fraction of the jet close to the jet axis will pass through lower temperatures compared with the outer part of the jet, which is closer to the flame.

This is not the case for any of the C-flames, since the single diffusion flame always forms a flame-tip at the jet axis.

The particles from flame B1 are more homogeneous in size, since the high methane flow rate provides a flame more like the C-type.

For flames C1, B1 and B3, the diffraction patterns are inserted on figure 5.6. All three flames show spots and ring formation indication crystalline material. The identification of the alumina phase(s) has not been determined. Flames B1 and C1 have more clear spots, since those particles are formed in the flames with the highest methane flow.

The primary particle size can be estimated from the TEM images by direct measurements on the images. The measurements were carried out on images with a magnification of 265000 (*88600 in the microscope and *3 in the developing procedure). On the images, the particles are from 4 to 7 mm in size. This procedure was only applicable for the C-flames, where the particles are quite homogeneous in size. For flame B, the range of particle sizes on the TEM image [cf. figure

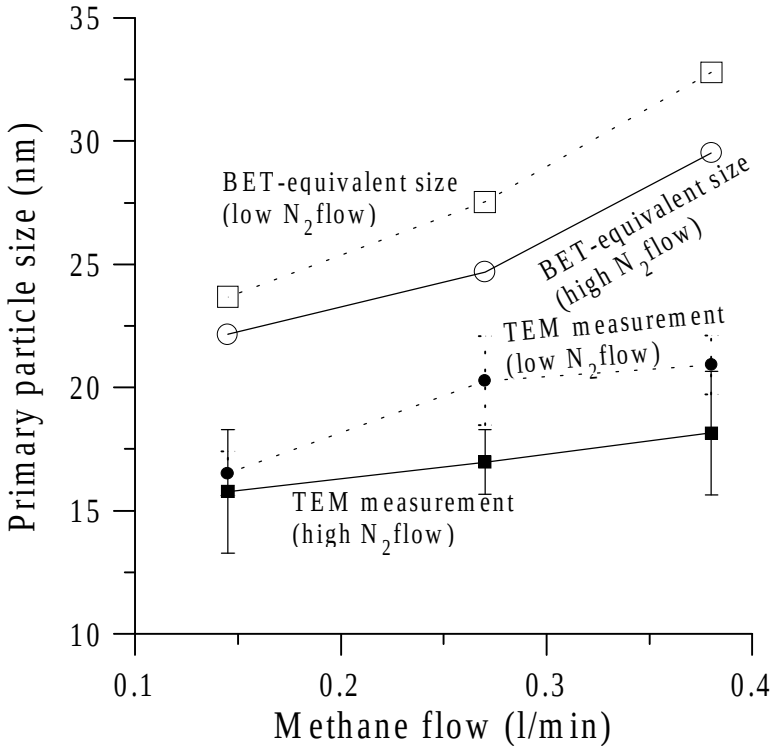

Figure 5 *The points represent experimental values of the primary particle size of the Al_2O_3 particles from the C-flames (operating conditions from table 5.1) obtained from TEM images and computed from SSA measurements.*

5.6] was too large.

From the specific surface area measurements, the equivalent primary particle size was calculated and those values are compared with the results of the sizes measured on the TEM images.

For all C-flames, the particle size computed from the BET-data exceeds the values obtained from the TEM images [cf. figure 5.7]. This is mainly caused by the loss of surface area between partly

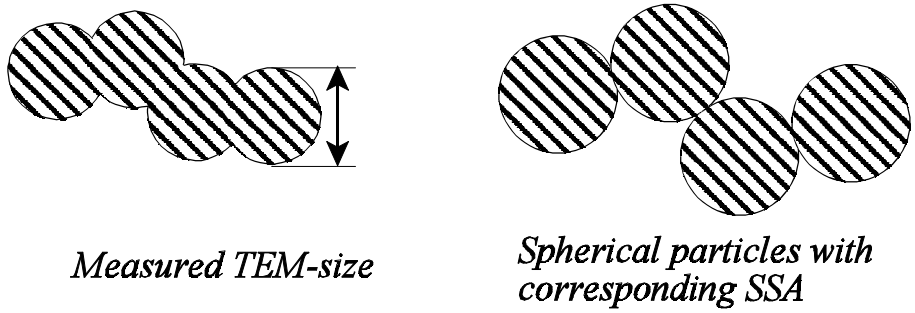

Figure 5 *A schematic of the difference between the particle size in aggregates obtained from TEM images and the calculated value based on the BET-surface area of the aggregates. The difference is caused by the loss of surface area in the real aggregate when neighbouring particles form necks*

coalesced particles. The initial neck formation between particles causes a loss of surface area but the size measured on TEM images is not affected by this since the size is measured across the identifiable particles. Therefore, when the surface area is converted to an equivalent particle size, the assumption of spherical, point-connected particles results in an equivalent size that is larger than the necked primary particles. This point is illustrated on figure 5.8. Non-coalesced primary particles must be larger than the individual partly coalesced particles to have the same surface area per mass.

5.1.5 Particle size distributions

The gas ejector in combination with the SMPS (scanning mobility particle sizer) system is well suited for analysing size distributions of the agglomerates.
In the present work, size distributions were only measured at the process outlet. In continuation of the present work, it is planned to investigate the development of the size distribution as a function of height above the burner and of the radial position. However, sampling closer to the

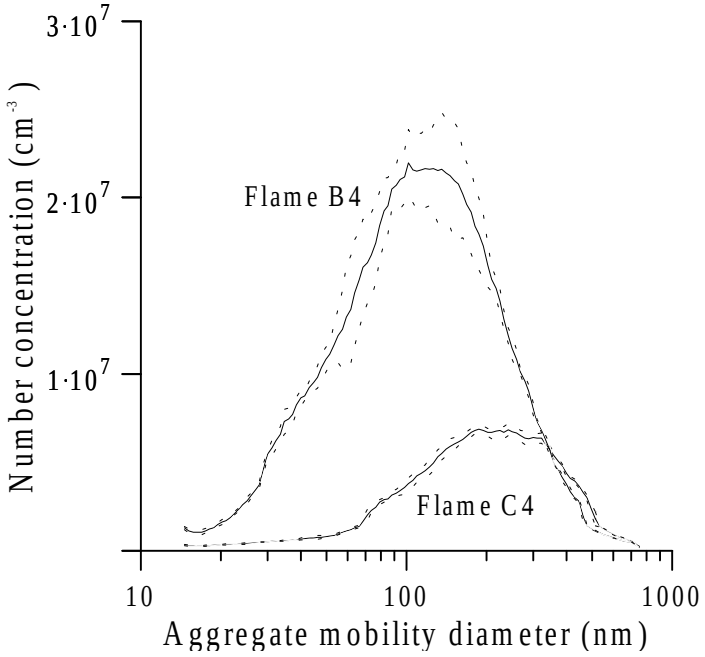

Figure 5 *Size distributions for two different operating conditions (flames C4 and B4, table 5.1) measured by SMPS-system at the burner outlet after dilution and cooling in the gas ejector. Each distribution is an average of several runs, for which the standard deviation is also shown*

flame will require closer control of the coagulation in the sampling tube because of the higher concentration levels deeper in the flame process.

Aggregate mobility diameter distributions were measured by the SMPS system after dilution of the sampled product gas in the ejector. In average, three distributions were measured for each flame and the distributions are shown with the standard error on the measurement.

Figure 5.9 shows the measured size distributions with standard deviation for flames B4 and C4. The operating conditions are listed in table 5.1. The two distributions differ significantly. Flame B4 yields a larger total concentration of aggregates but a smaller mean aggregate size. Based on the measured distributions, the average aggregate mobility diameters and the average total concentrations are calculated for the different flames and the results are summarized in the graphs below. The mean aggregate diameter as a function of methane flow for fixed flame types and nitrogen flow rates is shown on figure 5.10. Figure 5.11 shows the corresponding graph for the total aggregate concentration.

An overall trend is, that flame B yields smaller aggregates at higher concentrations compared with flame C for identical flow of feed gases. Furthermore, for each curve, an increase in methane flow results in a decrease in aggregate size and a decrease in concentration.

The total concentration results [cf. figure 5.11] are less useful because the dilution ratio in the ejector probably changes between experiments with different methane flow rates. The experimental points on figure 5.11, however, can still be compared vertically at a constant methane flow rate. At a constant methane flow rate, the outlet temperature is approximately constant despite nitrogen flow rate and flame configuration

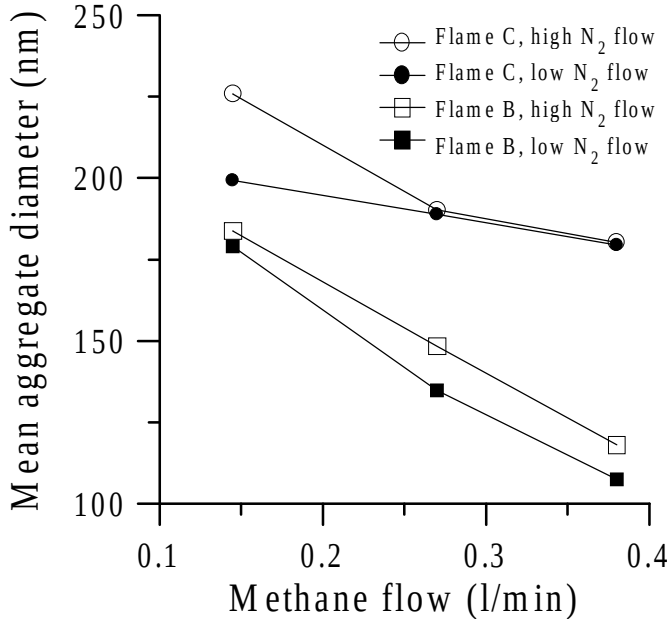

Figure 5 *Mean aggregate mobility diameter as a function of methane flow rate for the different nitrogen flow rates and flame types. Data points are calculated from SMPS size distributions measured after dilution in the ejector. Operating conditions are listed in table 5.1*

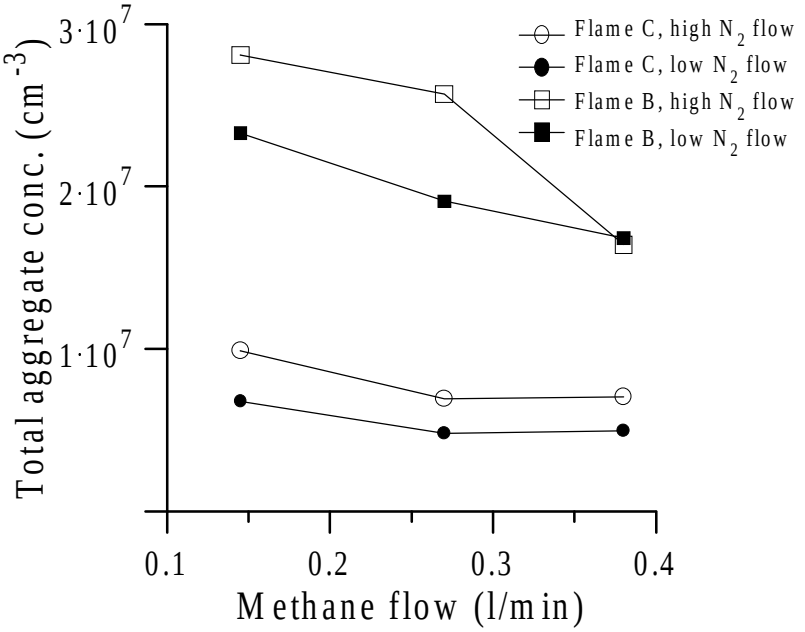

Figure 5 *Total aggregate concentration as a function of methane flow for the different nitrogen flow rates and flame types. Data points are calculated from SMPS size distributions measured after dilution in the ejector. Operating conditions are listed in table 5.1*

5.2 Premixed burner experiments

Initially, several experiments with the premixed burner were carried out to explore the ranges of operation of the flame. During the last part of the project, a final experimental scheme was determined. The purpose of this experimental design was to get a clear overview, with as few experiments as possible, of the possibilities of using a precursor jet in a premixed burner with rapid quenching. For these four experiments, a thorough analysis including specific surface area measurements, TEM-analyses, aggregate size distributions and detailed burner simulations by computational fluid dynamics, is carried out.

The important operating parameters are summarized in figure 5.12.

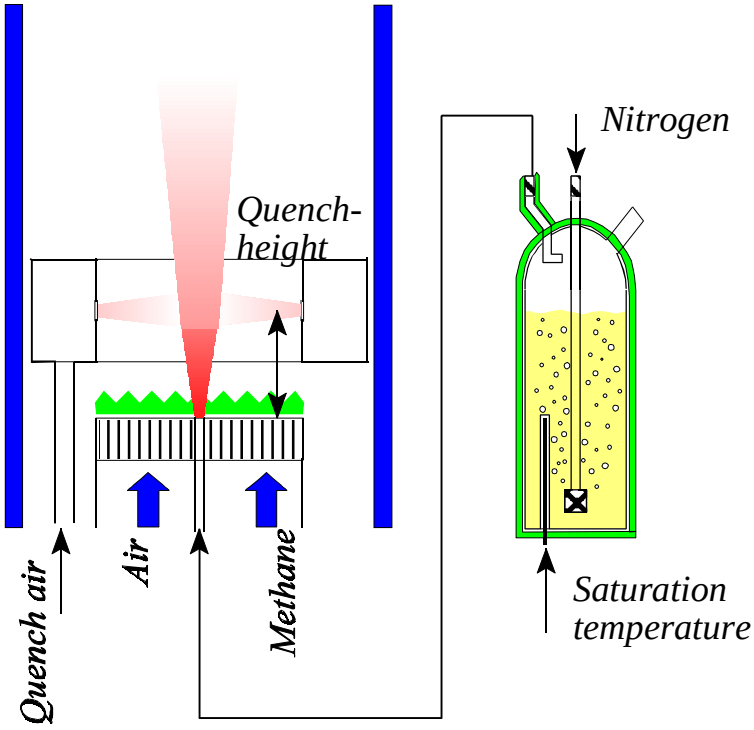

Figure 5 *A schematic of the premixed burner with indication of the main operating parameters*

Table 5.2 *Operating conditions for the premixed burner experiments. For all experiments the quench-height is 3 cm, air flow rate is 10.5 l/min, methane flow rate is 0.83 l/min and the saturator temperature is 160 °C.*

Experiment	Nitrogen (l/min)	Quench air (l/min)	$v_{jet,average}$ (m/s)	v_{quench} (m/s)
P1	1.0	0	14	0
P2	1.0	4.1	14	17.5
P3	0.16	0	2.2	0
P4	0.16	2.6	2.2	11

The experimental design (table 5.2) consists of four sets of operating conditions.
The nitrogen flow rate has two different values in order to study the effect of residence time in the system. For each value of the nitrogen flow rate, runs are made with and without quenching. The volumetric flow rate of the quench-air was lower for P4 than P2. This is necessary to avoid severe disturbance of the flow patterns just above the flame arrestor. For both the jet and the quenching air, the average linear exit velocity is computed.
The quenching height was fixed at 3 centimetres above the flame arrestor. With this positioning of the quenching ring just above the flame, the effect of quenching on the particle morphology is supposedly very significant.
For all experiments, the saturator temperature is 160 °C. At this precursor concentration level, the production rate is sufficient for collecting enough particle mass on filters for specific surface area measurements. By using a saturator temperature of 160°C, the premixed flame experiments become comparable to the diffusion flame experiments.
Furthermore, the methane and air flow rate are set at 10.5 l/min and 0.82 l/min respectively. At those flow rates, the premixed flame is very stable.

The measuring procedure for depositing particles on filters is essentially the same as for the diffusion flame experiments:

- Initially the temperature controllers of the units are switched on. Because of the large time constant, it takes approximately one hour for the saturator to reach the steady state. Meanwhile, the temperature of the brass heating jacket and the tube from the saturator to the burner reaches the desired level, slightly above the saturation temperature.

- All flows rates are then set to the desired values and the flame is ignited.
- After 1 min., particle collection by filtration starts. Particles are collected on the filter (Whatman, 47 mmØ glass micro fibre filters) for 15-25 minutes.

The procedure for measuring the specific surface area is different from the diffusion flame experiments. In the diffusion flame experiments, particles were scraped off the filter, weighed and the specific surface area was determined. The problem with this method is the possibility of scraping parts of the filter material off when the particles are recovered from the filter, because the layer of particles is thin. This fraction of fibrous material can disturb the measurements.
A new method, which avoids this problem, is used for the premixed burner experiments.
Initially, one clean filter was weighed and the BET surface area was measured. Since the filters are very homogeneous, the specific surface area of each filter is with good approximation constant. During deposition experiments, any filter is weighed before and after deposition of alumina particles. The total specific surface area for the filter and particles is measured by putting the filter mat with particles in the test-tube.
After the total surface area measurement, the BET surface area of the particles is calculated by:

$$SSA_{particles} = \frac{SSA_{total} m_{total} - SSA_{filter} m_{filter}}{m_{total} - m_{filter}} \quad \textbf{(5)}$$

and SSA_i is specific surface area, m_i is the mass, where *"i"* is either particle, filter or total mass (particles + filter). For each experiment, SSA_{total}, m_{total}, *and* m_{filter} are measured while SSA_{filter} is assumed constant.
TEM-grids were prepared by exposing cold, clean grids to the hot product gas for 5-10 seconds, using thermophoresis as the dominant deposition mechanism.
The aggregate size distribution is measured "on-line" downstream from the ejector sampler, from where a side stream is fed to the SMPS system. Several distributions were measured for each configuration. The ejector was positioned at the top of the quartz tube and with the tip of the sampling tube positioned at the quartz tube centre.
The dilution ratio in the ejector operating at room temperature was approximately 1:32. This is calculated by measuring the total particle concentration of the surrounding air with and without ejector dilution. Since the dilution gas is particle-free (less than $10cm^{-3}$), the dilution ratio is simply the ratio of the measured concentrations with and without the ejector.
A different sampling tube was used at the premixed burner experiments. The inner diameter was

1.0 mm as opposed to 1.6 mm for the diffusion flame experiments, which results in higher dilution ratios.

5.2.1 Temperature measurements

For the premixed burner, temperature profiles along the jet axis are shown on figure 5.13 for the four experimental conditions in table 5.2. The two main operating parameters, jet exit velocity and quenching flow rate, have a significant influence on the temperature profiles. For the two cases without quenching, the increase in jet velocity results in a lower peak temperature whereas the position of the peak is shifted approximately 3 cm upwards, from 3.5 cm (P3) to 6.7 cm (P1). This is directly correlated with the higher volumetric flow rate (linear velocity) of nitrogen in

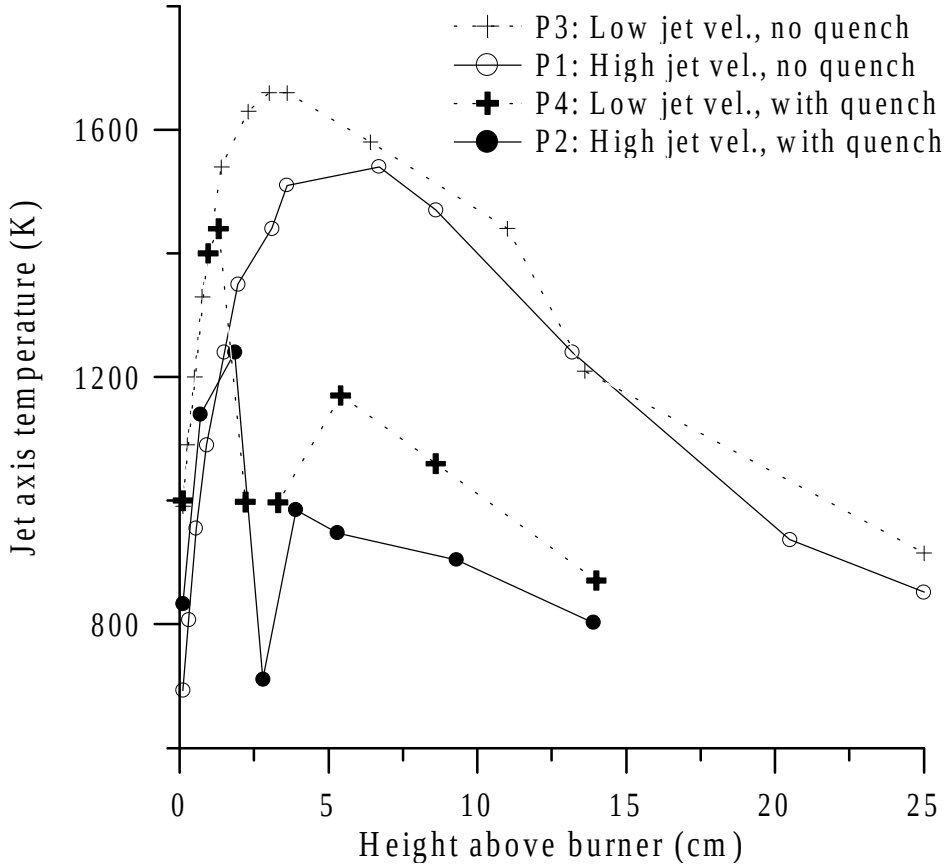

Figure 5 *Temperature profiles along the jet axis for the four different premixes burner experiments. Increasing the jet velocity results in a lower peak temperature and peak is located higher above the burner. The quench has a drastic effect on the vertical axis profile. There is a sharp drop in temperature at approximately 3 centimetres (the quenching height). The increase in temperature above the quenching point is caused by mixing with hotter gas surrounding the jet.*

the jet.

For the two cases with quenching, we see a very drastic effect on the profiles. At roughly 3 centimetres above the flame, which is the quenching height, the temperature of both P2 and P4 drops approximately 700K below those with no quenching. Still, the profiles up to the point of quenching lie close to the no-quench curves. Therefore, we can see that "shaping" the jet residence-time temperature relationship is possible within wide ranges by changing jet flow rate, quenching flow and height of quenching.

This is a very important result, since it confirms that the burner/quench system operates exactly as predicted in the design phase.

The outlet temperature is important for the estimation of the ejector dilution. For the four experimental conditions, the outlet temperatures are summarized in Table 5.3.

Table 5.3 *Results of temperature measurements at the process outlet. The operating conditions are listed in table* 5.2

Experiment	P1	P2	P3	P4
Outlet temperature	580 °C	340 °C	600 °C	320 °C

Though the linear jet velocity changes from 2.2 m/s (P1 and P2) to 14 m/s (P3 and P4), the volumetric flow rate of the jet is still low compared with the flow rate of methane and air and the effect on the outlet temperature is hardly significant. However, the quenching air reduces the temperature significantly because of the large volumetric flow. These measurements and the profiles above ensure that the cooling water in the quenching ring [cf. figure 4.4] serves its purpose. Without cooling water present, the quenching-ring metal would be heated by the combustion gases causing the quenching air to be heated on the way through the quenching ring. If that was the case, the difference in temperature between P1 and P2 and between P3 and P4 would be less significant.

Based on the large temperature difference (almost 300K) between the individual experiments, we must expect the dilution ratio in the ejector to vary with flame operating conditions. The dilution ration will be larger for P1 and P3 than for P2 and P4. The exact numeric difference is difficult to calculate. Based on the approximative computational fluid dynamics simulation [cf.

section 4.3.2], the dilution ratio is estimated to be approximately 1.5 times higher for the high outlet temperature experiments (P1, P3) than for the low outlet temperature experiments (P2, P4).

5.2.2 Specific surface area

The results of the specific surface area measurements are summarized in table 5.4.

Table 5.4 *Results of the specific surface area (SSA) measurements for alumina particles in the premixed burner. The value of the SSA for the filter-material, SSA_{filter} = 4.6 m^2/g, is used in all experiments. The surface area (SA) of each filter, which should be compared with $SA_{particles}$, is approximately 0.6 m^2.*

Experi-ment	m_{filter} (g)	m_{total} (g)	SSA_{total} (m^2/g)	$m_{particles}$ (g)	$SA_{particles}$ (m^2)	$SSA_{particles}$ (m^2/g)	$d_{p,\,BET}$ (nm)**
P1	0.1299	-	-	-	-	[153;187]*	[8.1;9.9]
P2	0.1316	0.1800	53.7	0.0484	9.1	187	8.1
P3	0.1301	0.1441	19.0	0.0140	2.14	153	9.9
P4	0.1312	0.1494	23.7	0.0182	2.94	161	9.4

* For experiment P1, $SSA_{particles}$ must be within the range of experiments P2 and P3 based on the range of experimental conditions from table 5.2

** Calculation of BET-equivalent primary particle size is based on equation 4.1

The results in table 5.4 show that the calculation of the specific surface area of the particles from the difference between filter and filter+particles is an expedient method. Especially for experiments with low mass deposition, where particles are difficult to recover from the filter. The total surface area of the particles, $SA_{particles}$, for the lowest case is more than four times the surface area of the filter material, SA_{filter}. If SSA_{filter} varies from filter to filter by, e.g. ±10%, then the resulting error on $SSA_{particles}$ is ±2% for the worst case.

The value of *SSA* for experiment P1 cannot be reported, because the sample tube with the filter from P1 broke in the BET-apparatus. However, it must be within the range of the *SSA* of experiments P2 and P3. The jet-velocity for P3 is lower then P1, which yields lower *SSA*. Furthermore, the *SSA* of P2 must be larger than or equal to P1, since for P2 the jet-velocity is the same as for P1 but P2 is with active quenching. This assessment ensures that the missing data point of P1 is inside the range of the other three data points but the exact value of the *SSA* for

P1 cannot be estimated.

For some of the cases, the variation of the *SSA* with the operating conditions agrees with the expectations. The lowest *SSA* is produced in P3 with the low jet velocity and no quench and the highest *SSA* in P2 with the high jet velocity and active quench.

By comparing P3 and P4, the quenching reduces the *SSA* of the particles. The effect of the quenching on the *SSA*, however, is small. The increase in *SSA* from 153 m^2/g (P3) to 161 m^2/g (P4) is quite insignificant.

Even with an increase in average jet velocity from 2.2 m/s to 14 m/s and activation of quenching, from P3 to P2, the increase in *SSA* is only from 153 to 187 m^2/g, only an increase by approximately 20%.

Since we have no reason to doubt the BET-results, we must conclude, that within the investigated range of operating conditions, the effect of quenching and jet velocity on the *SSA*, and hence on the primary particle size, is moderate.

If we compare the values of the *SSA* from the premixed flame system with the results from the diffusion flame (chapter 5.1.3), the diffusion flames yields lower *SSA* for all experimental conditions in this study. This is probably due to a lower residence time at the high temperature level for the premixed burner, where the precursor jet quickly passes through the short premixed flame zone. In the diffusion flame, the flame zone is positioned higher above the burner mouth than for the premixed burner.

5.2.3 TEM images

For each experiment, aggregates at the process outlet were deposited on TEM-grids by thermophoresis on cold, clean grids. The grid from experiment P1 was tightly covered with aggregates. This causes the image to be blurred due to the overcharging of the particles in the TEM vacuum chamber, and the image appears as if it is way of out focus. TEM results from experiment P1 therefore cannot be shown here.

By observing the aggregate images [cf. figure 5.14] for the three remaining experiments, we get the impression that the primary particle is smaller for P2 than P3 and P4.The difference between

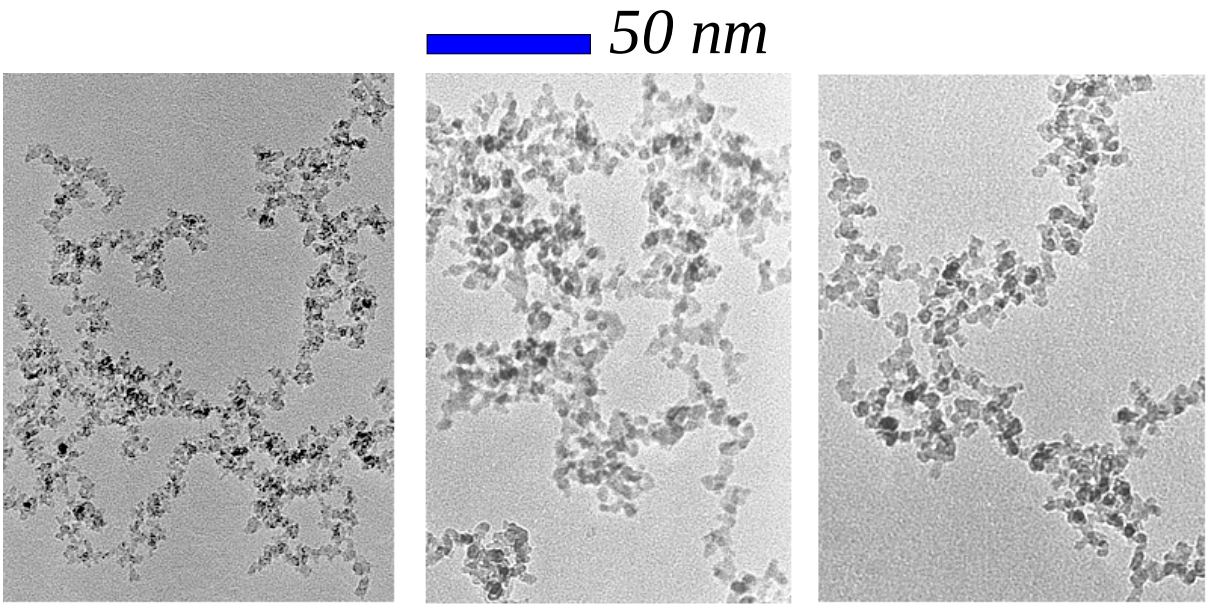

Figure 5 *Low magnification TEM images of alumina aggregates produces in experiments P2, P3 and P4. Compared with P3 and P4, the primary particles in the P2-aggregate appears more irregular. Operating conditions are listed in table 5.2.*

P3 and P4 is slight. The aggregates consist of numerous primary particles in a dendritic structure. Images with higher resolution are shown in figure 5.15 and the pattern of primary particle sizes is confirmed by these images. For P3 and P4, diffraction images are also shown. For P3, the vague ring pattern shows the presence of a crystalline phase. For P4 with low jet velocity as in case P3 but with quenching active, the ring has disappeared. Therefore, by activating the quench (from P3 to P4) the crystallinity seems to disappear completely. If we compare these images with the diffraction patterns from the diffusion flames [cf. figure 5.6], there is clearly a higher crystal order for the alumina produced in the diffusion flames, since the spots are more bright and multiple rings are present.

The primary particle size (PPS) can be estimated from the TEM images by measuring the size of particles on the images. The measurements are carried out on images with a magnification of 600.000 (*200.000 in the microscope and *3 in the developing procedure). On these images, the particles are from 4 to 10 mm in size. Two images from different locations on each grid were prepared to check/ensure that, at least on the prepared grid, the particle size is homogeneous to some extent.

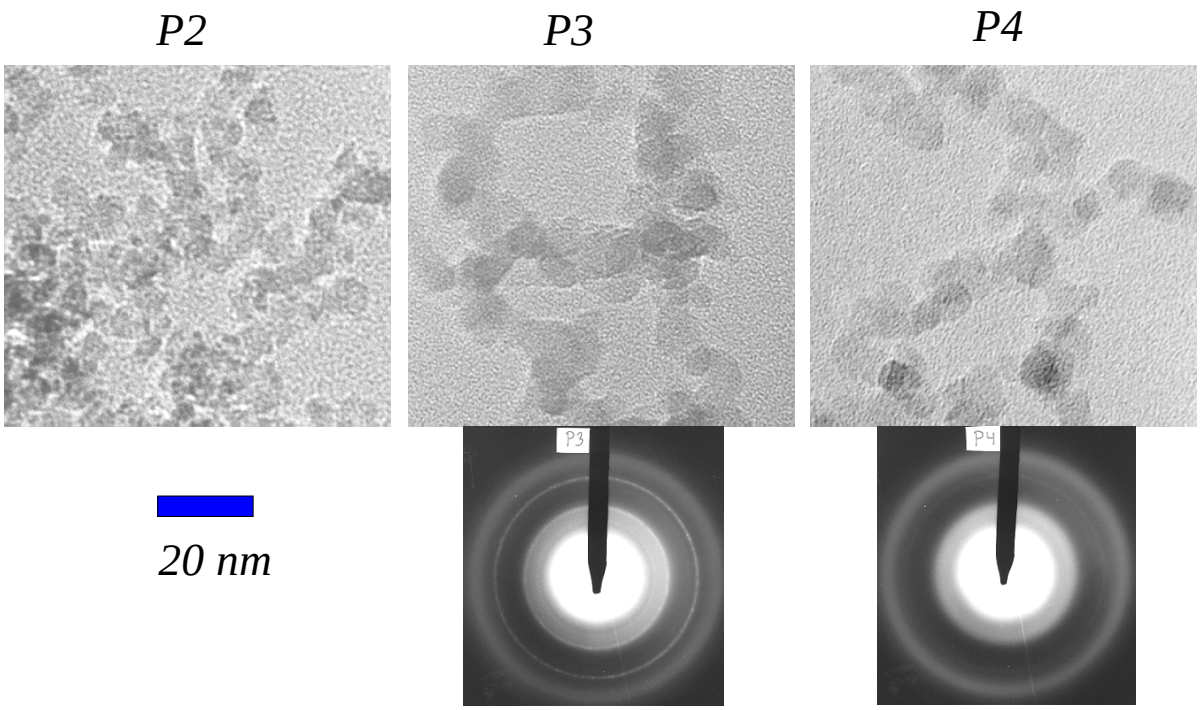

Figure 5 *High magnification TEM images of aggregates consisting of partially coalesced primary particles from experiments P2, P3 and P4. Operating conditions are listed in table 5.2. The primary particles are slightly bigger for P3 and P4 (low jet velocity). For P3 and P4, the corresponding diffraction image are shown. For P3, there is a vague diffraction ring indicating crystalline of material, which is more or less disappeared in P4.*

From the specific surface area measurements, the equivalent primary particle size was calculated [cf. table 5.4] and those values are compared with the results of the sizes measured on the TEM images.

There is a good correlation between the *SSA* and TEM results on figure 5.16. The size measured by TEM seems to follow the trend of the equivalent size computed from the *SSA* data. For each experiment, the *SSA*-equivalent size is slightly larger than the TEM size, which probably is due to the loss of surface area between necked primary particles. This was also the case for the diffusion flame experimental data shown on figure 5.7, page 40. The effect of neck formation between particles on the particle size computed from *SSA*-data is discussed on page 40.

The effect of operating conditions on the primary particle size has the expected trend, but not to the extent one would expect based on the measured temperature profiles.

Based on the results of experiments P3 and P4, the primary particle size is almost unaffected by

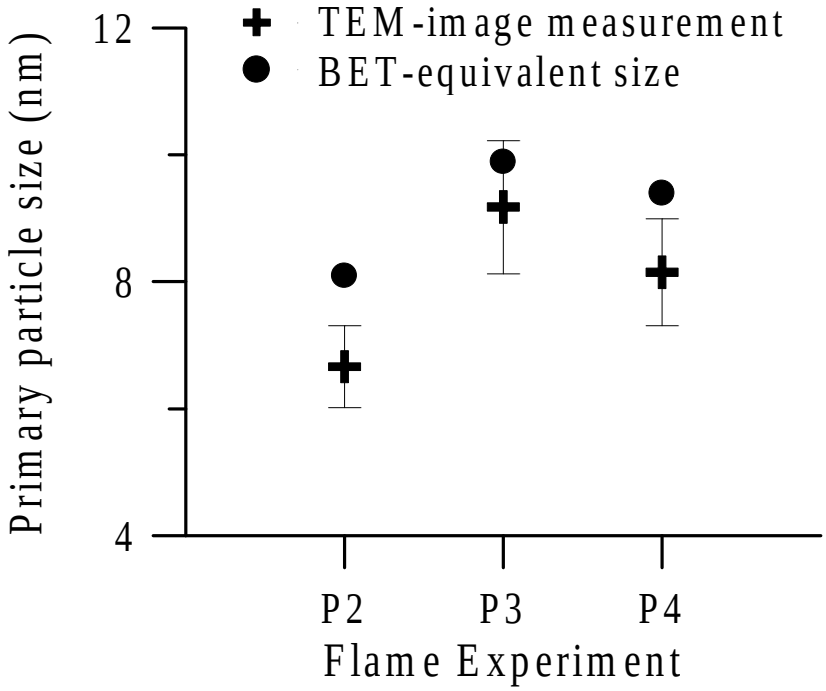

Figure 5 *The primary particle size of alumina in the premixed burner calculated from the specific surface area and measured on TEM images. The standard deviation on the TEM measurements are shown as error bars.*

the quenching but we see a change in crystallinity. Therefore, the primary particle size must be determined before the jet passes through the quenching zone. For P3, the jet residence time above the quenching ring is at a higher temperature level than for P4. This difference, which is shown on figure 5.13, must be high enough for a slight phase transformation but insufficient for a significant change of particle size.

5.2.4 Particle size distributions

Particle size distributions are measured at two different saturator temperatures. The two graphs on figure 5.17 and 5.18 show distributions for experiments P1, P2, P3 and P4. Figure 5.18 shows size distributions for the experiments on the preceding page, i.e. with a saturator temperature of 160°C. Figure 5.17 shows size distributions for identical experimental conditions, except the saturator temperature, which is 120°C.

The outlet size distributions measured with $T_{saturator}$=120°C [cf. figure 5.17] are, unlike the specific surface area, highly dependent on the jet velocity and the quenching flow. The standard errors on the measurements are shown on the figure as dotted lines, and the differences between

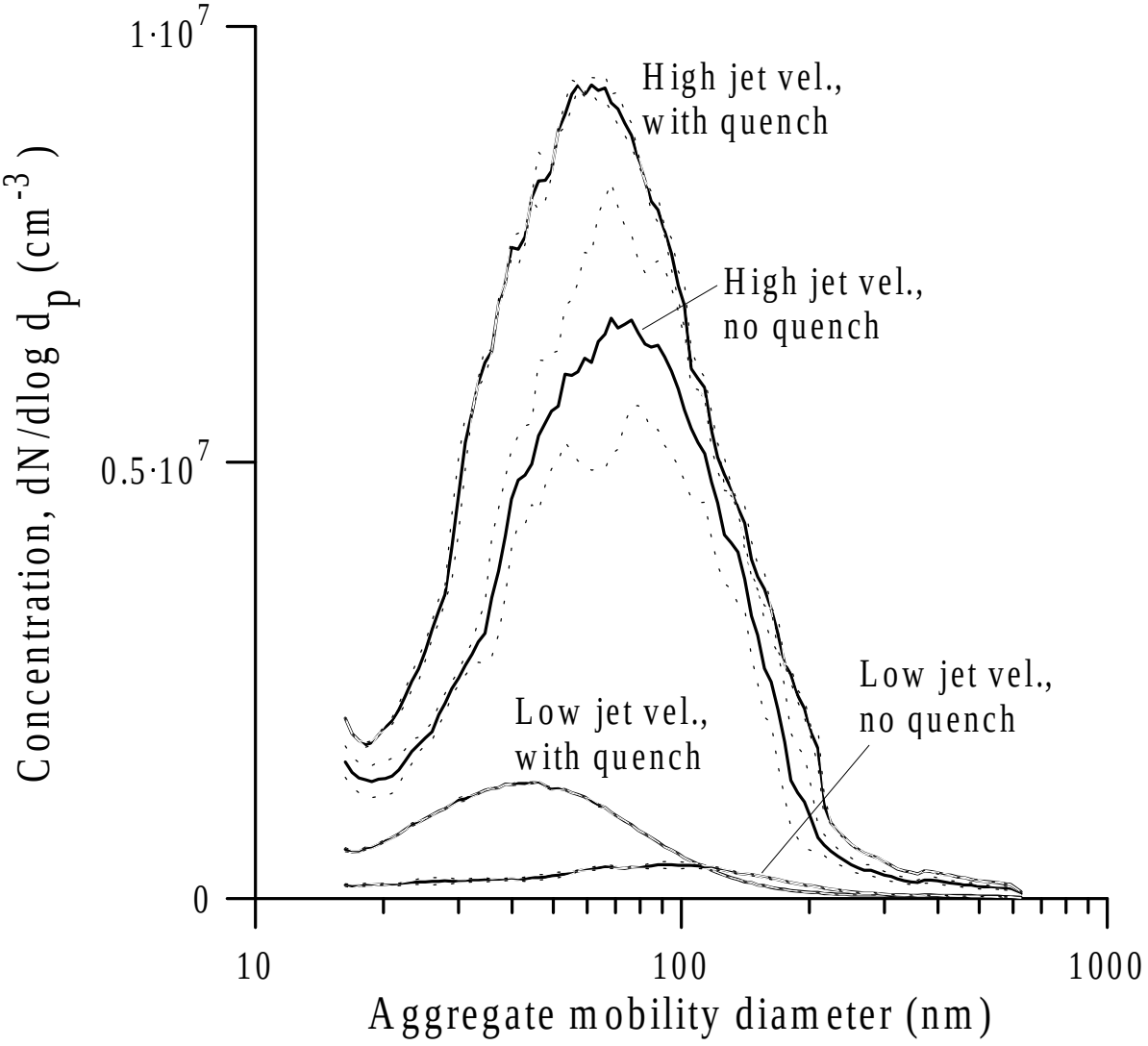

Figure 5 *SMPS size distributions measured at the process outlet. The saturator temperature is 120°C, but otherwise the operating conditions are as in table 5.2. The standard errors on the measurements are shown as dotted lines. The jet velocity and the quenching have a large effect on the outlet size distributions.*

the individual measurements are significant. The quenching reduces the coagulation downstream from the quenching point. From P1 to P2 (high jet velocity with and without quenching) the mean aggregate diameter is slightly reduced from 67 nm to 64 nm and from P3 to P4 (low jet velocity with and without quenching), the mean aggregate diameter is reduced from 72 nm to 46 nm. The more drastic effect is seen for P3 to P4, which is caused by the long particle residence time for case P3. For case P4, the coagulation rate is reduced after the quenching and the difference from P3 becomes significant.

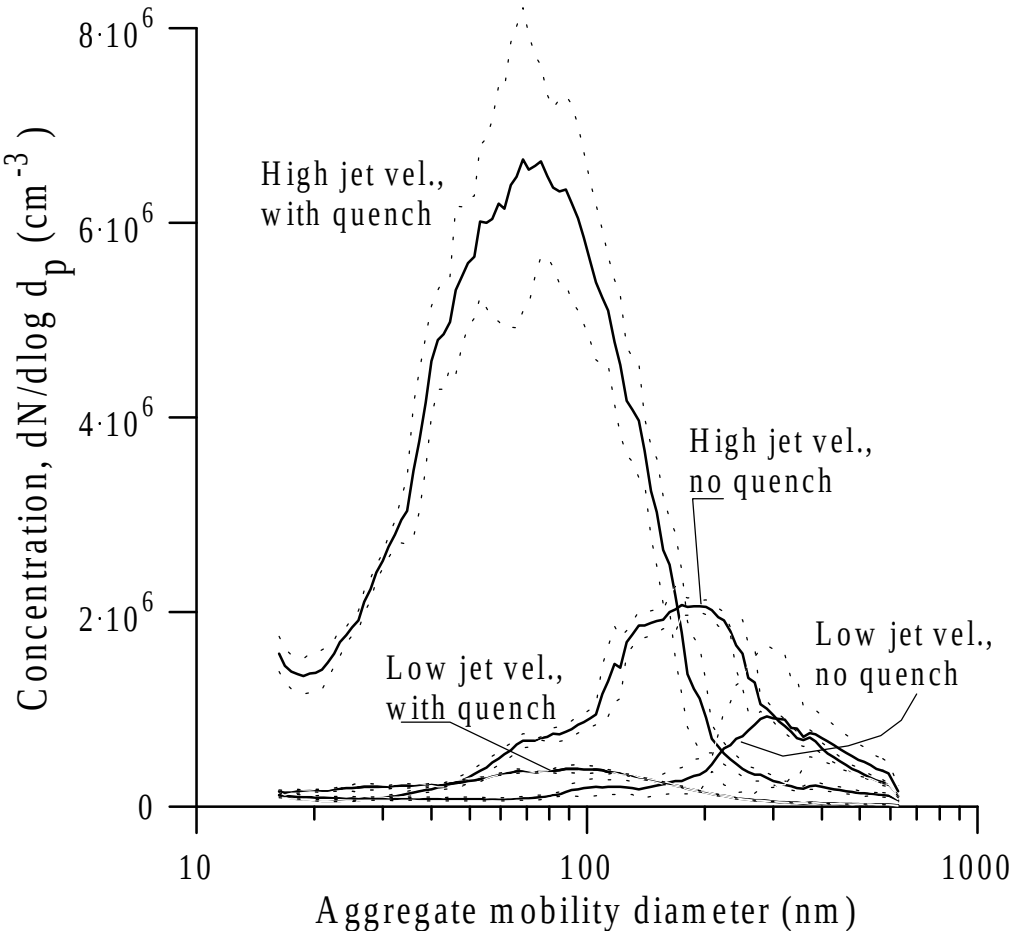

Figure 5 *SMPS size distributions measured at the process outlet. The saturator temperature is 160°C, as in table 5.2. The standard errors on the measurements are shown as dotted lines. Both the jet velocity and the quenching have a large effect on the outlet size distributions.*

Figure 5.18 shows similar measurements, but with the same saturator temperature as in the specific surface area experiments ($T_{saturator}$ = 160°C, table 5.2). For these experiments, the mean aggregate diameters are: P1: 162 nm , P2:173 nm , P3:214 nm , P4:157 nm.
Here we see, as for the previous experiments, that the quenching reduces the aggregation from case P3 to P4. The quenching in cases P1 and P2 actually increases the mean aggregate diameter. This unexpected behaviour might be a combination of two things:

- The quenching breaks up/slows the jet, causing the effect of dilution to be outweighed by the increase in residence time.

- The quenching reduces the outlet temperature, causing a decrease in the dilution ratio in the ejector. This can disturb the comparison between the two cases.

Still, the quenching has a much more significant effect on the evolution of the aggregate size distribution than on the specific surface area.

By use of the ejector, we can reduce the aggregate formation rate. Another advantage is that the decrease in temperature upstream from the ejector probably will cause newly formed aggregates to be more loosely connected. Neck formation between particles in two collided aggregates, which is the initial part of coalescence, is temperature dependent.

5.2.5 Radial variation of outlet concentration

All size distributions shown in the previous section were measured at the centre line of the quartz tube outlet. The radial dispersion of particles is studied by measuring additional size distributions with the tip of the ejector probe positioned by the wall right at the inner side of the quartz tube.

A schematic of the two different measuring locations at the premixed burner outlet is shown on figure 5.19. The quenching ring is not shown on this drawing.

By comparing the total concentrations at the two positions for each of the four operating conditions, we get a measure of the radial transport of particles.

The results are summarized in table 5.5. The ratio of the concentrations measured at the two positions is computed based on the total number concentration from the SMPS data.

Since the temperature variation across the outlet is low, the ejector dilution can be assumed constant for these comparisons. The sampling at different locations yields a local value since the volumetric flow rate in the sampling tube is below 0.3 l/min and the total gas flow at the outlet is above 10 l/min. Therefore, the disturbance of the flow by the ejector is insignificant.

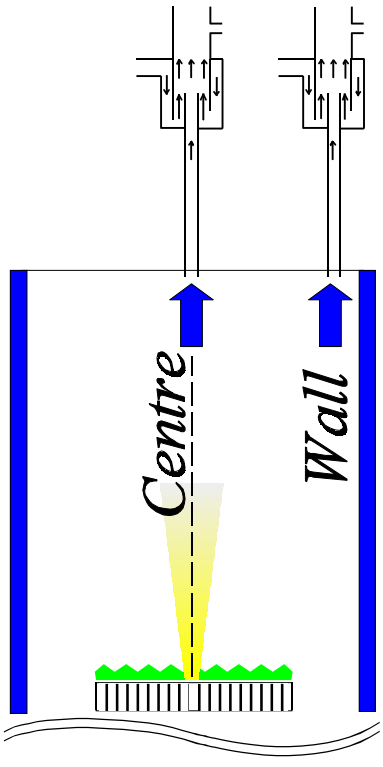

Figure 5 *The two different ejector sampling positions: At the centre line and at the inner side of the quartz tube.*

Table 5.5 *For the four premixed burner experiments, the*

ratio of the total concentrations at the centre line, $N_{Total, Centre}$, and at the quartz tube wall, $N_{Total, Centre}$, is computed. For P1 and P2, the concentration is constant across the entire tube, whereas for P3 and P4, the concentration is slightly higher at the centre-line. The high concentration close to the wall at the outlet confirms that there is a significant radial dispersion of particles.

Experiment	P1	P2	P3	P4
$N_{Total, Centre}/N_{Total, Wall}$	1.04	0.98	3.2	2.1

The low lateral variation of the total particle concentration across the quartz tube outlet confirms the significant radial dispersion of particles in the process. We cannot conclude that the particle properties will be uniform at the outlet, only that the particulate matter at the outlet has been dispersed radially far beyond the core region of the jet. Closer to the flame, of course the difference between the particle concentration at the centre line and by the wall is large.

Table 5.6 shows the mean aggregate size based on the same measurements. The mean aggregate size decreases from the centre line to the wall. A likely explanation is that the highly dispersed aggregates close to the wall have experienced a lower coagulation rate due to the lower particle concentration along the outermost trajectories.

Table 5.6 *For the four premixed burner experiments, the mean aggregate size is measured at the centre line and close to the quartz tube wall. For all experiment, the aggregate size from the SMPS data is lower close to the wall than at the centre line.*

Experiment	P1	P2	P3	P4
Mean agg. diam. (centre line), nm	162	173	214	157
Mean agg. diam. (wall), nm	137	158	190	116

6 CFD simulation of flames

Recent works on particle modelling in flames have employed a coagulation-coalescence model for particle dynamics [cf. Chapter 3] combined with either an assumed or measured temperature profile (e.g. Kruis et al., 1993, Windeler et al., 1997, Yang and Biswas, 1997). In this approach one needs information about the velocity field to compute the coupling between temperature and time, since temperature is measured as a function of distance and the independent variable in the particle equations is time.
Furthermore, the particles are often formed in jets, where there can be a significant degree of lateral mixing of the gases resulting in a dilution of the particles. Since the coagulation rate is highly sensitive to changes in concentration, the knowledge of gas mixing is important.

In the present study, the approach is to use a computational fluid dynamics (CFD) code to simulate the gas temperature and velocity profiles of the burners. Once the flow, temperature and composition fields from the CFD simulations are known, the particle model can be integrated along characteristic trajectories. The particle model and the implementation in the flow fields will be discussed later.
The bulk flow of combustion gases with little error can be assumed independent of the aerosol dynamics, since the mass loading of particles is at least two to three orders of magnitude smaller than the mass flow of gasses.

This chapter serves as an introduction to the CFD method. The general method for computational fluid dynamics is presented. Fundamental equations, which are solved in a computational grid are also discussed. Finally, selected results of the simulations of both the diffusion flame burner and the premixed burner are presented and compared with temperature measurements within the flame.

6.1 Fundamentals of CFD

Computational fluid dynamics is a method for simulating a wide range of physical/chemical systems by solving the fundamental equations for flow, heat- and mass-transfer in a computational domain similar to the actual geometry of the physical system.

The solver used in this study is the commercially available CFD solver, Fluent (Fluent Inc., 1996).

The principal governing equations, which form the basis for the calculations are shown below. For further details, readers are referred to the software manuals (Fluent Inc., 1996) and the text books by Bird at al. (1960) and Fletcher (1997).

6.1.1 Conservation equations

The conservation energies are presented in the following in the vector-tensor form similar to Bird et al. (1960). In this notation, scalars are lightface italic, vectors are boldface italic and tensors are boldface Greek.

Some typical examples of

- scalars are: Temperature, T, mass fraction, m_i, or enthalpy (h).
- vectors are: Velocity ($\boldsymbol{u}$), momentum, force or the vector differential operator,∇
- tensors are: The shear stress tensor,$\boldsymbol{\tau}$, or momentum-flux tensor.

Some of the important vector-tensor operators are:

- The scalar product ("$\cdot$") between two vectors results in a scalar.
- The scalar product ("$:$") between two tensors results in a scalar.
- The scalar product ("$\cdot$") between a vector and a tensor results in a vector.
- The dyadic multiplication of two vectors, e.g. $\boldsymbol{uu}$, results in a tensor.

The conservation of mass is given by

$$\frac{\partial \rho}{\partial t} + \nabla \cdot \rho \boldsymbol{u} = S_m \qquad \textbf{(6)}$$

where ∇ is the vector differential operator known as "nabla" or "del", ρ is the fluid density, $\boldsymbol{u}$ the velocity vector and S_m a source term for mass added to the continuous phase, e.g. from evaporation of a dispersed second phase. For momentum, the conservation is given by

$$\frac{\partial}{\partial t}(\rho \boldsymbol{u}) = -\left[\nabla \cdot \rho \boldsymbol{u}\boldsymbol{u}\right] - \nabla p - \left[\nabla \cdot \boldsymbol{\tau}\right] + \rho \boldsymbol{g} + \boldsymbol{F} \qquad \textbf{(6)}$$

where p is the static pressure,$\boldsymbol{\tau}$ is the stress tensor, and $\boldsymbol{g}$ and $\boldsymbol{F}$ are vectors of gravitational acceleration and external body-forces respectively. The physical meaning of the first three terms on the right-hand side are: Rate of momentum gain by convection, pressure force on a fluid

element per unit volume and the rate of momentum gain by viscous transfer per unit volume. Any number of chemical species can be specified, and for species *i*, the conservation equation is:

$$\frac{\partial}{\partial t}(\rho m_i) + \nabla\cdot\rho m_i \boldsymbol{u} = \nabla\cdot\boldsymbol{J_i} + S_i \qquad \textbf{(6)}$$

where m_i is the mass fraction of species *i*, $\boldsymbol{J_i}$ the diffusive mass flux of species *i* and S_i the net rate of production of species *i* per unit volume from chemical reaction or contribution from a dispersed phase.

The diffusion mechanisms included in the models are diffusion due to concentration gradients and thermal effects. Pressure diffusion is neglected, and the equation for the diffusive mass flux $\boldsymbol{J_i}$ vector becomes:

$$\boldsymbol{J_i} = -\nabla\cdot\rho D_{i,m}\nabla m_i - D_{i,T}\frac{1}{T}\nabla T \qquad \textbf{(6)}$$

where $D_{i,m}$ is the diffusion coefficient for species *i* in the gas mixture and $D_{i,T}$ is the thermal diffusion coefficient.

For the conservation of energy, the static enthalpy, *h*, is employed:

$$h = \sum_i m_i h_i \quad , \text{ where } h_i = \int_{T_{ref}}^{T} c_{p,i}\, dT \qquad \textbf{(6)}$$

T_{ref} is a reference temperature and $c_{p,i}$ is the specific heat capacity of the species *i*.

Again, neglecting pressure diffusion, the transport equation for energy, a scalar, becomes:

$$\frac{\partial}{\partial t}(\rho h) + \nabla\cdot\rho h\boldsymbol{u} = \nabla\cdot k_c\nabla T - \nabla\cdot\sum_j h_j\boldsymbol{J_j} + \frac{\partial p}{\partial t} + \boldsymbol{u}\cdot\nabla Dp - \boldsymbol{\tau}:\nabla\boldsymbol{u} + S_h \qquad \textbf{(6)}$$

where k_c is the thermal conductivity, S_h is a source term describing enthalpy sources such as reaction heats, radiation and heat exchange with a dispersed second phase. The two first terms on the right-hand side are the transport of enthalpy by conduction and by species diffusion. The term $\boldsymbol{\tau}:\nabla\boldsymbol{u}$ is the scalar product of the stress tensor and the divergence of the velocity vector, which is also a tensor. The physical significance of this term is the irreversible rate of energy increase by viscous dissipation.

Conductive solid regions, e.g. a tube wall separating hot and cold gases, are accounted for by an

equation of conduction, which includes heat flux resulting from conduction and volumetric heat sources within the solid, given by

$$\frac{\partial}{\partial t}\rho_w h_w = \nabla \cdot k_w \nabla T + \dot{q} \qquad \textbf{(6)}$$

where ρ_w is the wall density, h_w wall enthalpy, k_w wall conductivity, T wall temperature, and $\dot{q}$ the volumetric heat source.

6.1.2 Turbulence models

By employing a time-averaging procedure, Reynolds averaging (Hines, 1975), the conservation equations for laminar flow can be modified to include effects of turbulent fluctuations.
Variables in turbulent flow are described by the sum of a mean (time averaged) and a fluctuating value. For, e.g. the velocity $\boldsymbol{u}$ we have:

$$\boldsymbol{u} = \overline{\boldsymbol{u}} + \boldsymbol{u}' \qquad \textbf{(6)}$$

Here, the over-lined symbols represent the time averaged values and " ´ " is the fluctuating component.
The time-averaging procedure yields the following equation for the momentum conservation:

$$\frac{\partial}{\partial t}(\rho\overline{\boldsymbol{u}}) = -\left[\nabla \cdot \rho\overline{\boldsymbol{u}}\,\overline{\boldsymbol{u}}\right] - \nabla\overline{p} - \left[\nabla\cdot\overline{\boldsymbol{\tau}}\right] - \left[\nabla\cdot\overline{\boldsymbol{\tau}}'\right] + \rho\boldsymbol{g} + \boldsymbol{F} \qquad \textbf{(6)}$$

The only difference between equation 6.2 and 6.9 is the term $[\nabla\bullet\overline{\boldsymbol{\tau}}']$ which represents the rate of momentum gain by turbulent fluctuations. The individual components of the turbulent momentum flux tensor, $\overline{\boldsymbol{\tau}}'$, are in an (x,y,z)-coordinate system of the form:

$$\overline{\tau_{xx}}' = \rho\,\overline{u_x' u_x'} \quad ; \quad \overline{\tau_{xy}}' = \rho\,\overline{u_x' u_y'} \quad ; \ldots etc. \qquad \textbf{(6)}$$

The individual components in equation 6.10 are usually referred to as Reynolds stresses.
The conservation equation with turbulence included for a given scalar, ϕ, is based on the same time-averaging procedure.
With the x-direction as an example, the result is:

$$\frac{\partial}{\partial t}\left(\bar{\rho}\,\bar{\varphi}\right) + \frac{\partial}{\partial x}\left(\bar{\rho}\,\bar{u}_x\,\bar{\varphi}\right) = \frac{\partial}{\partial x}\left(\bar{\rho}\,\overline{u_x'\varphi'}\right) + D(iffusion)_{\varphi} + S(ource)_{\varphi} \qquad \textbf{(6)}$$

where ρ is the density, u_x is the velocity in the *x*-direction, *t* is time, over-lined variables are time averaged values, and variables with superscript " ´ " are fluctuating. The first term on the right-hand side, $\bar{\rho}\,\overline{u_x'\varphi'}$, is the correlation term for turbulence. Physically this term represents the transport or "diffusion" of ϕ due to turbulent fluctuations.

Modelled by the gradient transport analogy, the correlation yields the following equations for the effect of turbulence on species conservation and enthalpy conservation, here for the x-direction:

$$\rho\,\overline{u_x' m_i'} = -\frac{\mu_t}{\sigma_m}\frac{\partial m_i}{\partial x} \qquad \textbf{(6)}$$

$$\rho\,\overline{u_x' h_i'} = -\frac{\mu_t}{\sigma_h}\frac{\partial h_i}{\partial x} \qquad \textbf{(6)}$$

where the over-lined variables are time averaged values, m_i is the mass fraction of *i*th species, h_i is the enthalpy for the *i*th species and σ_m is the turbulent Schmidt number and σ_h is the turbulent Prandtl number. The value of both numbers is 0.7, which is determined empirically. The turbulent viscosity is determined by the two parameters, *k*, the turbulent kinetic energy and, ϵ, the rate of dissipation of *k*:

$$\mu_t = \rho C_\mu \frac{k^2}{\varepsilon} \qquad \textbf{(6)}$$

where C_μ is an empirical constant equal to 0.09. The values of k and ϵ are obtained from turbulence models.

Added to the molecular viscosity, μ, the effective viscosity is given by:

$$\mu_{eff} = \mu_t + \mu \qquad \textbf{(6)}$$

The modified steady state scalar equations consist of a convection term, a source term and a diffusion term, where the diffusion term now includes both the effect of molecular diffusion and effects caused by turbulent fluctuations. For the case of species diffusion, there will be two dominant mechanisms: Molecular diffusion driven by concentration gradients and turbulent

diffusion due to transport by turbulent eddies. The important issue of the turbulent fluctuations is, that all species, both small particles and molecular species, will be transported by the same rate in turbulent diffusion.
Usually, the concept of a model for turbulence is to relate the Reynolds stresses, the turbulent momentum fluxes, to the mean flow quantities. Two such models, the k-ϵ model and the Reynolds Stress Model (RSM), will briefly be described below.

The k-ϵ model is an eddy-viscosity model, where the Reynold stresses are assumed proportional to the mean velocity gradients. The proportionality constant is the turbulent viscosity, μ_t.
The values of k, the turbulent kinetic energy, and ϵ, the rate of dissipation of k, are obtained by solving conservation equations for the two parameters. The limitation of the k-ϵ model is that the turbulent viscosity is isotropic. Therefore, velocity and length scales for turbulence become equal in all directions. For some systems with sudden expansions, swirling flows, or flows with regimes of both high and low Reynolds, this is not adequate. The k-ϵ model can however provide a starting point for the more computationally demanding RSM.
The RSM computes Reynolds stresses in each direction from individual differential transport equations, which makes this is a more computationally demanding method. The turbulent kinetic energy is computed based on the values of the stresses.
The total number of stresses in the turbulent stress tensor, $\bar{\bar{\tau}}'$, is nine, but due to the symmetry of $\bar{\bar{\tau}}'$ ($\tau_{xy} = \tau_{yx}$), the number of additional equations needed to be solved for the RSM is six and one additional equation for the dissipation rate, ϵ.

The main difference between the two models is the way the values of k and ϵ are obtained in relation to the stresses.
In this study, the RSM model is used.

6.1.3 Reacting flows

The rate of chemical reaction for turbulent flows is controlled either by the Arrhenius kinetic expression or by the mixing of the reactants in turbulent eddies.
Even though the combustion of methane consists of many radical reactions, a full implementation in CFD is not practically possible. Firstly, the number of species to solve in the system increases the computational time considerably. Secondly, the improvement of the accuracy by employing the detailed kinetic model is probably limited by the accuracy of other models, e.g. the turbulence model.
Therefore, a global first-order Arrhenius rate expression is employed for the kinetic rate of methane oxidation. The influence of turbulent mixing is calculated by the Magnussen and Hjertager (1976) eddy breakup model, which relates the rate of reaction to the dissipation rate of product and reactant containing eddies.
For both regimes, the reaction rate is calculated and the limiting value is used.

6.1.4 Radiation

For high temperature processes, radiation becomes important. Radiation is taken into account by the so-called P-1 model (Siegel and Howel, 1992), in which the radiation flux is expressed by expanding the radiation intensity in series of orthogonal harmonics. The radiation flux is then directly incorporated in the enthalpy balance to account for the radiation transfer process.
However, two radiation models are available in the commercial CFD code, Fluent (Fluent Inc., 1996): The already mentioned P1 model and the Discrete Transfer Radiation Model (DTRM). The DTRM uses integration of radiation properties along ray-traces originating from each wall cell in discrete number of angles. This model is demanding in terms of CPU-time and since the difference between the peak flame temperature of the two models was insignificant, the faster P1 model was applied.

6.1.5 Physical parameters

The essential physical parameters for the flame calculations are:
Specific heat capacity, thermal conductivity, binary diffusion coefficients, molar masses (molecular weights), formation enthalpies, viscosity and parameters for the kinetic theory of

gases. Physical data, which are either not available or difficult to implement, can be estimated based on the kinetic theory of gases.

The maximum flame temperature is an essential characteristic of the flame. Therefore, reliable temperature functions of the heat capacities of the individual species is important.

The burners operate at atmospheric pressure, and the density is therefore calculated by the ideal-gas law.

Various equations for computation of physical parameters in the simulations are listed in Appendix A.

6.1.6 Boundary conditions

In CFD simulations, the computational domain has boundaries similar to the physical system. The boundary conditions are of the following types:

Inlets*:* Velocity, composition, temperature, turbulence parameters etc. are specified for the fluid flowing into the domain. The parameters for turbulence are the turbulent intensity and the characteristic length of the inlet.

Wall: The fluid velocity is usually zero at the wall surface (no slip). The possible thermal boundary conditions of the walls are: Fixed temperature, fixed heat flux or a specified heat transfer coefficient with a temperature gradient determined by the wall temperature and an external temperature. Wall-cells can also be "live" cells where conduction of heat from one fluid to another through the wall takes place. For these cells, equation 6.7 is used.

The near-wall treatment of turbulence is employed by the so-called wall-functions (see Fluent Inc., 1996). In the commercial CFD-code, there are two available approaches: The standard wall function and the non-equilibrium wall function. To avoid any misunderstandings, "non-equilibrium" has no connection to non-steady state. In this work, the non-equilibrium wall function is used. This approach is recommended for complex geometries and wall bounded turbulent flows (Fluent Inc., 1996).

Outlet: The exit of the fluid. The outlet can be specified either as a single outflow boundary zone or multiple outlets with different levels of static pressure at each outlet. The difference in static pressure determines the fraction of the fluid that flows through each outlet zone. Outlets should be placed where moderate/low gradients exist in order to obtain a rapidly converging solution.

Symmetry: 3D problems with rotational symmetry, e.g. a vertical tube reactor, can be solved with a 2D grid where the axis of symmetry on the 2D plane is specified as a rotational symmetry boundary. Plane-symmetry is also an option. If possible, any symmetry in the system should be used to save computational time by minimizing the complexity of the computational domain.

6.1.7 The solver

The complete system of equations is solved using a control-volume-based technique (Fluent Inc., 1996). This technique is based on:

- division of the physical domain into discrete control volumes: The computational grid.
- integration of the governing equations on the individual control volumes, which results in algebraic finite difference equations for the discrete unknowns, like velocity, pressure, species etc.
- solving the discretized equations and obtaining a steady state solution, where the residuals are suitably low.

The solution procedure is either a line-by-line solver (Line Gauss-Seidel, LGS) or a multi-grid solver (MG). In the LGS solver, the solution propagates in the flow direction whereas the MG solver operates in several grid levels and swaps between different refinement levels. Large scale errors are more easily reduced on a coarse grid, while the local errors are reduced at the fine grid level.

The solving technique will not be discussed in further detail. Additional information about the solution procedure is found in Fluent Inc. (1996).

6.2 The computational grids

The grid divides the domain into a number of "control volumes" in which the equation system is solved. Solution accuracy and CPU time both increase with the number of cells. The effect of increasing the number of cells can be investigated during the simulation process. If the final result is dependent on the number of lines in the grid, the grid needs to be refined. Often, minor regimes with large gradients are the grid locations, where refinement should be considered.

The two physical systems to be studied in this work are the diffusion flame burner and the premixed burner with the jet. The diffusion burner has an obvious rotational symmetry.

The premixed burner is almost rotationally symmetric, but the five individual jets in the quenching device cause the system to deviate from the ideal symmetry. However, a complex 3D simulation is avoided by changing the five quenching outlets into a slit rotated around the axis in the 2D computational domain. The width of the slit is chosen such that the kinetic energy of the air at the slit outlet is equal to the energy of the five small jets for the same volumetric flow rate. The physical meaning of this approximation is shown on figure 6.1. The outline of the grid is constructed from a CAD drawing of the physical domain and the actual grid is created in a separate mesh program, where the domain is divided into quadrilateral (2D) or hexahedral (3D) mesh. The grids for the two different burners are shown on figures 6.2 and 6.3. In each case, a

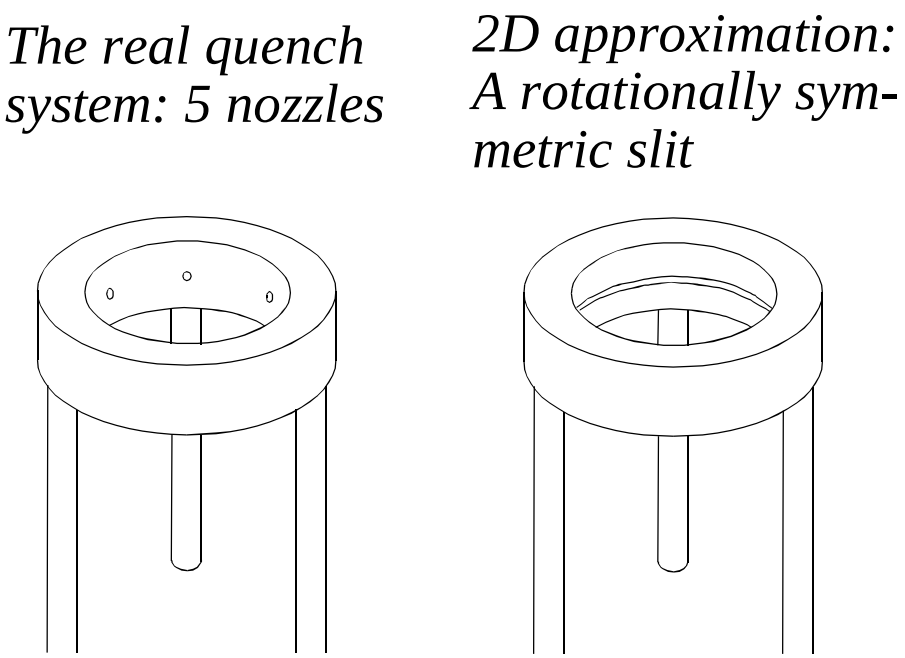

Figure 6 *The difference between the real quenching ring and the 2D rotationally symmetric approximation. In the 2D approximation, the five nozzles are modelled as a rotational slit. This enables a 2D simulation with a computational grid with a centre symmetry line.*

non-changing part of the grid between inlets and outlet is left out. Both grids are refined in areas where large gradients exist. In a structured grid like the ones on figures 6.2 and 6.3, each grid-line continues through the entire domain. This creates high grid resolution in areas with low

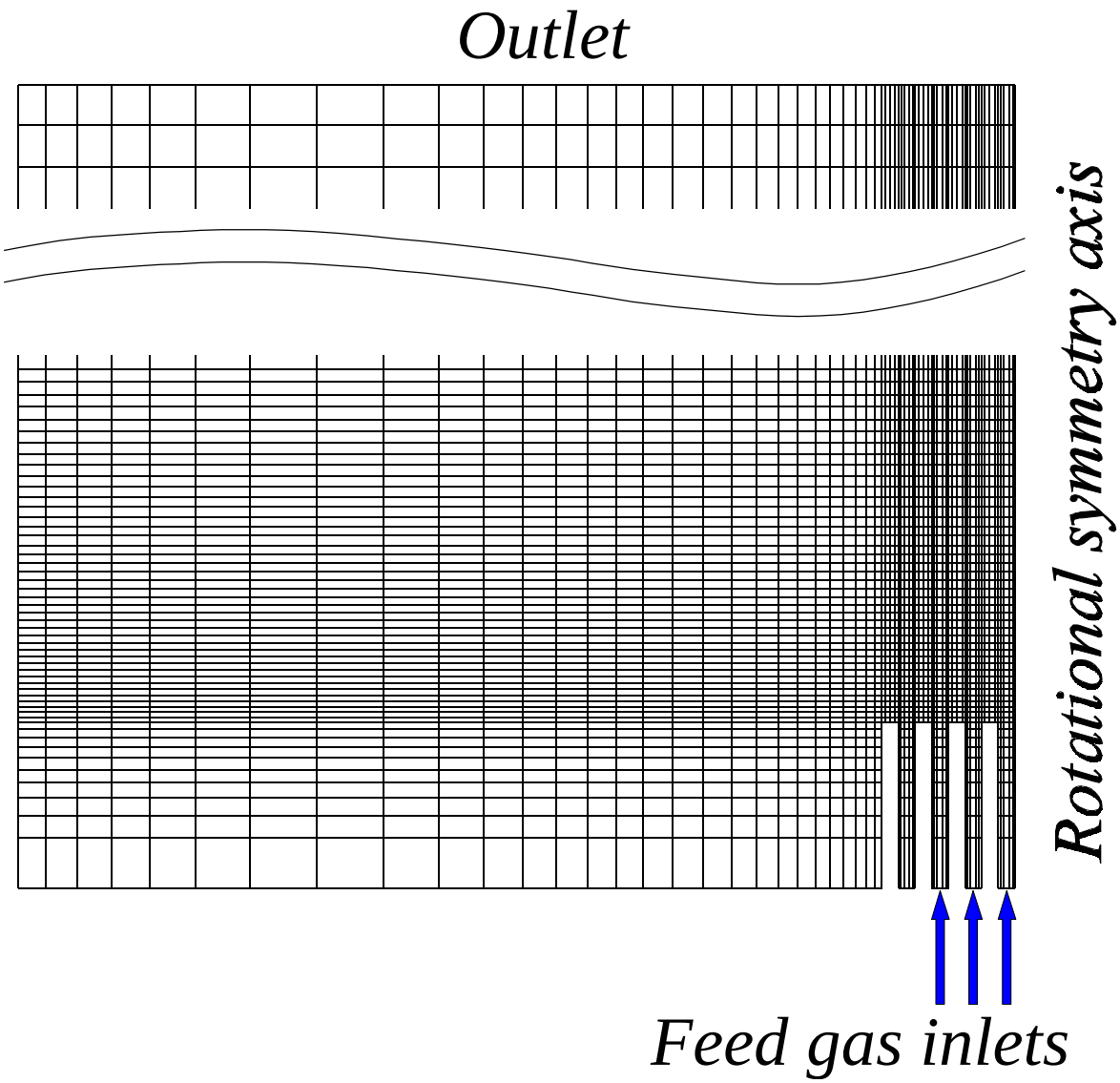

Figure 6 *The computational grid for the diffusion flame burner. Part of the grid above the burner mouth and the outlet is left out. For this burner, there is complete rotational symmetry around the axis. The grid is detailed in areas, where large gradients exist.*

gradients, e.g. the area to the left of the inlets in figure 6.2. This is a typical disadvantage of structured grids. It should be mentioned that the sufficiency of the grid resolution was investigated by observing the effect of increasing the number of cells in the axial and radial direction by a factor of two. The increase in grid size did not cause any significant changes in flow and temperature patterns and the grid resolution is concluded to be beyond the point of numerical influence.

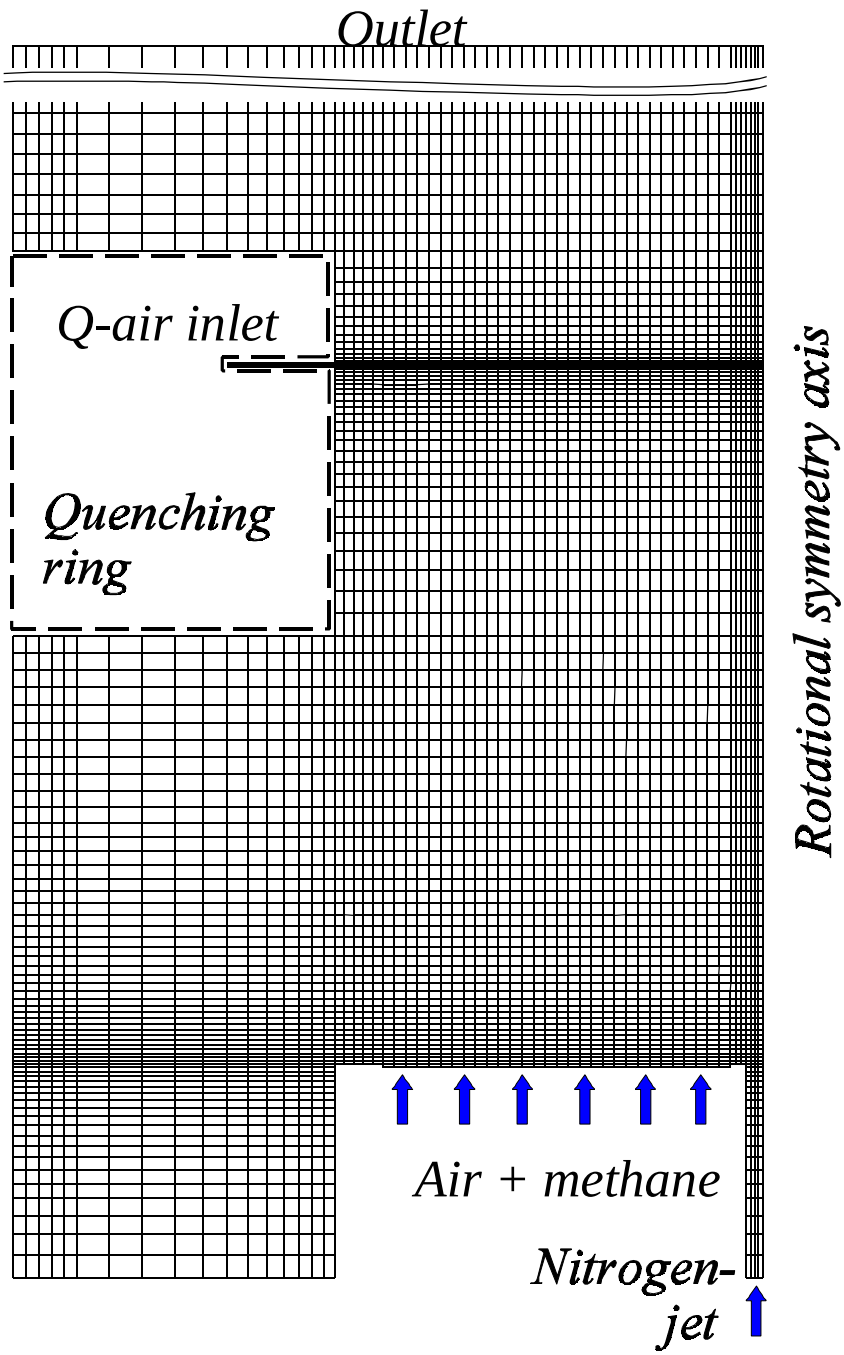

Figure 6 *The computational grid for the premixed burner, with the section between the quenching and the outlet left out. The grid is detailed in areas, where large gradients exist. Rotational symmetry for the quenching ring is obtained by creating a slit instead of five jets and the gab of the slit is determined to match the kinetic energy of the quenching air is for the five small jets. This is obtained when the area of the slit is equal to the area of the five circular jets.*

6.3 Simulating radial dispersion of particulate matter

In both flame systems in this work, the precursor enters the flame in a central jet/tube. Radial variation and dispersion can cause the particles to experience different temperature histories and this can result in a variation of outlet particle properties. This was seen in the TEM images of particles from the double diffusion flame in chapter 5.1.4.

A complete inclusion of the aerosol transport and dynamics in the CFD simulations is not expedient but the transport of particles can be simulated precisely by the following approach.

The Brownian diffusion coefficient of particles is low compared with the molecular diffusion coefficient of gas molecules. However, the turbulent diffusion coefficient is identical for all substances. Therefore, in turbulent regions in the flame, the radial transport of particles is substantial and not limited by the low Brownian diffusion coefficient.

There are five gas components in the burner systems: CH_4, O_2, CO_2, H_2O and N_2. At each inlet, the mass fraction of each species is specified. The transport of particulate matter is simulated by adding an additional gas component, PM (Particulate Matter), to the nitrogen jet inlet. The inlet mass fraction of the PM-component is equal to the corresponding mass fraction of alumina in the jet. Relevant physical data for PM are:

Diffusion coefficient. The molecular diffusion coefficient of PM is fixed to $1 \cdot 10^{-8}$ m^2/s, which is so low that it ensures the molecular diffusion of PM to be negligible. This is in agreement with expected behaviour of the particles except possibly for a short genesis phase assumed to be of negligible significance.

Molecular mass. Equal to the molecular mass of Al_2O_3

Other data are virtually irrelevant, since the low mass fraction causes the flow of PM to be without any influence on the macroscopic flow field. The only important issue is the turbulent radial dispersion of PM.

6.4 Estimating heat contribution from ATSB

Because of the large amount of organic material per aluminum atom in ATSB, the oxidation of the organic material results in a minor heat contribution to the flame. This cannot be measured accurately because temperature measurements with the precursor present in the flame are impossible. The deposition of particles on the thermocouple wire disturbs the measurements.

However, the heat contribution from the oxidation is empirically estimated from the combustion

heat of methane compared with that of the butoxide groups in ATSB. Each molecule of ATSB has three butoxide groups, i.e. a total of twelve carbon atoms. The heat of combustion of twelve methane molecules would overestimate the heat content since some C-atoms are bonded to other C-atoms and to oxygen.

As a rough estimate, the combustion of the three butoxide groups corresponds to the combustion of six methane molecules. Methane is already a species defined in the simulations, and the heat of precursor oxidation can therefore be approximated by specifying the precursor inlet as nitrogen, PM and methane. The mass fraction of methane is computed from the mole fraction of the precursor. For a precursor saturation temperature of 160°C, the corresponding mass fraction of methane in the simulations is approximately 0.02 whereas the actual mass fraction of alumina is 0.008. In the simulations, the reaction rate of the precursor-methane is assumed to follow the rate expression for the methane from the fuel inlet. The approximation is necessary due to lack of rate data and physical data for ATSB.

The following sections, chapter 6.5 and 6.6, shows results of simulations for the two burners. Those results are obtained without additional methane in the precursor inlet, because the simulations are compared with experimental data without precursor present. For the particle dynamics calculations in chapter 8, the methane mass fraction corresponding to the amount of the precursor is specified in the inlet conditions for the CFD simulations.

The effect of adding methane has a minor effect on the temperature profiles due to the low mass fraction of the precursor and therefore on the corresponding mass fraction of additional methane. The difference in flame peak temperature with and without precursor-methane present never exceeds 50-75K.

6.5 CFD results: Diffusion flame burner

The presentation of the CFD simulations of the diffusion flames comprises contour-plots characterizing the flames and graphs comparing experimental data and simulations.

The reaction in the diffusion flame between CH_4 and O_2 is approximated by a single step reaction with an Arrhenius expression of the following form:

$$R_{CH_4} = A_{single} \exp\left(-\frac{E_{single}}{RT}\right) C_{CH_4}^{\ a} C_{O_2}^{\ b} \qquad \textbf{(6)}$$

The order of magnitude of the pre-exponential factor, A_{single}, and the activation energy, E_{single}, are

obtained from Bartok and Sarofim (1991): A_{single}= 1·10^{12}m^3/mole/s and E_{single}=125 kJ/mole. The values of the exponents *a* and *b* in the single step model are derived from flammability data. The recommended values (Bartok and Sarofim, 1991) are *a*= -0.3 and *b*=1.3, but the negative value for the methane concentration results in numerical problems in the simulations. Therefore, the stable first order dependence of each reactant, *a*=1 and *b*=1, is used. However, using wide ranges of the values of A_{single} and E_{single} does not affect the results, since the reaction in the diffusion flame is controlled by the turbulent mixing rates. Therefore, a more accurate Arrhenius expression was not pursued.

The eddy break-up model proposed by Magnussen and Hjertager (1976) comprises of two rate expressions. One describes the reaction rate by the mixing of reactants in turbulent eddies, when diffusive transport of species is the limiting factor. The other expression describes the mixing of hot product gases with cold reactant gases, when heat transport to unreacted gases is the limiting factor.

The two rate expressions are of the form:

$$R_{reactant-limited} \sim A_{MH}(\varepsilon/k)C_{reactant} \quad \textbf{(6)}$$

$$R_{hot/cold\ limited} \sim A_{MH}B_{MH}(\varepsilon/k)C_{products} \quad \textbf{(6)}$$

where A_{MH} and B_{MH} are the two empirical "Magnussen and Hjertager" constants, *C* is the concentration of either reactants or products, *k* is the turbulent kinetic energy and ϵ is the dissipation rate of turbulent kinetic energy. The factor ϵ/k represents the time scale of turbulent eddies. The "default" values of A_{MH} and B_{MH} are 4 and 0.5 respectively (Magnussen and Hjertager, 1976) but the values may depend on the flame structure. For different flames, they report values, which differ up to a factor of 8.

By observing the effect of the two empirical constants on the simulated flame structure and maximum flame temperatures, the best results are obtained when A_{MH} is approximately 10 and B_{MH} is approximately 1. These values are used in all simulations of diffusion flames in the present work.

6.5.1 Visual appearance of diffusion flames

The photographs of the flames from chapter 5.1.1 are compared with simulated temperature contour plots. Figure 6.4 shows the comparison for four different flame operating conditions. The operating conditions are listed in table 5.1. The absolute temperature of the flame is not directly comparable with the visual appearance of the flame, but with that in mind, the photographs compare well to the temperature contours for all flames. The difference between the double diffusion flames (B-flames) and the single diffusion flames (C-flames) is clear on the photographs and on the simulations.

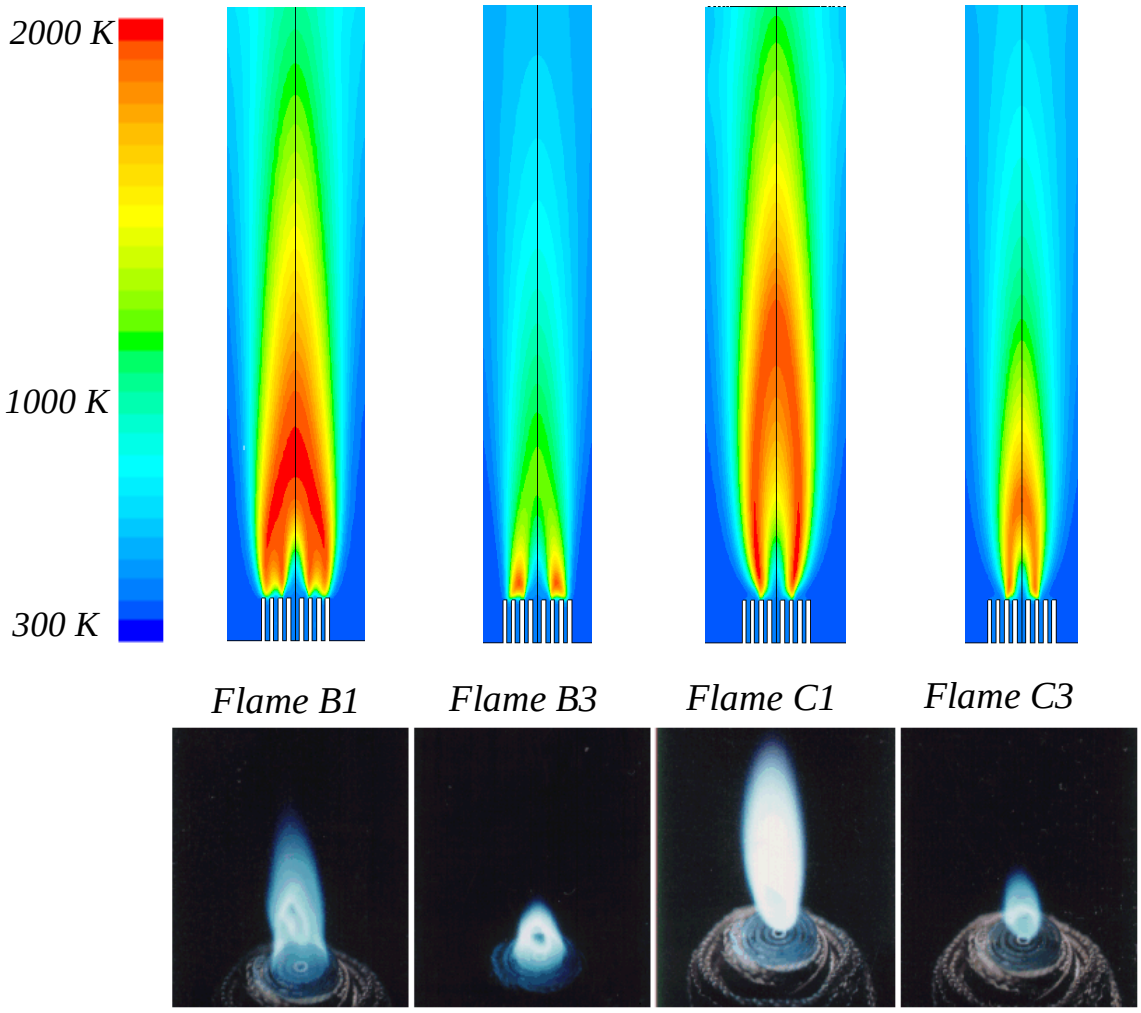

Figure 6 *Photographs of diffusion flames are compared with simulated temperature contour plots. The temperature scale in terms of colours is shown. The difference between double (B) and single (C) diffusion flames is clearly seen on both photographs and simulations. Operating conditions are listed in table 5.1.*

6.5.2 Temperature profiles

In figures 6.5 and 6.6, the two sets of temperature measurements from section 5.1.2 are compared with the profiles obtained from the simulations. Figure 6.5 is a comparison of the axis temperature profiles while figure 6.6 shows the maximum temperature as a function of height. In both cases, there is a good agreement between the measurements and the simulations. To measure the temperature of a flame is difficult, because the local temperature is measured in an environment of steep gradients and the thermocouple wire disturbs the flame. Therefore, the temperature measurements can be considered only as a guideline to the temperature pattern more than an exact measurement of absolute flame temperature. The good correlation between the simulations and the two sets of temperature measurements leads to the conclusion, that the reaction between methane and air in a diffusion flame with good approximations can be described by the eddy break-up model with parameters A_{MH} and B_{MH} equal to 10 and 1 respectively.

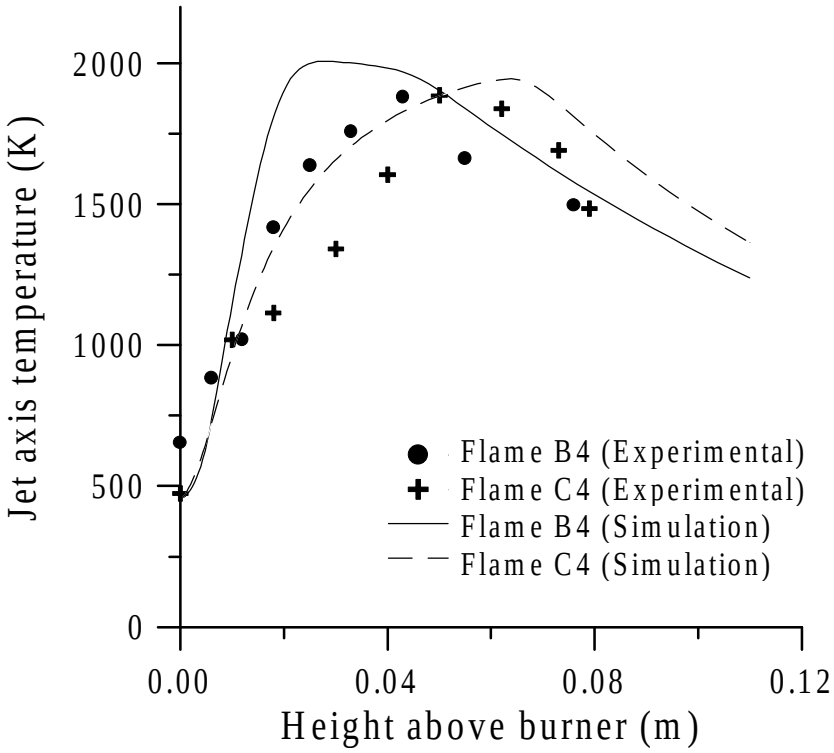

Figure 6 *Measured axis temperature profiles are compared with the profiles obtained from the simulations for flames B4 and C4. Operating conditions are listed in table 5.1.*

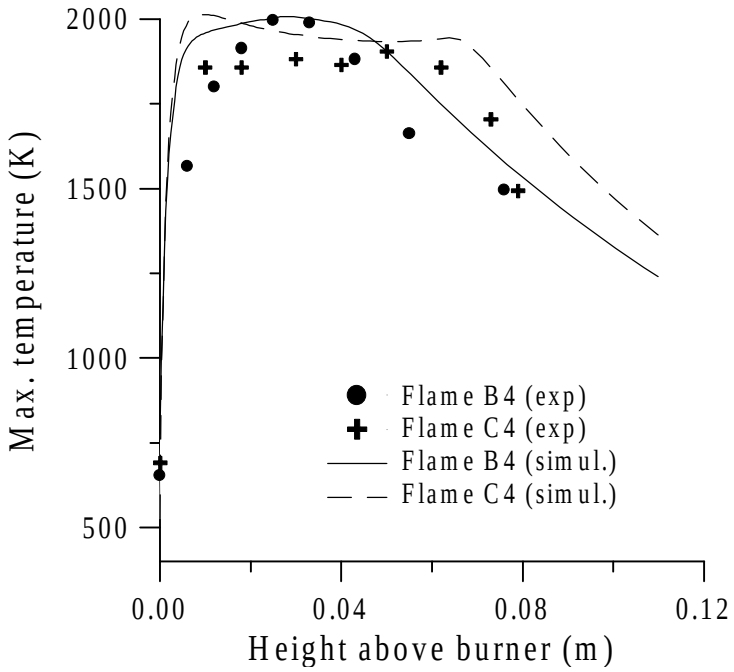

Figure 6 *Measurements of the maximum temperature as a function of height are compared with the corresponding results obtained from the simulations for flames B4 and C4. The plateau at high temperature for flame C4 is reproduced in the simulations. The curve for flame B4 has a single peak. Operating conditions are listed in table 5.1.*

6.5.3 Radial dispersion of the PM-component in the diffusion flames

The transport of particulate matter is simulated by the PM-component [cf. section 6.3] and the interesting issue is the radial transport of particles.

In figure 6.7, the mass fraction of the PM component in the flames is illustrated as contour plots for flame B3 and C3. The corresponding temperature plots are also shown. The PM-plots show a significant radial dispersion of particulate matter. The dispersion can be compared with the streak-lines passing through different radial positions in the jet ranging from the centerline to the wall of the jet. These lines are shown in figure 6.7. Streak-lines are continuous lines following a fluid element, which moves with the mean velocity of the gas.

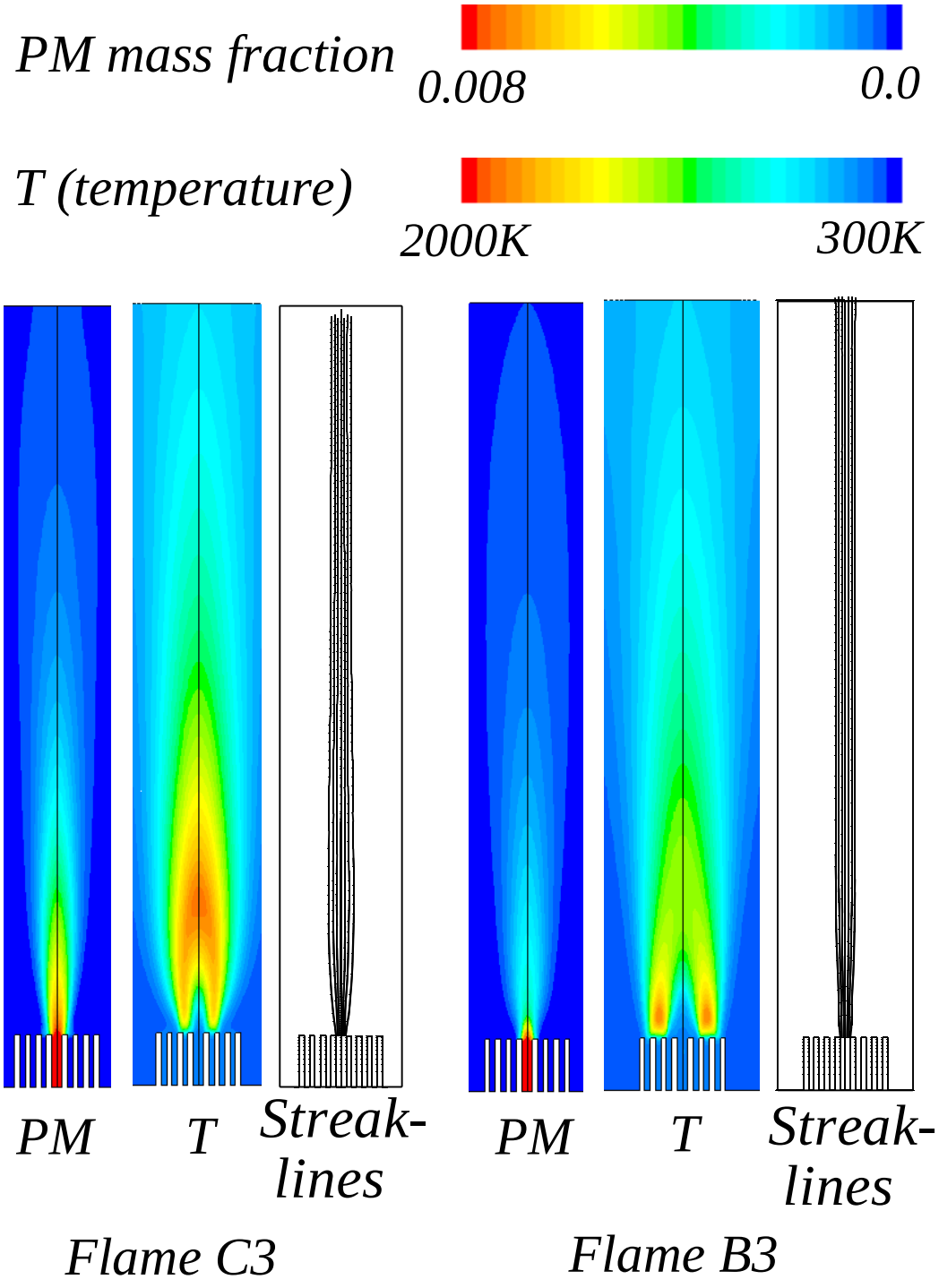

Figure 6 *For flames C3 and B3, the dispersion of the PM component is shown as contour plots and the corresponding temperature contours are shown. The radial dispersion of PM can be compared with the streak-lines originating from the precursor jet. Without radial dispersion, a particle follows a streak-line. The streak-lines lie close to the centre axis, whereas the contour plots of the PM component show a significant radial dispersion caused by turbulent diffusion.*

By comparing the streak-lines and the PM contours, one sees that the radial eddy dispersion transports PM far beyond the width of the streak-lines.

The radial dispersion of particles brings different particle trajectories into regions with widely different temperatures, which can cause a significant variation of particle properties.

Figure 6.8 shows a single flame case, B3, where the contours of the PM mass fraction are superimposed on the temperature pattern of the flame. Close to the burner mouth, we can see PM contours reaching the hot reaction zone but most of the particle mass, however, is found close to the jet axis in the lower temperature region. On this figure, the outermost contour corresponds to a dilution by a factor of 80 (0.008/0.0001). Higher above the flame, the particulate matter is quite evenly distributed in the gas.

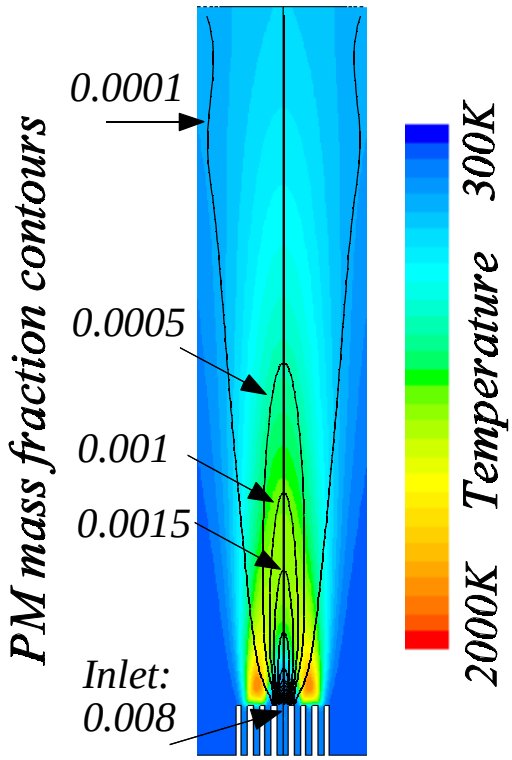

Figure 6 *For flame B3, the PM mass fraction contours are superimposed on the temperature contour plot to illustrate the effect of dispersion on the variation of the temperatures that particles will experience in some flames*

Based on this important figure, we cannot expect all particles in a flame to experience the same temperature histories through the flame zone. For flame B3, which is very heterogeneous in

structure compared with the single diffusion flame C3 on figure 6.7, we must expect the dispersion to have more effect on the particle properties than for flame C3. In the single diffusion flame, even highly dispersed particles will pass through a more homogeneous flame zone.

6.6 CFD results: Premixed burner

The results of the premixed burner simulations are presented as the diffusion flame results. The simulations are compared with experimental data and selected contour plots which characterizes the premixed burner are shown.

In order to avoid numerical problems, the reaction parameters used for the diffusion flame simulations have to be modified. The reaction rate of the premixed fuel and air has a very high local value just above the flame arrestor. This is very difficult to resolve with a computational grid without having a very fine grid just above the burner mouth. The problem is solved by changing the Arrhenius parameters and deactivating the eddy-breakup reaction model. When the Arrhenius values are changed to $A_{single} = 1 \cdot 10^{8} \mathrm{m}^3/\mathrm{mole/s}$ and $E_{single} = 40\ \mathrm{kJ/mole}$ [cf. equation 6.16], the results is a numerically stable flame with a flat reaction zone similar to the real system. For a premixed flat flame, the most important parameter is the adiabatic flame temperature. This temperature is not affected by the change of parameters as long as the reaction is sufficiently fast. The transport phenomena, which controls the diffusion flame, are less important in the premixed flame system.

All wall boundaries in the computational grid are similar to the real system. The transport of heat from the experimental system takes place either by convection at the outlet, by radiation, by heat transport to the cold surface of the quenching metal ring or by conduction of heat through the quartz wall to the surrounding gas. All these features are accounted for in the simulations.

6.6.1 Temperature contour plots

The effect of operating conditions on the behaviour of the premixed burner is illustrated on figure 6.9, which shows the temperature contours for the four experimental conditions listed in table 5.2. On these plots, the quenching ring appears blank. This is due to the fact, that the ring itself is not a part of the computational domain, only the wall effects of the ring, thereby also the quenching inlet, are included. This does not introduce errors. It merely saves computational time by reducing the total number of computational cells.

The effect of the quenching is the most obvious phenomenon on the plots. From P1 to P2 and

from P3 to P4 the quenching has a drastic effect on the temperature pattern. The flow patterns of the jets are disturbed by large eddies, which are created in the quenching zone. However, the high jet velocity in P1 and P2 stabilises the flame structure slightly. By comparing P1 and P3 we

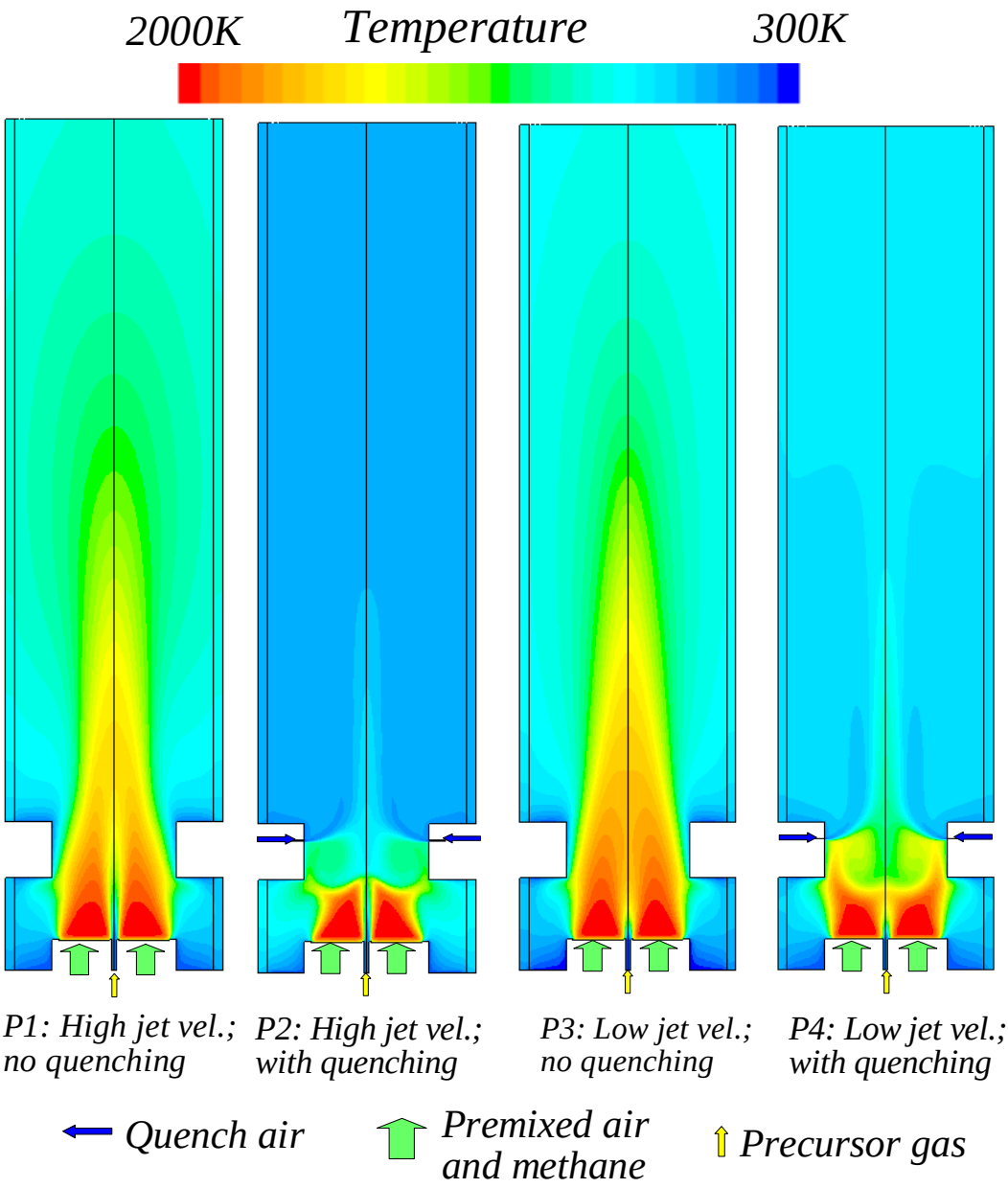

Figure 6 *Temperature contour plots of the four experimental conditions of the premixed burner [cf. table 5.2]. The quenching has a drastic effect on the temperature pattern. Large eddies are created in the quenching zone which disturbs the jet flow below the quenching point. However, the high jet velocity in P1 and P2 stabilises the flame structure slightly. The quenching ring appears blank on the plots, which is because the ring itself is not a part of the computational domain, only the wall effects of the ring, thereby also the quenching inlet, are included.*

see that the high jet velocity creates a more well-mixed zone in the upper part of the flame. Also, the cold jet extends higher up into the flame zone for P1 than for P3.

6.6.2 Temperature profiles

The jet axis temperature profiles from the simulations are compared with the experimental data reported in section 5.2.1 [cf. figure 6.10]. There is an excellent agreement between the simulations and the experimental data all the way to the exit.

The corresponding graph for the two cases with quenching is shown on figure 6.11

The location of the sharp temperature drop is accurately predicted by the simulations. Because of the large eddies formed in the quenching zone, the temperature drop occurs below the actual quenching height, which is 3 centimetres.

The temperature-rise above the quenching ring, which is seen in the experimental data, is caused by the mixing between the cooler quenched gases and the hot gases, which pass in between the five quenching jets. This cannot be predicted by the simulations, since the quenching device in

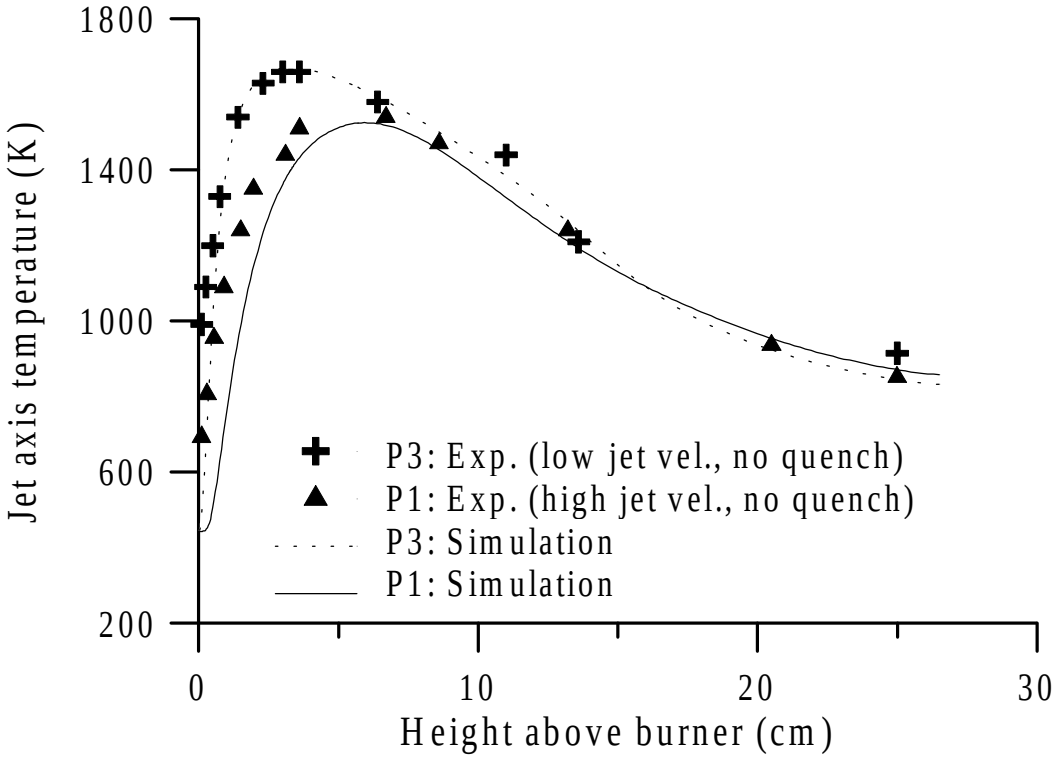

Figure 6 *Simulated and experimental axial temperature profiles are compared for the two premixed flames with no quenching. The agreement is excellent and we see a lower maximum temperature with the peak located higher above the burner for the case with high jet velocity.*

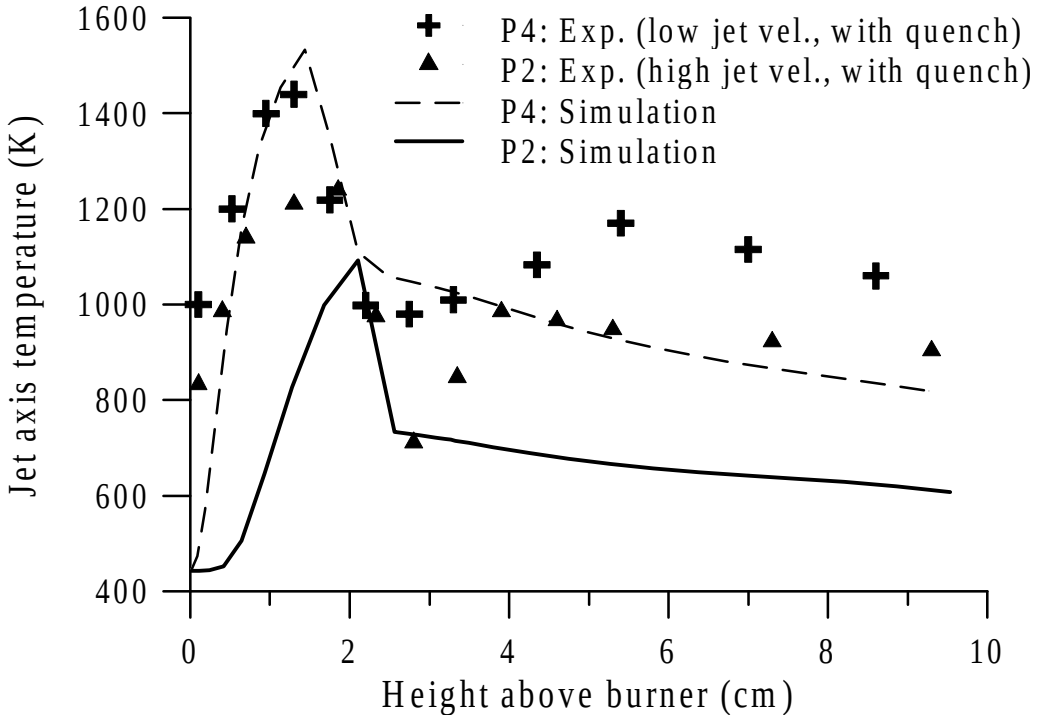

Figure 6 *Simulated and experimental axial temperature profiles are compared for the two premixed flames with quenching. In both cases, the steep temperature drop is well reproduced by the simulations. The under prediction of the temperature above the quenching ring is caused by the approximation of the quenching ring as rotationally symmetric slit in the computational domain.*

the computational domain is approximated as a rotationally symmetric slit [cf. figure 6.1]. It can seem impossible, that a fraction of the hot combustion products in the real system can pass between the quenching jets. However, this is the case. A schematic of this is shown in the top view of the quenching ring [cf. figure 6.12], where the regions of hot upcoming gases are shown. The temperature measured along the dotted circle is low close to or inside the quenching jets whereas the temperature is high in the undisturbed regions of hot upcoming gases. A schematic of the temperature profile along the dotted circle in the ring is shown. The efficiency of the quenching device is not in question since all five jets, as shown on the temperature curves, rapidly cool the jet core. This figure only serves to illustrate the effect on the simulation results caused by assuming rotational symmetry. The minor temperature rise above the quenching ring cannot be captured by the simulations because of this.

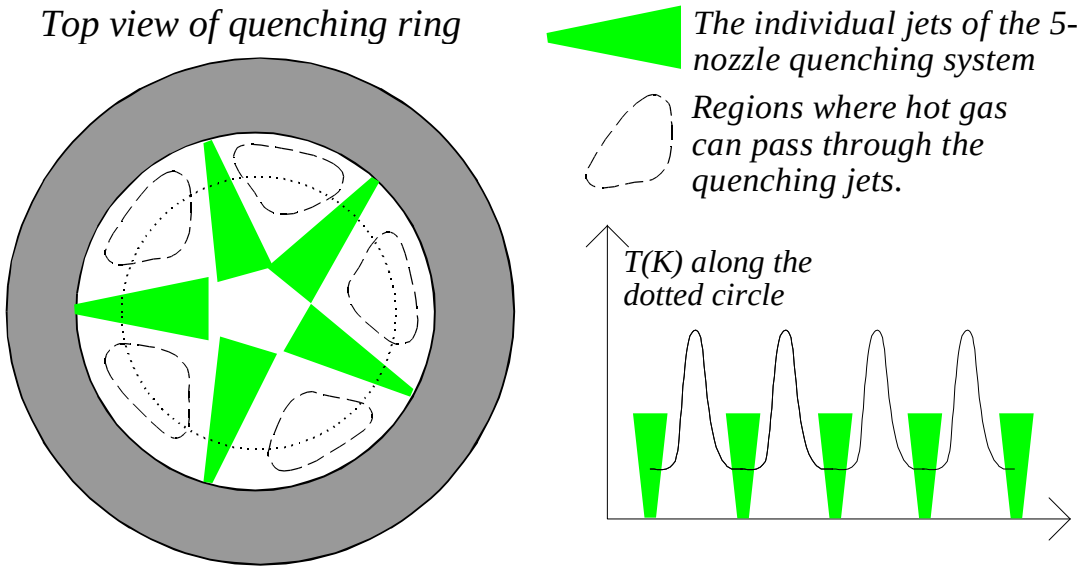

Figure 6 *A schematic of the top view of the quenching ring, which shows the regions away from the centre line where hot upcoming gases can pass through the quenching zone. This behaviour is not captured by the simulations.*

In conclusion, the flow and temperature fields of the premixed burner system are well predicted using a modified Arrhenius expression thereby avoiding numerical problems. The assumption of rotational symmetry creates minor deviations above the quenching ring when the quenching is on. This disadvantage is by far gained in terms of the computational time saved by avoiding a rigorous 3D simulation. In addition, the heat transport from the system to the surroundings is described accurately by the boundary conditions since the cooling rate up through the system for P1 and P3 was well predicted.

6.6.3 Radial dispersion of the PM-component

The radial dispersion of the PM component in the premixed burner system is illustrated on figure 6.13. Because of the low variation of the concentration in the upper half of the system, only the lower half is shown on these plots. Mass fraction contour plots are shown for configurations P1 and P2 [cf. table 5.2]. The same picture is qualitatively seen for P3 and P4. For both cases shown here, we see a significant radial dispersion of the PM component throughout the flame region. For the case with quenching, P2, the gas flow is forced away from the centerline and the net flow of particle mass follow lines similar to the streak-lines shown below the PM-plot. Still, the

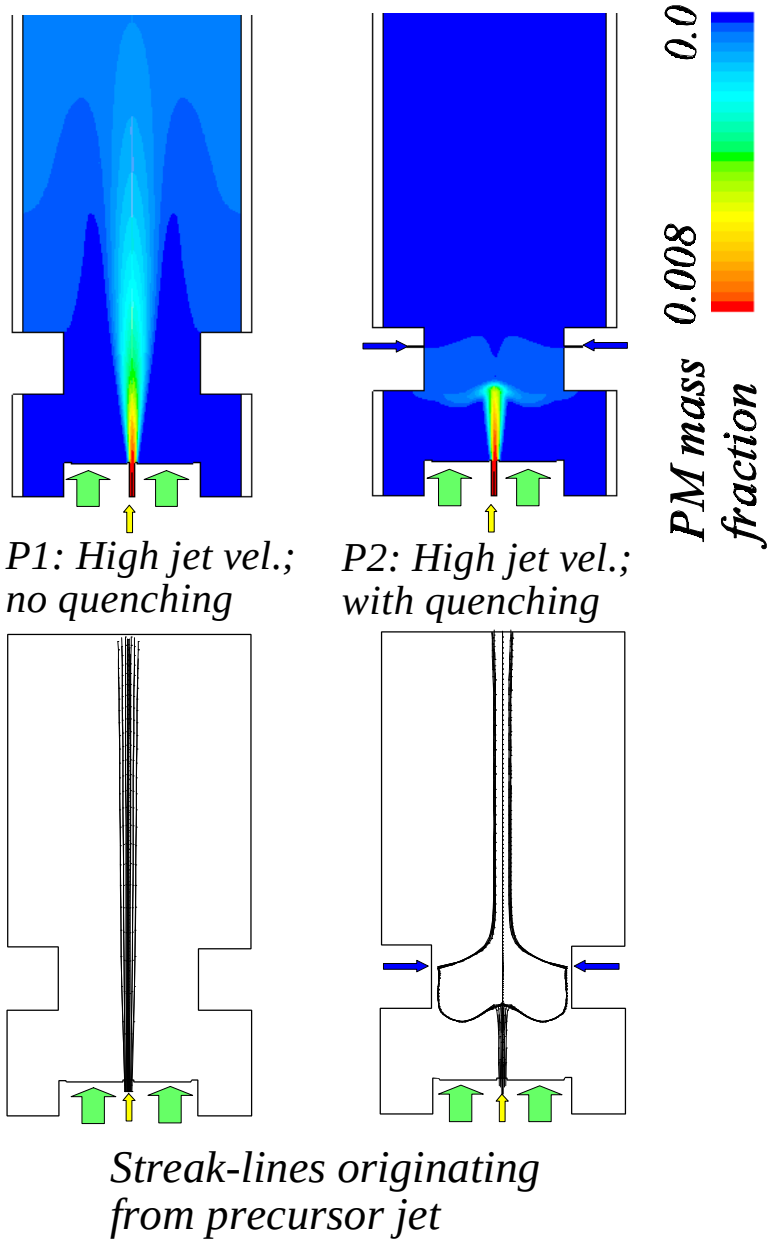

Figure 6 *The mass fraction contour plots for cases P1 and P2 show a significant radial dispersion of the PM component. This is enhanced by the quenching for P2, which causes the net gas flow away from the centre axis in large eddies. The same is qualitatively seen for P3 and P4. The corresponding streak-lines originating in the jet are shown below the mass fraction plots. The streak-lines differ significantly from the flow of dispersed particulate matter.*

streak-lines after the quenching zone are reunited close to the centre axis. The PM-component, however, is completely mixed with the gases and the mass concentration after the mixing is so low that it does not show on the colour scale.

For P1, one can also see a significant dispersion of PM compared with the width of the streak-lines.

The high lateral dispersion can be compared with the concentration measurements for different radial outlet positions [cf. section 5.2.5]. The total aggregate concentration across the outlet is virtually uniform in those measurements. These measurements confirm the results of the simulations where PM component at the outlet is highly dispersed. Therefore, simulating the particle transport by means of the PM component is an expedient method for particle/aggregate transport in systems with turbulence.

7 Simulation of flame generated particles: Combining aerosol dynamics with CFD

In this chapter, a novel method for combining aerosol dynamics with CFD simulations is presented. The model for the aerosol dynamics combines the kinetics of coagulation and coalescence with dilution effects caused by turbulent radial dispersion of particles. The computed flow and temperature fields in the flames form the basis for calculation of trajectories, where particles originating from different radial positions in the precursor jet will experience different time-temperature histories.

7.1 A monodisperse coagulation/coalescence model with dilution

In a normal flame process, the concentration of particles/agglomerates decreases along the particle trajectories because of coagulation. However, for a non-coagulating aerosol, the concentration still decreases because of dilution of the precursor jet with the other gasses. This dilution is taken into account by using the CFD-simulations in which the gas component, "PM", simulates the transport of particulate matter. In both burners, the precursor flows in the central tube. The PM component described in section 6.2 does not take part in any reaction and can therefore be used to calculate dilution. The PM mass fraction at a certain position compared with the value at the jet outlet corresponds to the degree of mixing with the other gas streams.
For the regular monodisperse model (Kruis et al., 1993) which was described in chapter 3, the decrease in number concentration of agglomerates is given by:

$$\frac{dN}{dt} = -\frac{1}{2}\beta N^2 \qquad \textbf{(7)}$$

where N is the number concentration and β is the collision frequency function [cf. chapter 3.2]. To model the dilution, one can use a variable volume batch reactor model, where the batch reactor in time corresponds to a point following a particle in space. The volume of the batch reactor increases with time according to the dilution ratio. The particle balance becomes:

$$V(t+\Delta t)N(t+\Delta t) - V(t)N(t) = -V(t)\frac{\beta}{2}N(t)^2\Delta t \qquad \textbf{(7)}$$

where *V(t)* is the variable volume. The connection between *V* and the dilution factor, f_D, is:

$$f_D(t) = \frac{V_0}{V(t)} = \frac{y_{PM}}{y_{PM,0}} \quad \textbf{(7)}$$

where V_0 is an initial volume. The dilution factor can also be expressed as the ratio of the mass fraction of particles in the gas and at the inlet. Since f_D is less than or equal to one, *V* will always be greater than or equal to V_0.

For $\Delta t \to 0$, equation 7.2 can be reduced to:

$$\frac{d(VN)}{dt} = -V\frac{\beta}{2}N^2 \quad \textbf{(7)}$$

Expanding the differential and rearranging yields:

$$\frac{dN}{dt} = -\frac{\beta}{2}N^2 - \frac{N}{V}\frac{dV}{dt} \quad \textbf{(7)}$$

Using equation 7.5 with 7.3 gives:

$$\frac{dN}{dt} = -\frac{\beta}{2}N^2 + \frac{N}{f_D}\frac{df_D}{dt} \quad \textbf{(7)}$$

This equation describes coagulation and dilution, where f_D at the precursor inlet is equal to one and is less than one upstream from the inlet. The value of f_D and df_D/dt can be calculated from the simulated concentration field of PM.

By changing the concentration, *N*, to one based on number per mass of gas, N_{mass}, the equation is transformed to:

$$\frac{dN_{mass}}{dt} = -\frac{1}{2}\beta\rho_g N_{mass}^2 + \frac{N_{mass}}{f_D}\frac{df_D}{dt} \quad \textbf{(7)}$$

where ρ_g is the gas density. With the concentration based on mass and not volume, the model automatically is suited for non-isothermal conditions.

The equations for aggregate surface area and aggregate volume in the mono-disperse model must be slightly modified. The change in aggregate properties must not be affected by pure dilution when coagulation can be neglected. Therefore, the differential equations describing surface area and volume of the aggregates are modified as shown below:

$$\frac{da}{dt} = -\frac{1}{N_{mass}}\left(-\frac{1}{2}\beta\rho_g N_{mass}^{\,2}\right)a - \frac{1}{\tau_f(d_p)}\left(a - a_s\right) \qquad \textbf{(7)}$$

$$\frac{dv}{dt} = -\frac{1}{N_{mass}}\left(-\frac{1}{2}\beta\rho_g N_{mass}^{\,2}\right)v \qquad \textbf{(7)}$$

Equation 7.7 to 7.9 forms a consistent set of differential equations for the aerosol dynamics with radial dispersion of particles. They are in a form, which allows a direct integration along particle trajectories. However, the coalescence term of equation 7.8, $(a\text{-}a_s)/\tau_f$, must be modified to a more accurate approach to the coalescence of large aggregates, which is the subject for the following section.

7.2 A new approach to coalescence of aggregates: The Points-Of-Contact model

For the coalescence of aggregates, Lehtinen et al. (1996) proposed an expression for the reduction of surface area, a, based on coalescence by volume diffusion of groups of m_p particles. This expression has already been presented in chapter 3.

In a novel approach, the so-called Points-Of-Contact (POC) model developed in the present study, the starting point is the regular coalescence expression for two initially spherical particles with total volume v, as proposed by Friedlander and Wu (1994) [cf. equation 3.10]:

$$\frac{da}{dt} = -\frac{1}{\tau_f(v)}\left(a - a_s\right) \qquad \textbf{(7)}$$

Instead of expanding this model to hold for a certain number of particles, we use the fact that the coalescence mainly takes place at the contact point between adjacent particles.

In the monodisperse model, the aggregates are described by the surface area, a, and volume, v, and aggregates are at all times assumed to consist of n_p equally sized primary particles with diameter, d_p . The characteristics of the aggregates are given by:

$$d_p = \frac{6v}{a} \quad , \quad v_p = \frac{\pi}{6} d_p^3 \quad , \quad n_p = \frac{v}{v_p} \quad , \quad a_p = \pi d_p^2 \qquad \textbf{(7)}$$

where v_p and a_p are the volume and surface area respectively of a primary particle.
Therefore, if the local sintering rate in an aggregate is determined at each contact point between two adjacent particles, then at each contact point the local rate of reduction of the surface area is given by the normal expression for da/dt based on the size d_p.

In an aggregate without cyclic structures, the number of contact points is equal to n_p-1, and in the following, we assume that the number of contact points caused by cyclic structures is negligible. Significant number of cyclic structures will probably only be present in large aggregates, where the number of contact points is already very large.

Therefore, the total rate of reduction of surface area in an aggregate is given by the following

equations:

$$\frac{da}{dt} = \frac{-1}{\tau_f(d_p^*)}(a - a_s) \quad and \quad d_p^* = \left(\frac{6(v/2)}{\pi}\right)^{1/3} \qquad , for\ n_p \le 2 \qquad \textbf{(7)}$$

$$\frac{da}{dt} = (n_p - 1)\left[\frac{-1}{\tau_f(d_p)}\left(2a_p - a_{2\cdot p,s}\right)\right] \qquad , for\ n_p > 2 \qquad \textbf{(7)}$$

where $\tau_f(d_p)$ could be taken from literature data or table 3.1 with equation 3.18. The parameter $a_{2\,p,s}$ is the surface area of a spherical particle with the same solid volume as two spherical primary particles with diameters d_p. Furthermore, d_p^* is the size of the primary particle when the aggregate volume is partitioned into two primary particles. This corresponds to the value of d_p computed for $n_p = 2$. In general, $a_{n\cdot p,\,s}$ can be calculated by:

$$a_{n\cdot p,s} = \pi n^{2/3} d_p^2 = n^{2/3} a_p \qquad \textbf{(7)}$$

In equation 7.12, the calculation of τ_f is based on a fixed particle size, d_p^*, which is the particle size when the coalescence is at the state where two spherical particles remain in the aggregate, each containing half the solid volume, *v/2*. Until the next collision, the coalescence is essentially based on the exponential decay of coalescence of two particles expressed by equation 7.10, and it seems reasonable that the final exponential decay is calculated from the last identifiable spherical particle.

In the formulation of the POC-model, the coalescence of an aggregate is completely described by the expression for the coalescence of two primary particles and the number of contact points in the aggregate. There are no restrictions on the mathematical form of the expression for the characteristic coalescence time. The POC-model also has the right asymptotic behaviour. Once the surface area is reduced to a level where the corresponding number of primary particles is two, the normal coalescence model holds for the final stage of coalescence. For n_p=2, the change from eq. 7.12 to 7.13 is continuous since n_p-1=1 for n_p=2 and the value of *a* for n_p=2 is $2a_p$. The physical aspect of the POC model is illustrated on figure 7.1.

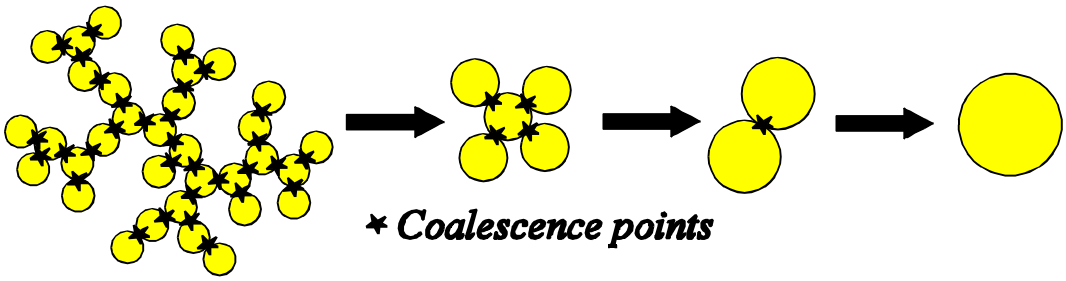

Figure 7 *A schematic of The POC-model (Points-of-Contact) approach to coalescence of aggregates. The local coalescence rate is only a function of primary particle size. The overall coalescence rate is obtained by multiplying the local rate by the number of connecting points.*

In the following graph, we compare four different coalescence expressions for an aggregate consisting of n_p particles by plotting *da/dt* for various values of n_p. The comparisons are based on the solid state diffusion mechanism, which is the foundation for the derivation of the group model (Lehtinen et al., 1996).

The four models compared in figure 7.2 are:

- Friedlander and Wu (1994): τ_f is based on the total aggregate volume and the driving force is the difference between the total surface area and the surface area of the corresponding solid sphere, i.e. (a-a_s).
- Kruis et al. (1993): τ_f is based on the primary particle size and the driving force is the difference between the total surface area and the surface area of the corresponding solid sphere, i.e. (a-a_s).
- Lehtinen et al. (1996): τ_f is based on the number of particles pr. group, m_p, and the driving force is the difference in current and relaxed surface area for the group (a_{mp} - $a_{mp,\,s}$). In figure 7.2, the value of m is 3. The value for dendritic aggregates is close to 3 or 4 (Lehtinen et al, 1996). The rate is higher for m_p = 3 than m_p = 4.
- The POC-model: τ_f is based on the primary particle size, the driving force is the local driving force between two particles and the rate is proportional to the number of particle contact points in the

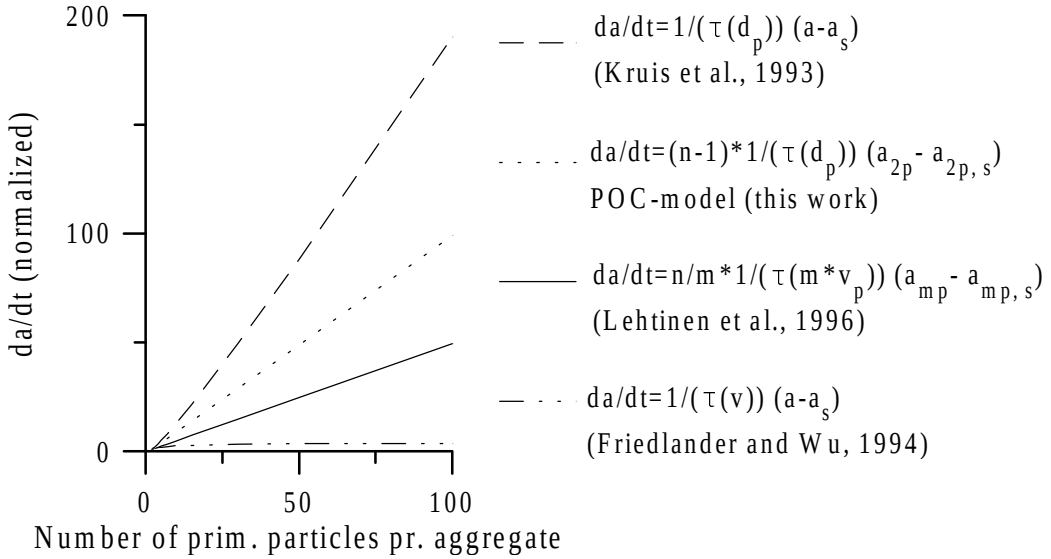

Figure 7 *The effect of number of primary particles pr. aggregate on the rate of change of surface area for four different coalescence models. For the group coalescence model (Lehtinen et al., 1996), the group size, m, is 3. The rate predicted by the POC-model lies between the group model and the simple expression from Kruis et al. (1993).*

aggregate, n_p-1.

In the two simple approaches (Friedlander and Wu, 1994 and Kruis et al., 1993) the rate is underestimated and overestimated respectively. In the first case because τ_f is calculated based on the total aggregate volume. The approach by Kruis et al.(1995) overestimates the rate because τ_f is based on the "local" primary particle size but the driving force is the difference between the total area and the corresponding area of a single sphere.

For two reasons, the POC-model predicts a rate slightly higher than the group model by Lehtinen et al. (1996):

1. The value of τ_f is in the POC model based on d_p, not $m_p v_p$
2. The group model neglects the sintering at contact points between the individual groups.

Finally, all models do, for n_p approaching 2, have the same sintering rate, which is the final step of coalescence from two particles to one. This is not influenced by aggregate issues.

7.3 Summary of the equations for the modified monodisperse model

In order to get a clear overview of the modified monodisperse model before we discuss the connection with CFD-simulations, the elements of the model are summarized below.

The decay of concentration of particles/aggregates pr. mass of gas is given by:

$$\frac{dN_{mass}}{dt} = -\frac{1}{2}\beta\rho_g N_{mass}^2 + \frac{N_{mass}}{f_D}\frac{df_D}{dt} \qquad \textbf{(7)}$$

where f_D is a dilution factor and β is the collision frequency function [cf. Chapter 3.2] based on the particle/aggregate collision diameter, which is related to the fractal dimension, D_f [cf. equation 3.7]. The change of aggregate surface area is

$$\frac{da}{dt} = -\frac{1}{N_{mass}}\left(-\frac{1}{2}\beta\rho_g N_{mass}^2\right) a + \left[\frac{da}{dt}\right]_{coalesce} \qquad \textbf{(7)}$$

where the coalescence rate is calculated according to the POC-model:

$$\left[\frac{da}{dt}\right]_{coalesce} = (n_p - 1)\left[\frac{-1}{\tau_f(d_p)}\left(2a_p - a_{2\cdot p,s}\right)\right] \quad , \text{for } n_p > 2 \qquad \textbf{(7)}$$

$$\left[\frac{da}{dt}\right]_{coalesce} = \frac{-1}{\tau_f(d_p^*)}\left(a - a_s\right) \quad \text{and } d_p^* = \left(\frac{6(v/2)}{\pi}\right)^{1/3} \quad , \text{for } n_p \le 2 \qquad \textbf{(7)}$$

The individual parameters of this model are explained on page 89.
The particle/aggregate volume increases according to:

$$\frac{dv}{dt} = -\frac{1}{N_{mass}}\left(-\frac{1}{2}\beta\rho_g N_{mass}^2\right) v \qquad \textbf{(7)}$$

Regarding the coalescence time, I choose to work with an empirical expression for the characteristic coalescence time:

$$\tau_f = A d_p^{\,m} T \exp\left(\frac{E_A}{RT}\right) \qquad \textbf{(7)}$$

In this expression, A is a pre-exponential factor, d_p is the particle diameter, T is the temperature and E_A is the activation energy for the coalescence process. It is obvious, that this expression is suited for fitting, since it contains two "unknown" parameters, A and E_A. The value of m is determined by the coalescence mechanism.

In the presented form, A and E_A are highly coupled, which leads to large confidence intervals when this expression is fitted to experimental data. The sintering rate at a certain temperature, T_0, can be obtained by an infinite number of combinations of A and E_A. We can rewrite the expression to the following form:

$$\tau_f = k_0 d_p^{\,m} \frac{T}{T_0} \exp\left(\frac{E_A}{R}\left(\frac{1}{T} - \frac{1}{T_0}\right)\right) \qquad \textbf{(7)}$$

which mathematically is identical with eq. 7.20. The pre-exponential term, $k_0 \cdot d_p^{\,m}$, is now the characteristic coalescence time at the temperature T_0. The two expressions are identical when $k_0 \cdot d_p^{\,m}$ is equal to the value of τ_f from eq. 7.20 evaluated at T_0. The actual value of T_0 is without influence on the results and the value of T_0 is typically chosen to be somewhere in the temperature interval of interest. In the following, all simulations are carried out with T_0=1400K.

As already discussed in chapter 3.5.4, surface diffusion is the most likely coalescence mechanism for nano particles. The empirical coalescence time for surface diffusion is obtained when the value of m is four and when nothing else is stated, m is assumed equal to four.

7.4 Calculation of particle trajectories in a gas with radial dispersion

Particles are dispersed mainly by turbulent diffusion and will therefore not follow the mean flow of gases. A method for calculating time, temperature and particle mass dilution along particle trajectories is presented. The CFD simulations provide the necessary information about flow, mass fractions, reaction and temperature.

Figure 7.3 shows a typical contour plot of the dispersion of particle mass upstream from the burner mouth, where red and dark blue corresponds to a high and low mass fraction of PM respectively. The diameter of the jet-tube is 2mm.

The net axial particle mass flow rate, w_{PM} (kg/s), which is constant up through the flame, is calculated at the inlet by:

$$w_{PM} = 2\pi \int_0^{r_{tube}} \rho_g \, y_{PM,inlet} \, u_z \, r \, dr \qquad (7)$$

where r_{tube} is the radius of the precursor tube, ρ_g is the gas density, y_{PM} is the mass fraction of the PM (the CFD-equivalent of particulate matter)and u_z is the linear gas velocity component in the vertical z-direction.

At any height, z, above the burner, a corresponding integration for $r = [0; r_{max}]$ yields the same value of the mass flow rate. However, the radius of the circular cross section, within which the total mass flow is "contained", increases with z because of the dispersion.

By radial integration one can calculate the fraction of the particle mass flowing inside a circle with certain radial distance from the symmetry axis. If a constant fraction of the total particle mass flow is specified, we by that define an envelope-curve, (z,r), within which a given fraction of the total particle mass flows. The envelopes thus defined are an obvious choice as particle trajectories. Due to the random nature of turbulent diffusion, they are not true trajectories in the sense that they depict the path of all individual particles. However, a point on a trajectory represents the most likely position for a particle previously located at that trajectory.

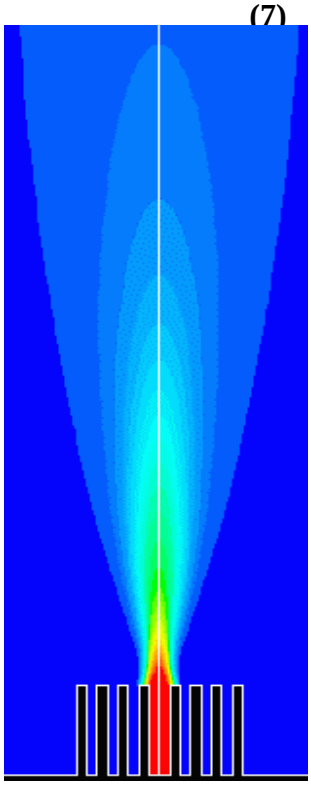

Figure 7 *An example of a contour plot of particle mass fraction upstream from the diffusion burner (red~0.008 and blue~* 0).

For a given value of z, we calculate values of r_i for which the following equation is fulfilled:

$$2\pi \int_0^{r_i} \rho_g \, y_{PM} \, u_z \, r \, dr = w_{PM} \alpha_i \ , \ i=1,2,...,N_{line} \qquad \textbf{(7)}$$

where N_{line} is the number of trajectories and r_i are the radial values, inside which the corresponding fraction of particle mass flows. The parameter α_i is the fraction of PM mass flow contained within the i^{th} trajectory. The values of α_i can in general be assigned any value between zero and one. Yet, in order to get a reasonable representation of the total mass flow of particulate matter, the α-values can be computed by the following equation, which evenly distributes the N_{line} trajectories:

$$\alpha_i = \frac{1}{2N_{line}} + \frac{i-1}{N_{line}} \ , \ i=1,2,...,N_{line} \qquad \textbf{(7)}$$

For the case of five trajectories, N_{line}=5, the corresponding α-values are 0.1, 0.3, 0.5, 0.7 and 0.9 respectively. Each of the five trajectories defined by 7.23 and 7.24 represents thus the history of 20%, equal to $1/N_{line}$, of the total particle flow.

The independent variable in the particle dynamics equations is time. Therefore, the position, z, along a trajectory has to be transformed into time. The resolution of the trajectories in the vertical z-direction is determined by the discrete number of points, N_Z, where equation 7.23 is evaluated. The axial spacing, Δz, between the individual points on the (z,r)-curves is given by:

$$\Delta z = \frac{z_{max} - z_0}{N_z - 1} \qquad \textbf{(7)}$$

where z_{max}-z_0 is actual height of the computational domain concerned.

For each discrete value of z_j (where j=1,...,N_Z) the values of r_i are computed. The calculation of time is carried out by the following approximation: The time of flight from z_j to z_{j+1} for the i^{th} trajectory is calculated as:

$$\Delta t_i \approx \frac{\Delta z}{v_z(z_j, r_i)} \qquad \textbf{(7)}$$

For dr_i / dz equal to zero, which would correspond to no radial dissipation, equation (7.26) is exact. In these systems with dispersion, the approximation is still valid since $\Delta t_i v_z \gg \Delta t_i v_r$.

For each point on the curves given by z_j and r_i , the temperature and the dilution factor are

calculated and the results are N_{line} particle trajectories where the relation between time, temperature and dilution ratio is established. A fraction of the particle mass flow equal to $1/N_{line}$ is then "assigned" the time-temperature history of each trajectory.

At any point, the dilution factor, f_D, is computed as the value of y_{PM} at the current position divided by the value at the inlet, $y_{PM,\,inlet}$.

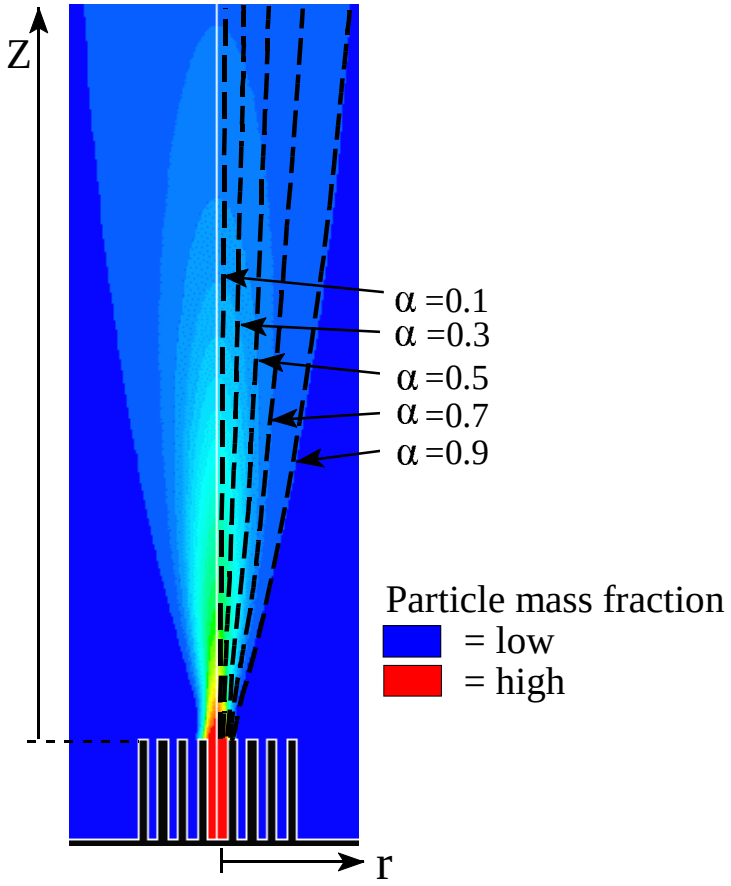

Figure 7 *Visualization of characteristic trajectories describing the radial distribution of particulate matter. In this case, five trajectories are shown and each trajectory represents the time/temperature/dilution history of 1/5 of the total particle mass flow*

The concept of discrete trajectories in dispersion systems is illustrated on figure 7.4, where the spread of particulate matter is calculated as five characteristic trajectories with separate time/temperature/dilution-history.

The particle model is integrated along each trajectory, and the average outlet property of the process can be computed as the sum of values from each trajectory divided by the total number

of trajectories, N_{line}. For the specific surface area, the average outlet value, $\overline{SSA}$ is computed by

$$\overline{SSA} = \frac{1}{N_{line}} \sum_{i=1}^{N_{line}} SSA_i \qquad \textbf{(7)}$$

7.4.1 Implementation of the trajectory calculation

The CFD simulations yield values of velocity, temperature, composition etc. in each cell.
Data from a simulation are stored in so-called universal files (Fluent Inc. ,1996) which are read by the fortran program. For any position in the computational domain, the value of any dependent variable can be calculated by interpolation between the values in the nearby cell centres. This interpolation is carried by a 2D-polynomial interpolation method. A description of the interpolation method is shown in Appendix B. The method only works for structured grids, where the position, e.g. (x,y), can be expressed by indices, e.g. *i* and *j*.
The numerical procedure in the fortran code for the calculation of trajectories is:

1. Read the CFD data file containing all computational data into large matrices.
2. Determine the total mass flow of the PM component, w_{PM}, at the inlet ($z = z_0$) by equation 7.22. The initial time for each trajectory is set at zero.
3. Compute the N_{line} different values of r_i according to equation 7.23 on page 95.
4. Calculate temperature and dilution ratio ($f_D = y_{PM} / y_{PM,inlet}$) for each value of r_i by interpolation and save current position, time and temperature.
5. Calculate the z-component of the velocity for each value of r_i by interpolation.
6. For Δz given by equation 7.25, the time change to the next point on the trajectory, Δt_i, is calculated by equation 7.26.
7. Repeat from step 3 as long z_j is less than z_{max}

The trajectory data are stored in large matrices/vectors, which are used with the particle model to calculate particle dynamics in the flame.
A complete fortran code, POC_CFD.FOR, for determination of trajectories and integration of the monodisperse POC-model along the N_{line} trajectories has been developed. The inputs for the program are data from the CFD simulation and the parameters for the particle dynamics.
The equation system is solved with a semi-implicit Runge-Kutta ordinary differential equation solver (Villadsen and Michelsen, 1978). Initial values of particle morphology, concentration, particle/aggregate surface area and volume are specified and the equations are integrated with time as the independent variable. The values of temperature and dilution ratio for a specific value

of time are computed from the trajectory data by linear interpolation between the two nearest discrete trajectory points. As an example, if $t_i < t < t_{i+1}$, then the values of T and f_D are determined by linear interpolation between (t_i ,T_i , $f_{D,\,i}$) and (t_{i+1} , T_{i+1} , $f_{D,\,i+1}$).

8 Results of particle dynamics simulations

The particle dynamics model presented in the previous chapter is solved for both the diffusion flame burner and the premixed burner. For one specific flame, diffusion flame B3, the detailed features of the model are investigated. The experimental data are used to estimate the coalescence parameters for alumina particles. Selected time-temperature relations along particle trajectories are presented and the resulting values of specific surface area/primary particle size are discussed. The new approach to particle simulation in flames is additionally validated by complete simulations of the measurements from Pratsinis et al. (1996) where a different diffusion flame burner is employed for the production of titania particles. All simulation data in this chapter are obtained from the implementation of the model, POC_CFD.FOR, which uses the CFD data to compute the particle trajectories along which the particle dynamics is solved. The Initial conditions for alumina and titania particles are listed in Appendix C.

8.1 Investigating the features of the model in the double diffusion flame

To illustrate the different aspects of the simulation method, the double diffusion flame B3, which was shown on figures 6.4, 6.7 and 6.8, is selected for illustration purposes. This flame has a very heterogeneous structure and therefore the effect of dispersion is significant. This is studied by carrying out simulations for two chosen parameter-sets for the characteristic coalescence time [cf. equation 7.21]:

- High coalescence activation energy: E_A=300 kJ/mole with k_0=5·10^{29} m^{-4}s ; m=4
- Low coalescence activation energy: E_A=50 kJ/mole with k_0=1·10^{29} m^{-4}s ; m=4

In both cases, the dependence of the primary particle size, the power m, is chosen to be 4, which corresponds to surface diffusion. The value of T_0 is 1400K. In all simulations, the value of the fractal dimension is 1.8 [cf. Section 3.3, page 7].

The number of trajectories in the following simulations is five, i.e. the dispersion of particulate matter is approximated by five characteristic trajectories, each accounting for the history of 20% of the particle mass flow. The outermost trajectory [see figure 7.4] represents the highly dispersed particles, which corresponds to α=0.9. In the figures 8.1 to 8.4, the outermost trajectory is marked with a "★".

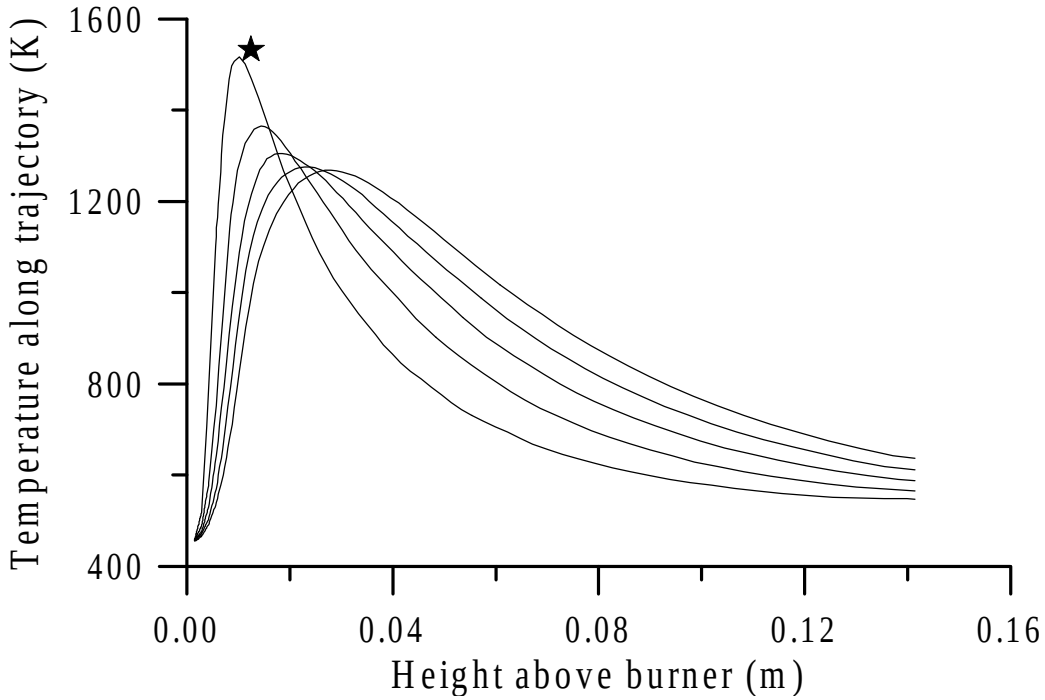

Figure 8 *The temperature as a function of height along the five particle trajectories for flame B3. The trajectory corresponding to the most dispersed particles is marked with a "⋆"..*

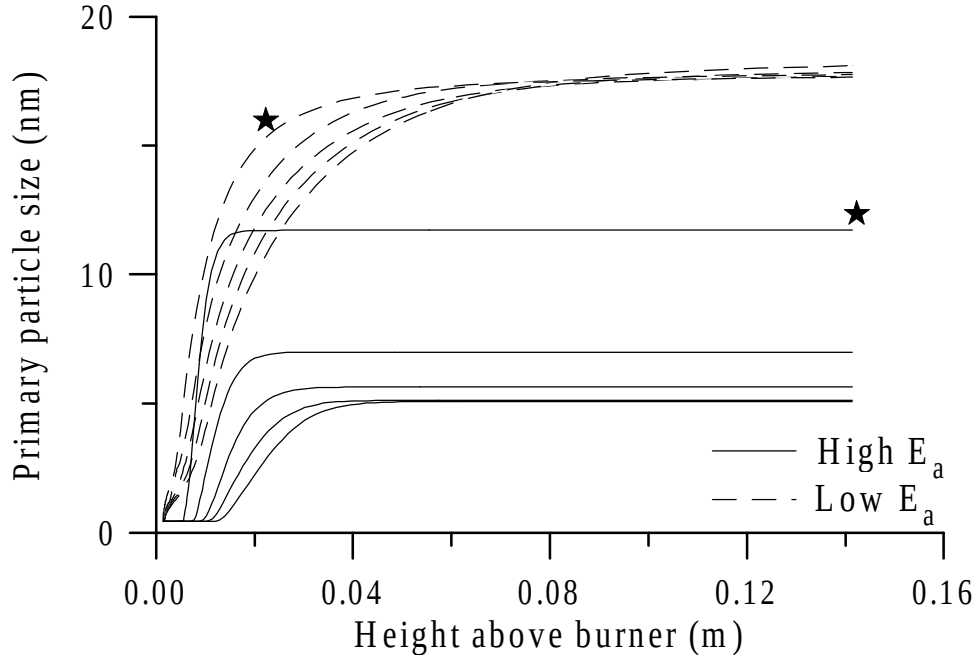

Figure 8 *For the two different activation energy levels, the primary particle size is shown as a function of height along the five particle trajectories for flame B3. The trajectory corresponding to the most dispersed particles is marked with a "⋆". The temperature curves are shown on figure 8.1.*

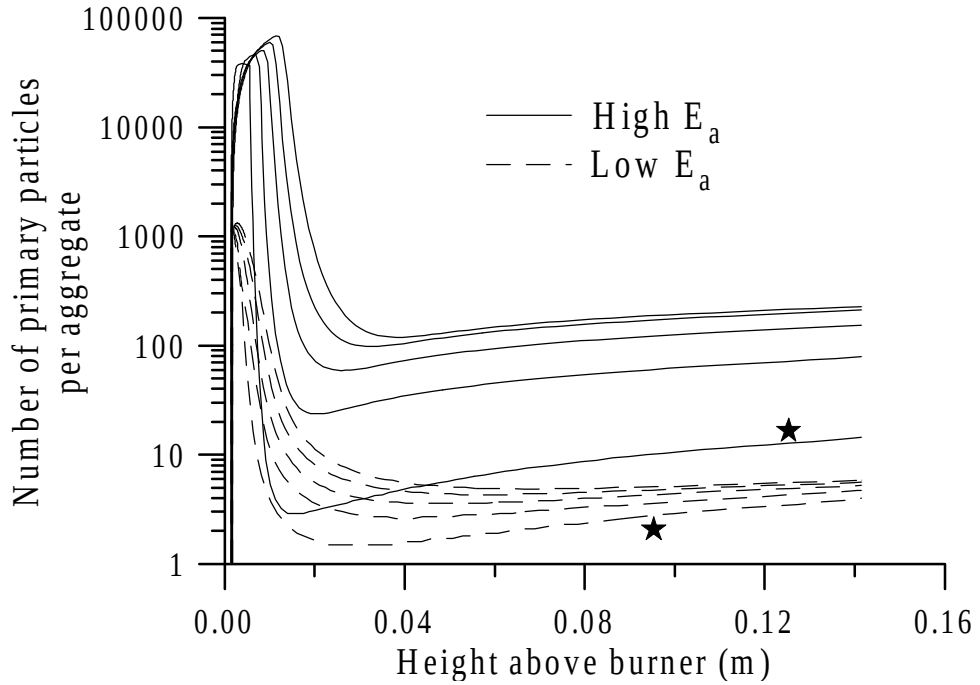

Figure 8 *For the two different activation energy levels, the number of primary particles is shown as a function of height along the five particle trajectories for flame B3. The trajectory corresponding to the most dispersed particles is marked with a "⋆". The temperature curves are shown on figure 8.1.*

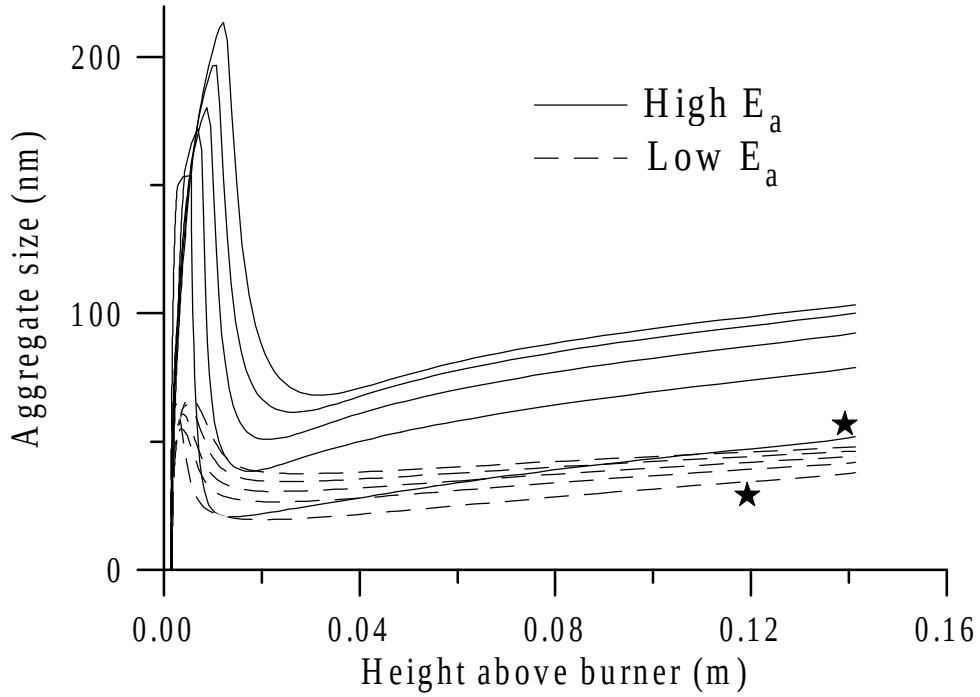

Figure 8 *For the two different activation energy levels, the aggregate size (the collision diameter) is shown as a function of height along the five particle trajectories for flame B3. The trajectory corresponding to the most dispersed particles is marked with a "⋆". The temperature curves are shown on figure 8.1.*

Figure 8.1 shows the temperature as a function of height along the five trajectories, which apart from the difference in temperature also have different dilution histories. There is a significant difference between the temperatures along the five trajectories. The outermost trajectory, which is marked with a star, is closer to the reaction zone and the temperature of this trajectory is therefore higher in some regions compared with the centre profile.

Figures 8.2, 8.3 and 8.4 show plots of the primary particle size, the number of primary particles per aggregate and the aggregate collision diameter respectively.

The initial conditions for the particle monomers correspond to the molecular volume of alumina and a number concentration based on a mole fraction of 0.004 (cf. Appendix C).

In figure 8.2 we see that the high activation energy, E_A, enhances the difference between trajectories. For the high activation energy, the final degree of coalescence is determined by the peak temperature, but for the low activation energy process it is more influenced by the residence time. For the low E_A, the primary particles grow almost throughout the entire region. In the high E_A case, the growth only takes place in the high temperature regions and the high dispersion trajectory yields the largest primary particle.

The number of primary particles per aggregate (cf. figure 8.3) is extremely high just above the burner due to the high initial concentration of small particles, which rapidly coagulate and form large aggregates when the coalescence rate is low. When the coagulation rate decreases and the coalescence rate increases, the number of particles per aggregate decreases as the size of the primary particles increases. Closer to the process outlet, the number of primary particles per aggregate increases again, due to a decrease in the coalescence rate at the lower temperatures while the coagulation rate is still rather high. The particle dynamics at the two different E_A levels have the same qualitative appearance. However, for the high E_A process, the number of particles per aggregate reaches a much higher level during the initial low temperature phase when the coalescence is slow.

From the connection between the primary particle size, the fractal dimension and the number of primary particles per aggregate [cf. equation 3.7], the aggregate collision diameter can be computed. The evolution of the aggregate size along the trajectories is shown on figure 8.4. These curves are similar to those of the number of primary particles per aggregate. The increase of collision size in the initial phase, however, is not as drastic as the increase in the number of particles per aggregate because the primary particles initially are very small.

Figure 8.5 shows the dilution of the particulate matter along the five trajectories for two different

flame cases: B3 and C1. We clearly see that when the air flows in the annulus next to the precursor, flame B, a more efficient dilution is obtained. Flame C has the methane next to the precursor jet, which results in a slower dilution. For both flame types, the dilution occurs fastest at the outermost trajectory (α=0.9).

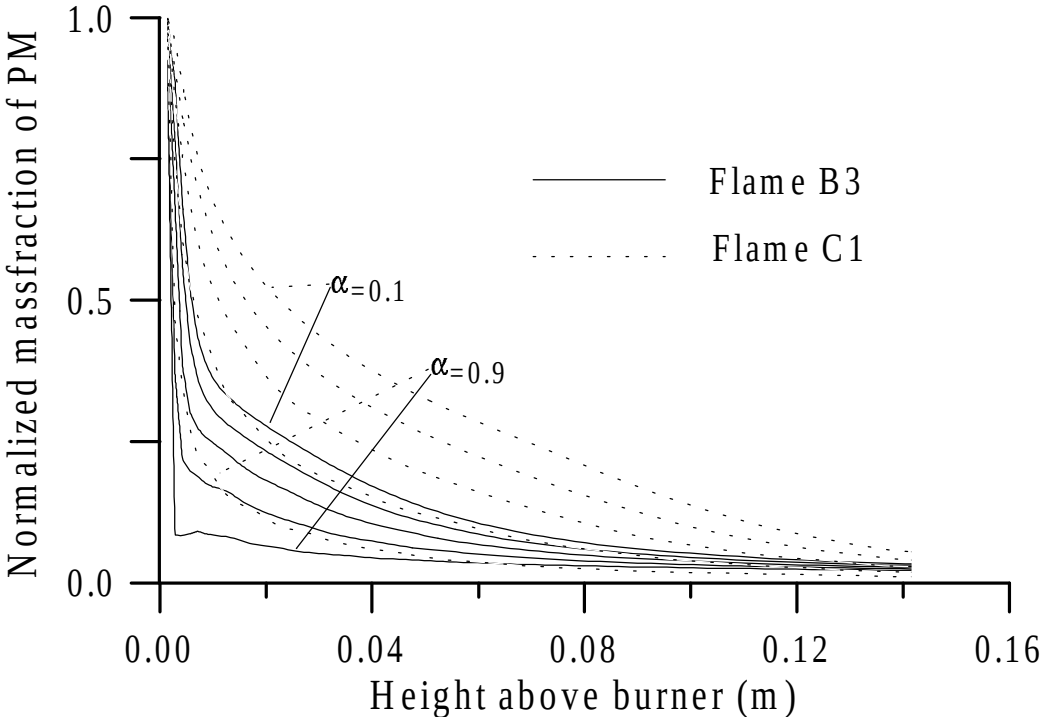

Figure 8 *For flames B3 and C1, the dilution of particulate matter along the trajectories is shown. Flame B3 has a more effective dilution caused by the high air flow in the annulus next to the precursor jet. For both flames, the dilution of the outermost trajectory (α=0.9) is more rapid than the inner trajectories.*

These calculations show the basic behaviour of the model. The necessity of choosing several trajectories in a system with radial dispersion is obvious. For the high activation energy coalescence process, the variation of particle properties between the individual trajectories is significant. The low temperature activated process blurs the effect because the coalescence rate depends more on the residence time than on temperature.

8.2 Diffusion flame simulations

The only unknown parameters in the particle dynamics model are the sintering rate constant k_0 and activation energy E_A of equation 7.21. The two parameter values are estimated by fitting the model to the measured specific surface areas (*SSA*)with a least-squares routine, which minimizes

$$SSQ = \sum_i \left(\ln(S_{A,meas}) - \ln(S_{A,model}) \right)_i^2 \qquad \textbf{(8)}$$

where *i* denotes the twelve measurements of Table 5.1. The value of $S_{A,model}$ is calculated as the mean value of $a/(\rho_p v)$ at the outlet of the computational domain. The mean value is obtained from equation 7.27 after integration of the particle dynamics model along five trajectories with α =0.1, 0.3, 0.5, 0.7, and 0.9, respectively. Logarithmic values are used to ensure that experimental points with large difference in *SSA* are equally weighed in the fitting procedure. The model is solved iteratively under the control of a modified Marquard routine (Fletcher, 1971). The derivatives of *SSQ* with respect to the estimated parameters, which are required in each iteration step by the Marquard code, are computed by numerical perturbation of the particle dynamics model. The initial conditions for the particle volume, surface area and number concentration are calculated from the assumption that the solid oxide is instantly released as monomers. The initial size of the alumina particles are computed from the molecular volume of alumina [cf. Appendix C]. They are considered to be single, spherical Al_2O_3 molecules formed at a given decomposition temperature, T_D = 470 K, approximately 20K above the inlet temperature. The value of T_D affects the final particle characteristics insignificantly as discussed later. However, the chosen value minimizes *SSQ* of equation 8.1. Furthermore, physically it makes sense that the decomposition of the precursor takes place downstream from the jet opening where water and oxygen are present and where the temperature has increased.

Simulations with different values of *m*, which is the power of the particle diameter in equation 7.21, were attempted. A value of $m = 4$ yields a slightly better model fit than $m = 3$, which points to surface or grain boundary diffusion as the most likely coalescence mechanisms. However, the difference is hardly significant enough to discriminate with certainty between the two values of *m*. The following values of the parameters in equation 7.21 were estimated:

Alumina: $\boldsymbol{k_0 = (1.3 \pm 0.3) \times 10^{29}\ m^{-4}s}$ **and** $\boldsymbol{E_A = 68 \pm 12\ kJ/mole}$

based on the following values of the constants in equation 8.1: $m = 4$ and T_0 = 1400 K. The estimated one-σ confidence limits are shown with the parameter estimates. The estimated

standard error in predicting the *SSA* by the model is 10%.

Figure 8.6 shows a graph comparing the different experiments with the simulations using the estimated coalescence parameters. We see, that the basic dependence of the specific surface area on flame configuration is qualitatively reproduced by the simulations. The B-flames yields larger surface areas than the C-flames and high methane flow rate results in low *SSA*. The *SSA* at high methane flow rates, however, is slightly underestimated.

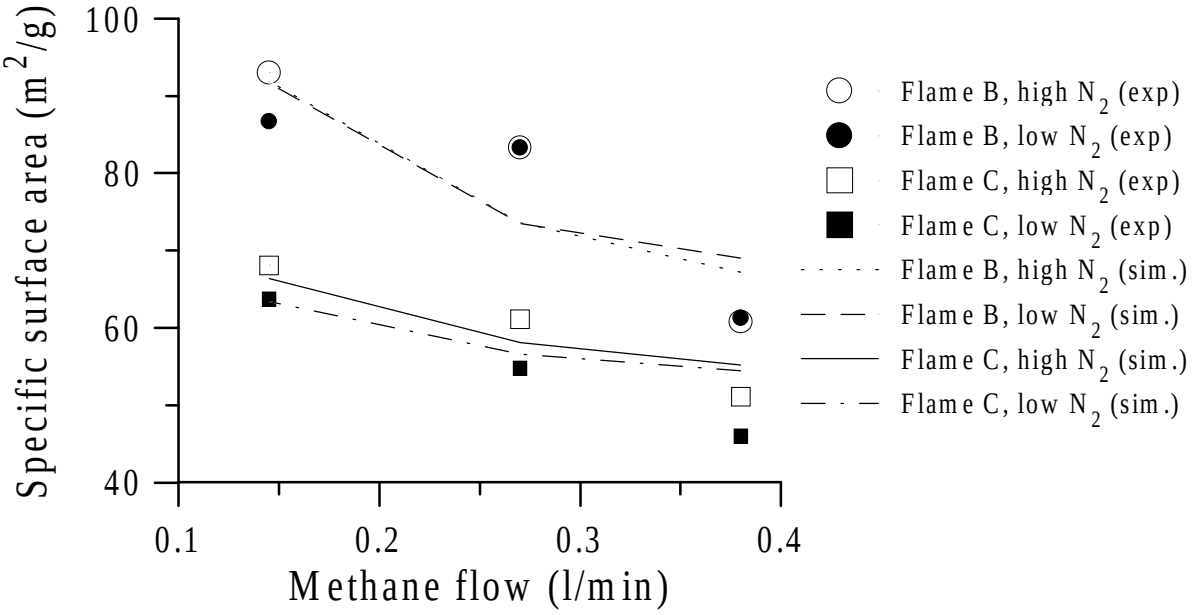

Figure 8 *The points on the graph represent experimental values of the specific surface area (SSA) of the Al_2O_3 particles manufactured in the diffusion flames at the set of operating conditions listed in table 5.1. The lines show simulated values of the SSA for the corresponding operating conditions. For the simulated lines, the pre-exponential factor, k_0, and the activation energy , E_A, for coalescence rate has been fitted using all experimental points.*

Of course, the ambition is to use expressions from one set of flame experiments to predict the particle properties in a different flame process.

We notice that the level of the estimated activation energy is quite low. This causes the variation of the primary particle size between trajectories to be low, similar to the low activation energy case of chapter 8.1. In the alumina simulations with the fitted coalescence expression, the variation of the primary particle size is between 15 and 18 nm for flame B3. Based on the TEM

images of flame B3 in chapter 5.1.5, where the variation of primary particle sizes is significant, we would expect a larger difference between the trajectories. This can be obtained when the coalescence has a higher activation energy, as shown in chapter 8.1. However, the fitting procedure, regardless of initial guesses of E_A and k_0, persistently yields a low activation energy.

8.2.1 The mean aggregate size vs. the aggregate collision diameter

The aggregate collision diameter from the simulations can be compared with the mean aggregate size from the experimental size distributions. The aggregate collision size from the monodisperse model is not directly comparable with the mobility diameter from the SMPS measurements but the two parameters can be assumed to be well within an order of magnitude of each other. In figure 8.7, the variation of the aggregate collision size computed from the simulations agrees reasonably well with the SMPS mean diameter, especially for flame B. However, this graph only serves to validate the implementation of dilution in the coagulation equation in chapter 7.1. Based on this figure, we can conclude that the coagulation and dilution effects agree with the experimental observations.

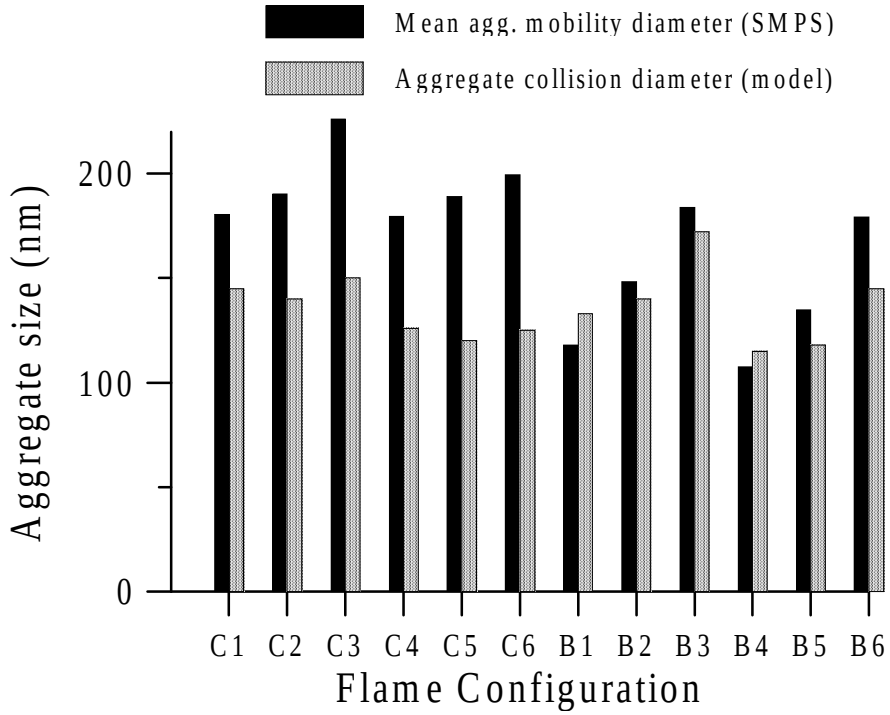

Figure 8 *Measured and simulated Al_2O_3 aggregate sizes plotted for different flame operating conditions. The experimental values are the mean mobility diameters computed from the measured size distributions. The simulated values are based on the aggregate collision diameter in the monodisperse POC-model. Operating condition are listed in table 5.1.*

8.3 Simulation of particle dynamics in the premixed burner

The coalescence parameters obtained from the diffusion flame fit are employed in the simulation of the alumina particles in the premixed burner experiments. The results are shown in table 8.1. When the values are compared with the experimental data, the result is disappointing.

The dependence of the *SSA* on the operating conditions is in qualitative agreement with the experiments concerning highs and lows but the numerical values differ for some of the cases by a factor of three. The surprising part is that the predicted values of specific surface area are quite close to the range of values obtained in the diffusion flames. Furthermore, the simulations predict a stronger dependence of operating conditions, i.e. the jet velocity and quenching, on the *SSA* than observed in the experiments.

Table 8.1. *The specific surface area from the premixed burner experiments are compared with the simulation results obtained by employing the fitted coalescence parameters from the diffusion flame experiments.*

Specific surface area, m*2*/g	P1	P2	P3	P4
Experimental	-	187	153	161
Simulation	55	125	44	62

Essentially the same results are seen when the other models for coalescence [cf. figure 7.2 on page 91] are employed with the same level of activation energy. Possible reasons for the unexpected simulation results are discussed in the next section.

8.4 Comparing the characteristics of trajectories in the diffusion flame and the premixed burner

In table 8.2, the specific surface area measurements are summarized. In this data set, two experimental trends are not reproduced by the simulations:

- The specific surface areas obtained in the premixed burner are consistently larger compared with the diffusion flame experiments.
- The quenching has little effect on the measured specific surface area in the premixed burner.

Table 8.2. *A summary of specific surface areas obtained in the experiments. Flames B and C are*

the diffusion flames and P are the premixed flames. Operating conditions are listed in tables 5.1 and 5.2. All values below are in m^2/g.

C1	C2	C3	C4	C5	C6	B1	B2	B3	B4	B5	B6
51	61	68	46	55	64	61	83	93	61	63	87

P1	P2	P3	P4
-	187	153	161

From the simulations of the two burners, we can compare the temperature as a function of time along the trajectories. Such a comparison, which is an expedient method for comparing the different flames, is shown on figure 8.8. Here, several trajectories are shown for each of the flames B1, C1, P1 and P3. The diffusion flames B1 and C1, with high methane flow rate, have higher trajectory peak temperatures than the premixed cases P1 and P3. For P1 we see the most rapid increase in temperature due to the high jet velocity in configuration P1.

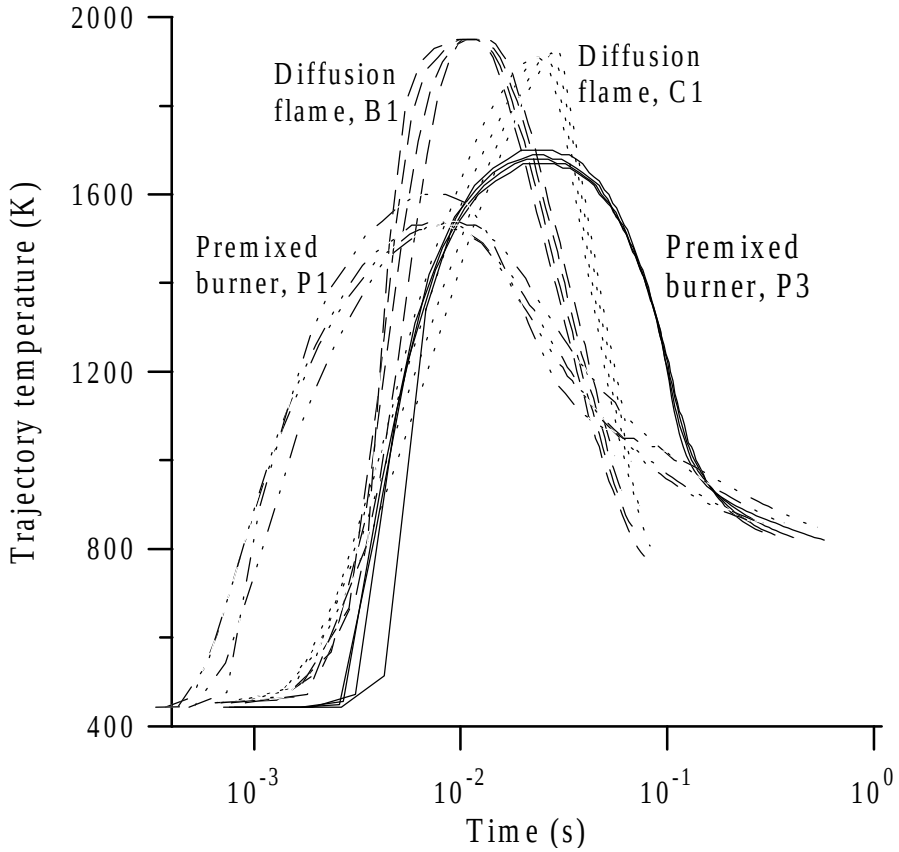

Figure 8 *Particle trajectories for diffusion flames B1 and C1 and the premixed flames P1 and P3. For each flame, the temperature as a function of time along each trajectory is plotted. For flames B1 and C1 the trajectory peak temperature is higher than the premixed flames for all trajectories from each flame.*

On figure 8.9, we see the same type of comparison, but now for the low methane-flow diffusion flames B3 and C3 and the premixed case P3. Here, flame C3 still shows a higher peak temperature than the premixed case but B3 shows lower peak temperatures for all trajectories and each trajectory is at high temperature level for a shorter period of time than P3. Based purely on the simulations of the trajectory temperatures in figure 8.9, it seems impossible that the experimentally measured surface area of P3 is 50% larger than B3. There is no obvious explanation for the inconsistency between the model and the experimental data.

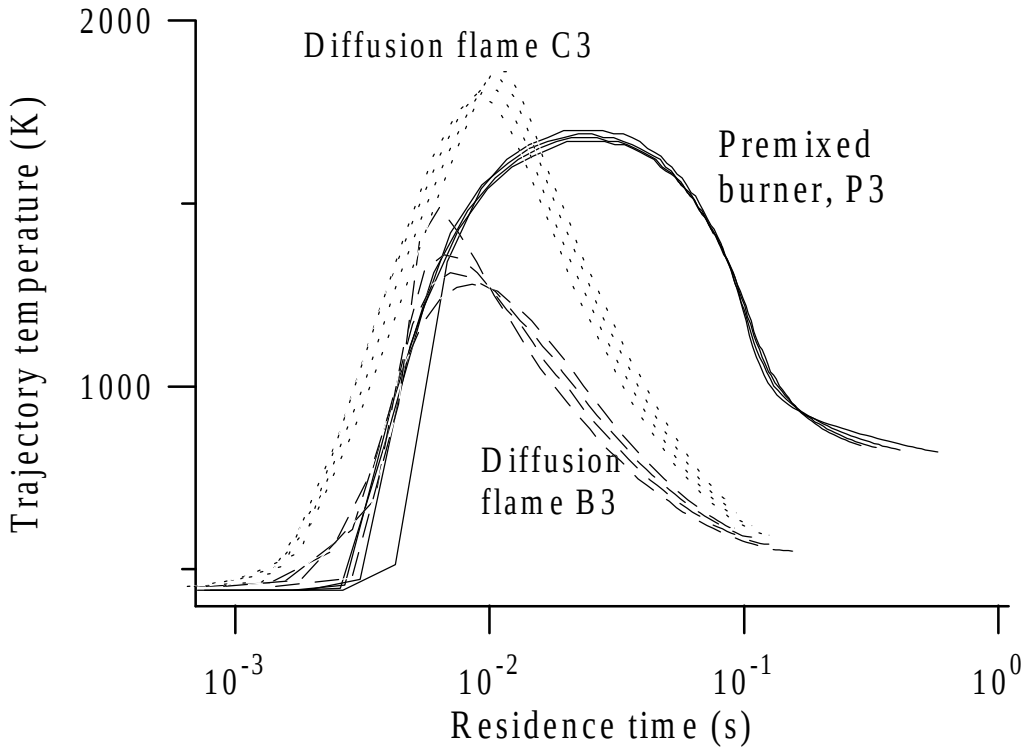

Figure 8 *Particle trajectories for diffusion flames B3 and C3 (low methane flow rate) and the premixed flames P3 (low jet velocity, no quench). For each flame, the temperature as a function of time along each trajectory is plotted. For flame B3, the temperature as well as residence time at high temperature is considerably lower than for P3. This is inconsistent with the observation of a lower specific surface area for B3 than P3.*

However, some possibilities are discussed below:

- The coalescence of alumina particles is a process that might be too complex to be described by an expression with a constant activation energy. Alumina can exist in many phases. Therefore, it is unlikely that the initially formed amorphous aggregates in the low temperature

region will coalesce by the same temperature activated process as the crystalline material, which later in the process has passed through temperature levels close to 2000K.

- The temperature trajectories of all diffusion flames, except the low methane-flow double diffusion flames (B3 and B6), have higher peak temperatures than the premixed cases, P1-P4. A consistent explanation for the higher surface area of the premixed flames can be connected with the temperature profiles of flames B3 and B6. The simulations of B3 and B6 are the most likely to be inaccurate because of the very heterogeneous structure of those flames [cf. figure 6.4]. For example, if the radial dispersion is underestimated, then a larger fraction of the particle mass will pass through higher temperature zones closer to the combustion zone. Thereby, the simulations would yield higher coalescence rates and thus larger surface areas for flames B3 and B6 than presently obtained in the simulations. The fitting of parameters would then result in a higher activation energy for the coalescence expression. This further causes the simulated specific surface area of the premixed cases, where the trajectories have lower peak temperatures, to increase well above level of all diffusion flames.

However, this is merely speculation, which has to be verified by a specially designed set of experiments.

The other unexpected result is the low effect of quenching on the specific surface area in the premixed flames. In figure 8.10, we compare the trajectories for the premixed flames P1 and P2, which are the cases with high jet velocity, no quench and with quench respectively. The quenching causes the trajectories to be more different in terms of peak temperatures, but for all computed trajectories, we see a high cooling effect and much lower peak temperatures. So why does the quenching show little effect on the specific surface area? A possible explanation is the large eddy formation below the quenching point, which is seen in the temperature contour plots of figure 6.9 on page 79. Because of the turbulence, some particles will rapidly pass through the quenching zone following the net flow of gases. However, some particles will be dispersed into the large eddies and remain there for a longer period of time. Eventually, they are dispersed to trajectories leaving the flame zone. In this case, the residence time of particles might be much higher than the time scale of figure 8.10. During this increased residence time, additional coalescence is possible. Still, the temperature in the quenching zone might be insufficient for an increase in primary particle size above the level of the experiments with no quenching.

Some experimental data support this hypothesis. The change in primary particle size from P3 to P4 is insignificant. However, a change in alumina phase was observed [chapter 5.2.3] from slight

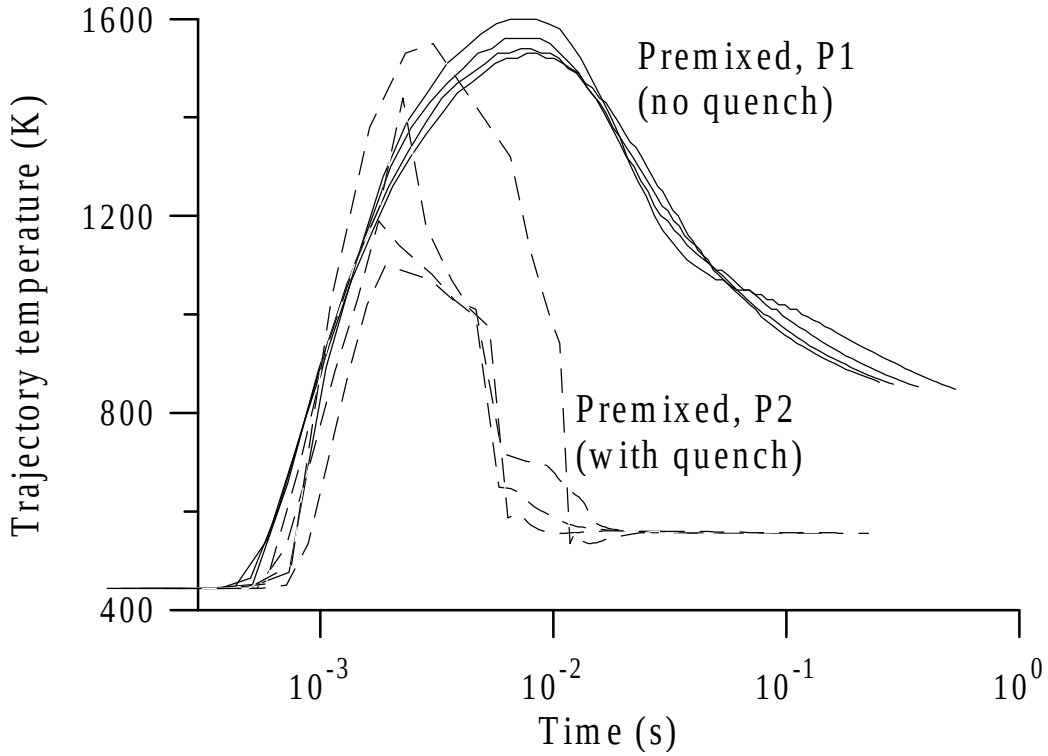

Figure 8 *Particle trajectories for premixed flames P1 (high jet velocity, no quench) and P1 (high jet velocity, with quench). For each flame, the temperature as a function of time along each trajectory is plotted. The quenching is seen to greatly affect the simulated trajectory temperatures. The specific surface area, however, is not as dependent on the quenching as would be expected from these curves.*

crystalline for P3 to amorphous material in P4 where quenching is active. The increased residence time for the aggregates in the large eddies causes the primary particle size to increase slightly but no change in crystallinity takes place due to the lower temperature in the eddy recirculation zone. This phenomenon is too complex for the current particle trajectory model.

In the continuing work, the simulation tools developed in this work will be employed in the design phase of a novel quenching device with minimized eddy formation. Based on the observations in this study, a possible modification is to change the angle of the quenching nozzles from horizontally to pointing slightly upwards, say 10 degrees. This would increase the upwards momentum of the gases and reduce the formation of a central stagnation point with downwards transport of a major fraction of the quench gases.

8.5 Applying the model for the production of titania in diffusion flames

The applicability of the approach to particle simulation developed in this study is investigated by use of experimental data from titania particle production in a different diffusion flame burner. In the experiments by Pratsinis et al. (1996), the diffusion flame burner is similar to the one used in this study, but with different dimensions: Central tube: ID = 4 mm (2mm in this study), the spacing between successive tubes is 1 mm (as in this study) and wall thicknesses of glass tubes are 1mm (as in this study).
In these experiments (Pratsinis et al. ,1996), all four flame configurations shown in figure 5.1 are employed. The operating conditions of the titania experiments are listed in table 8.3.

Table 8.3. *Operating conditions for the TiO_2-flame experiments by Pratsinis et al. (1996). For all conditions the methane flow rate was 0.312 l/min and the argon flow through the $TiCl_4$ bubbler was 0.25 l/min, corresponding to $5.8 \cdot 10^{-4}$ mole $TiCl_4$/min.*

Flame	A1	A2	A3	B1	B2	B3
Air (l/min)	2.5	3.8	5.5	2.5	3.8	5.5
Flame	C1	C2	C3	D1	D2	D3
Air (l/min)	2.5	3.8	5.5	2.5	3.8	5.5

A computational grid, similar to the one showed on figure 6.2 but with the new tube dimensions, is created and the CFD simulations are carried out with the same methane reaction-rate parameters as listed in chapter 6.
The resulting temperature contours for the flames with an air flow rate of 3.8 l/min are seen on figure 8.11. Flames B and C correspond completely to the flame structures of the alumina flames in this study. In flame A, the air flows with the precursor in the central tube. In flame D, the methane flows in the central tube with the precursor. For flame A, the resulting jet velocity is significantly higher than for the three other configurations.
The experimental data for the measured *SSA* are shown on figure 8.12.

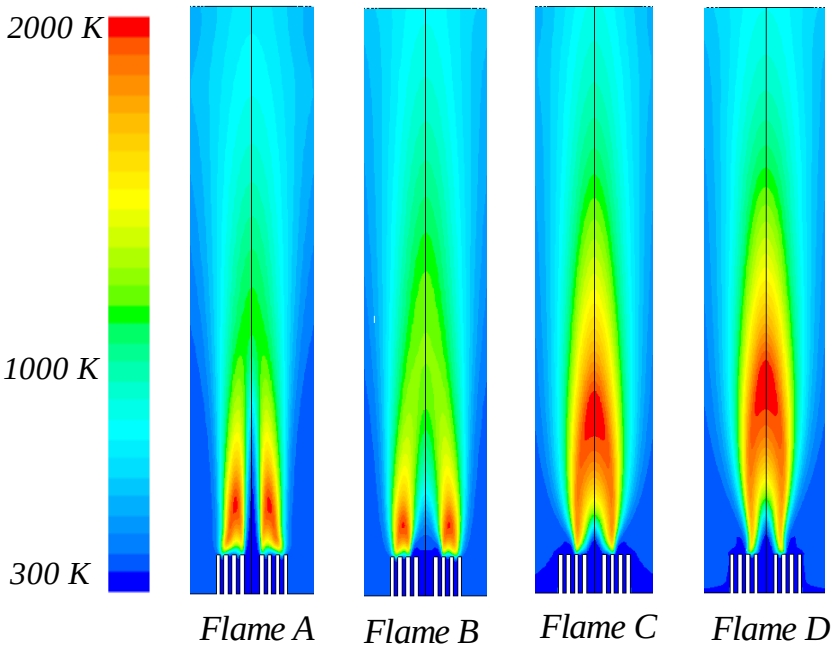

Figure 8 *Simulated temperature contour plots of TiO_2 flames based on experimental conditions from Pratsinis et al. (1996). The four cases are: A2, B2, C2, D2. The operating conditions are listed in table 8.3 and the flames configurations are shown on figure 5.1. The flame structures of the four configurations are highly different. A and B are double diffusion flames while C and D are single diffusion flames.*

When a given literature expression for the coalescence of titania (e.g. Yang and Biswas, 1997) is employed in the simulations, the trends of the simulations match the experimental data but an inadequate quantitative agreement is obtained.

As for the alumina simulations, the two coalescence parameters are estimated by fitting the model to the measured specific surface areas using equation 8.1. Logarithmic values are used to ensure that experimental points with large difference in *SSA* are equally weighed in the fitting procedure. The initial conditions for the particle volume, surface area and number concentration are calculated from the assumption that the solid oxide is instantly released as monomers. The initial size of the titania monomers are computed from the molecular volume of titania [cf. Appendix C]. They are considered to be single, spherical TiO_2 molecules formed at a given decomposition temperature, T_D = 340 K, approximately 20K above the inlet temperature. The value of T_D affects the final particle characteristics insignificantly, but the chosen value minimizes *SSQ* of equation 8.1. As for alumina, it makes sense that the decomposition of the precursor takes place downstream from the jet opening where water and oxygen are present and

where the temperature has increased. The following values of the parameters in equation 7.21 were estimated:

Titania: k_0**=(5.5±7.5)×10^{27} m^{-4}s and** E_A**=148±35 kJ/mole**

based on the following values of the constants in equation 7.21: m = 4 and T_0 = 1400 K. The estimated one-σ confidence limits are shown with the parameter estimates and the estimated standard error in predicting the *SSA* by the model is 30%. The standard error on the predicted values for titania particles is larger than the results obtained with alumina. This is also seen on the large confidence intervals on the estimates, especially k_0.

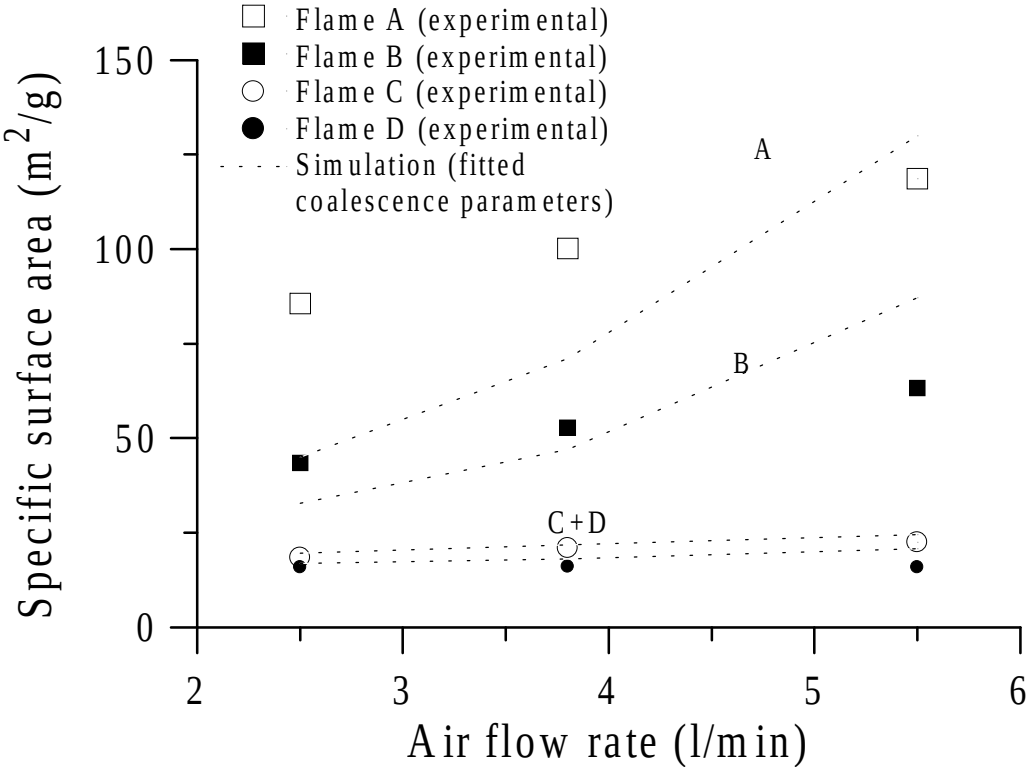

Figure 8 *Experimental data (symbols) from TiO_2 powder made in different flames (taken from Pratsinis et al., 1996). Experimental conditions are summarized in table 8.3 and the flame configurations are shown on figure 5.1. The corresponding simulations are obtained by fitting the coalescence parameters to the experimental data. The trend of the simulations agrees very well with the trend of the data points.*

The obtained values for the *SSA* computed by the model based on these coalescence parameters are shown on figure 8.12. When the large variation of flow rates and the change in flame configuration is taken into consideration, the result is a good description of the flame process by use of the fitted coalescence expression.

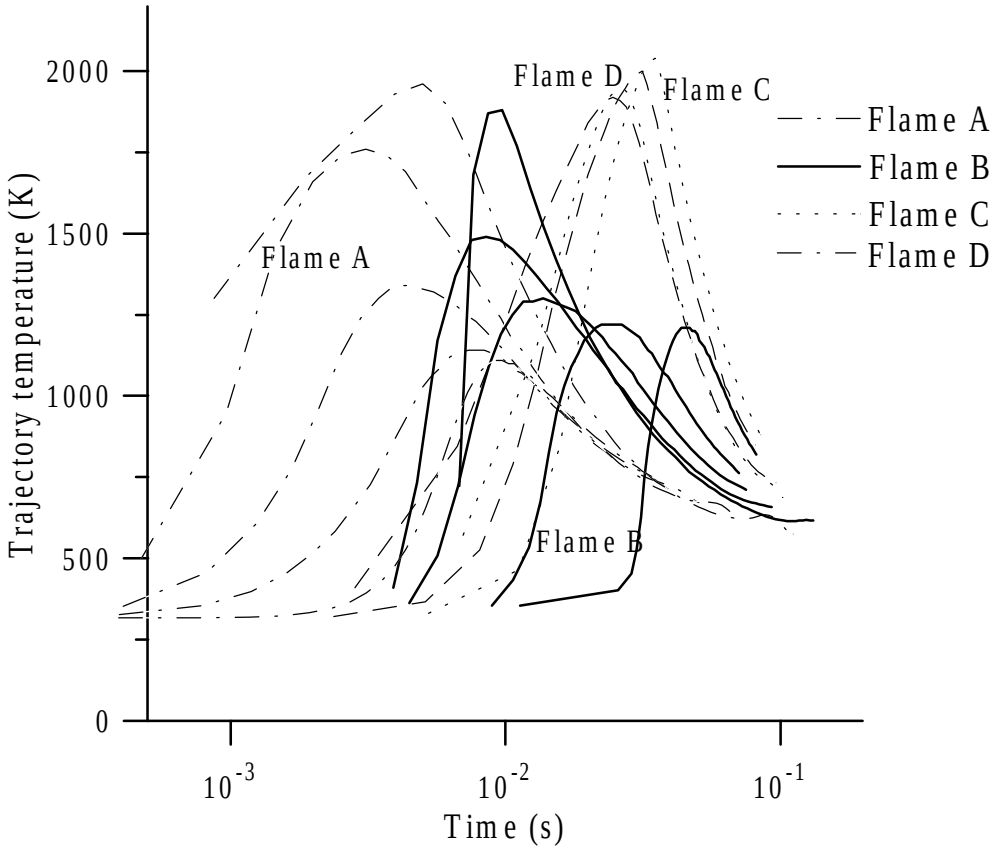

Figure 8 *Particle trajectories for the titania flame experiments A2, B2, C2 and D2 (table 8.3). For each flame, the temperature as a function of time along each trajectory is plotted. From these curves we see a large effect of dispersion for the double diffusion flames (A and B) where trajectories corresponding to high degree of dispersion pass through the hot regions. The single diffusion flames (C and D) have more homogeneous trajectories, which is why only two curves are shown for C and D.*

Figure 8.13 shows time-temperature trajectory plots for the four flames on figure 8.11. For flame A, we see the effect of high jet velocity, which results in short residence time along the trajectories. Flames B, C and D have comparable residence time in the system, but where C and D show very little variation between the individual trajectories (only two are shown for C and D), flame B has a large variation of trajectory temperature as a function of time. Of course, this is a result of the dispersion of particulate matter and the heterogeneous flame structure.

The effect of dispersion on the primary particle size for the simulations of the titania experiments is illustrated in figure 8.14. This figure shows the four flame cases from figure 8.13, where

schematics of the particle trajectories are superimposed on the temperature plots. The resulting primary particle size for each trajectory in each flame is shown on the right-hand side of figure 8.14. In flames C and D, we obtain the largest particles but with some radial variation. For flames A and B, the largest particles are found in the trajectories away from the centre axis whereas the opposite is the case for flames C and D.

The variations of primary particle sizes with trajectories seem quite complex for flames A and B. Especially for flame A, where there is a maximum around trajectory 3 and 4. This is due to the complex relationship between temperature and dilution. For the double diffusion flames A and B, the mixing of particulate matter with the air is effective, and the outer trajectories quickly become very diluted. Thus the primary particle size is not only determined by the rate of coalescence, but also on the rate at which the total mass of each aggregate increases. The primary particles cannot increase in size beyond the corresponding spherical particle with the same particle mass. Therefore, the rate determining step in primary particle growth in the diluted regions of the flame is not only the coalescence rate but also the collision rate.

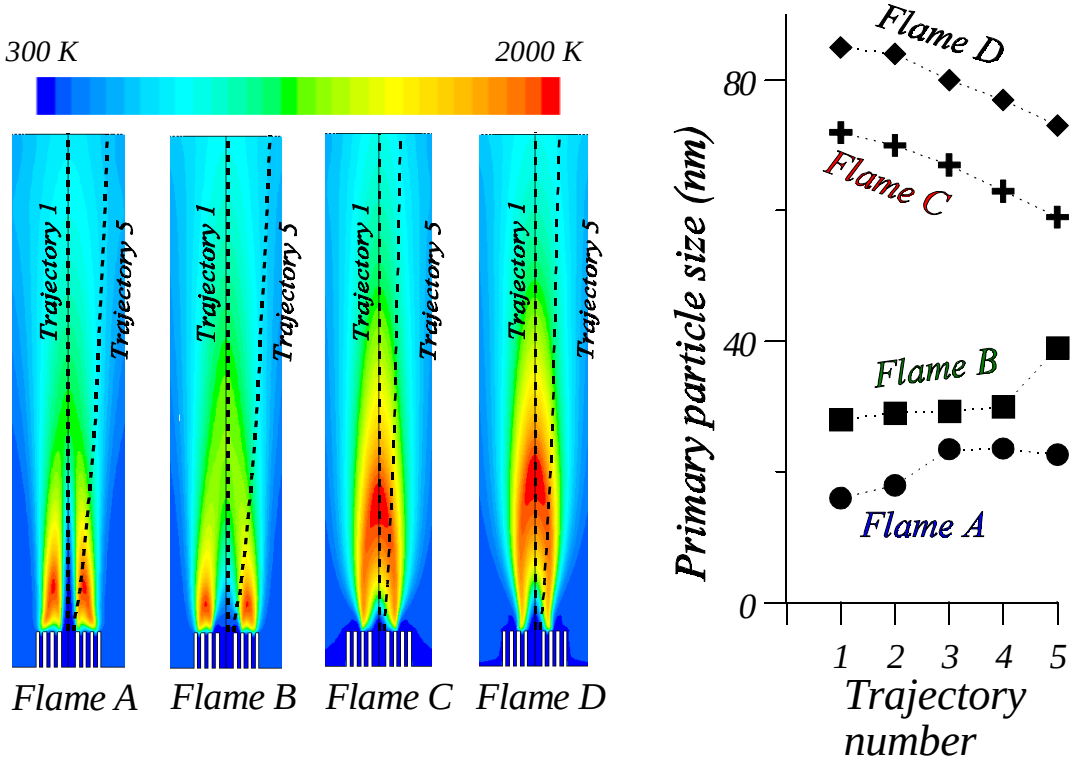

Figure 8 *For the titania flames A2, B2, C2 and D2 (cf. table 8.3), the variation of primary particle size between different trajectories within each flame is shown. Trajectory "1" and "5", corresponding to α=0.1 and α=0.9, are superimposed on each temperature contour plot to illustrate the variation of temperature along the trajectories.*

8.6 Characteristics of simulations for titania vs. alumina

To illustrate the qualitative differences between the results obtained for alumina and titania, two flame cases are compared:

- Alumina, flame B3 (cf. table 5.1 and figure 6.4)
- Titania, Flame B2 (cf. table 8.3 and figure 8.11)

When the following graphs are observed, one must keep in mind, that the initial concentration of particle monomers is higher for the titania flames than for the alumina flames. The initial molefraction of the titania precursor is approximately twenty times larger than the initial molefraction of the ATSB. All simulations are carried out with the coalescence parameters obtained in the fitting procedures. Five trajectories are used in each flame.

For each flame, the five temperature trajectories are shown on figure 8.15. Since both flames are double diffusion flames, the highest temperature is found away from the axis (α=0.9). Figure 8.16 shows the number of primary particles per aggregate along each trajectory. Especially for the center trajectory (α=0.1) in the titania flame, there is an enormous increase of n_p just above the burner. This is due to the low temperature, which inhibits coalescence. In addition to this, the innermost trajectory is slowly diluted, which results in a high coagulation rate. The physical interpretation of this is that once the monomers are formed from the decomposition of the precursor, large amorphous aggregates of non-coalesced monomers are formed. This can be compared with an initial formation of a large snowflake, which transforms into an ice cube. The rapid decrease in n_p initiates when the temperature increases and coalescence commences. For the alumina flame, the intermediate peak is less significant. In both cases, n_p drops several orders of magnitude after the peak has been reached and then increases again in the upper part of the burner.

The rapid decrease in n_p after the peak, is coupled with the graph of the primary particle size, d_p (cf. figure 8.17). When the primary particle growth initiates, n_p decreases. For titania, the difference between d_p for the different trajectories is significant. The largest primary particles are obtained in the $\alpha_{0.9}$-trajectory. The results for the titania flame B2 were also shown on figure 8.14. As discussed in section 8.2, the low activation energy obatined in the alumina simulations results in a residence time determined particle growth and the sizes of primary particles from separate trajectories are almost identical.

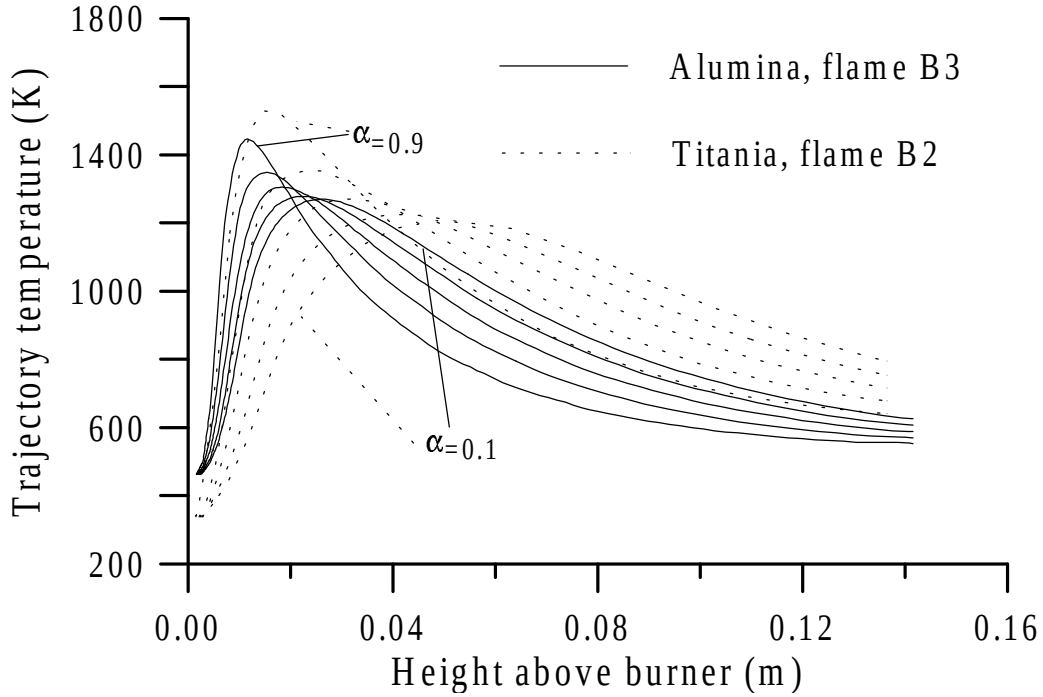

Figure 8 *The variation of temperature along trajectories for two flame cases: Alumina flame B3 (cf. table 5.1)and Titania flame B2 (cf. table 8.3). The simulations are carried out with five trajectories for each flame.*

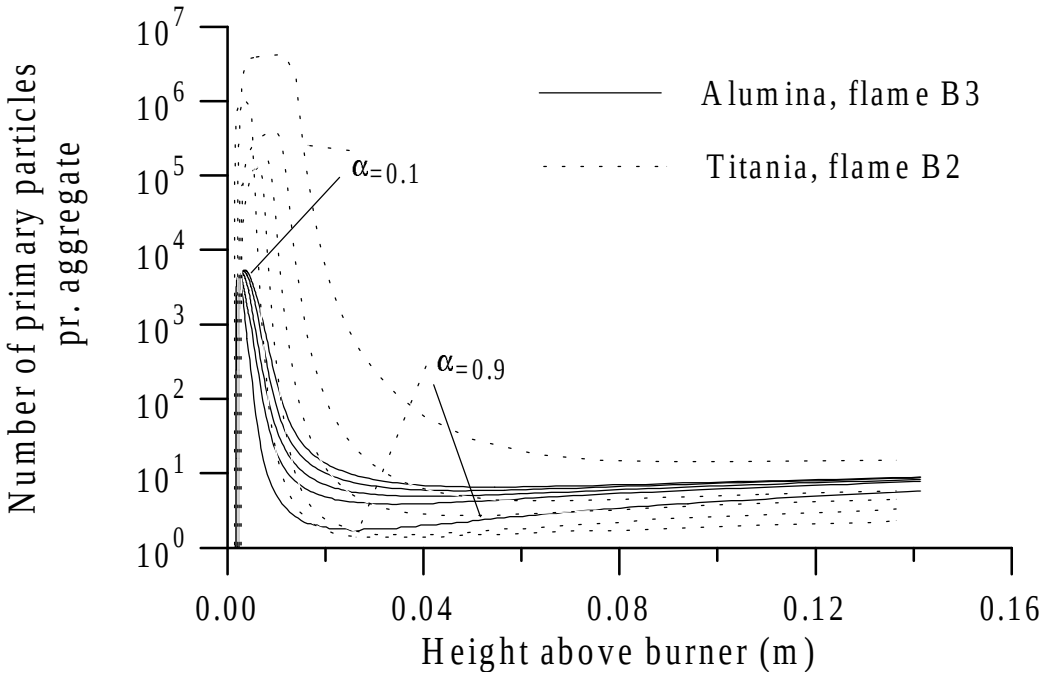

Figure 8 *The variation of the number primary particles per aggregate along trajectories for two flame cases: Alumina flame B3 (cf. table 5.1)and Titania flame B2 (cf. table 8.3).*

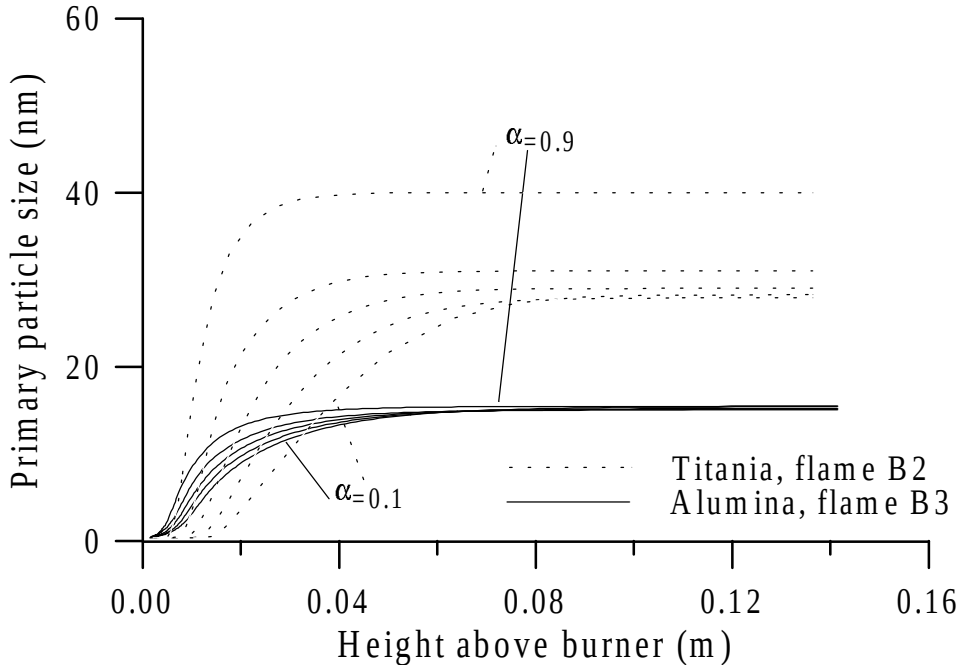

Figure 8 *The variation of the primary particle size along trajectories for two flame cases: Alumina flame B3 (cf. table 5.1)and Titania flame B2 (cf. table 8.3). The final particle sizes for the titania flame can also be seen on figure* 8.14

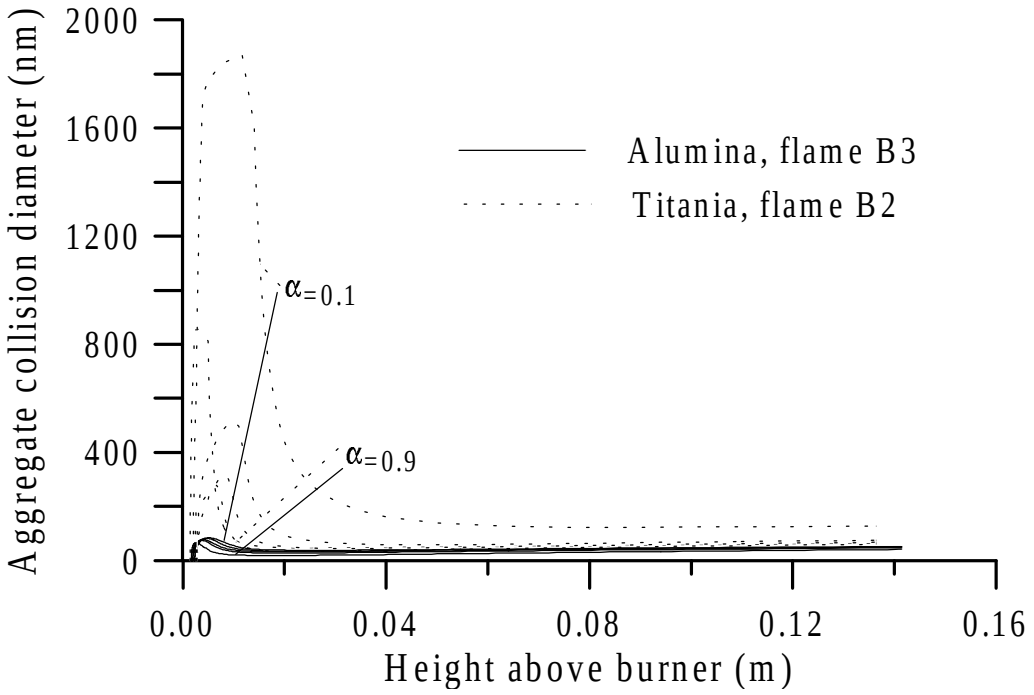

Figure 8 *The variation of the aggregate collision diameter along trajectories for two flame cases: Alumina flame B3 (cf. table 5.1)and Titania flame B2 (cf. table 8.3). The large peak for the $\alpha_{0.1}$ trajectory for the titania flame is caused by the initial high concentration and low temperature.*

The relation between n_p and d_p determines the collision diameter of the aggregates. These results are shown on figure 8.18. The aggregate sizes have the same trends as for n_p. Initially, large clusters of monomers are formed. The coalescence results in more compact aggregates but once the temperature decreases upstream from the flame zone, the aggregates grow again due to pure coagulation. Therefore, the curves for n_p and d_c have a local maximum and also a local minimum.

The model predictions of the huge titania aggregates in the intermediate section of the flame are very interesting. However, testing this experimentally is very difficult. The intermediate size might be overpredicted by the model due to the assumption of instantaneous formation of all monomers at a certain temperature. If the formation of the monomers from the precursor gradually takes places over a short period of time, the burst of newly formed particles will be less drastic and the initial coagulation rate will be lower. However, we would still expect large aggregates in the initial phase when the temperature and hence the coalescence rate are low.

When the results for the two different materials are analysed and compared, we get a valuable insight in the particle formation processes. The parameters for coalescence are extremely important when evolution of particle growth in flames is to be calculated accurately.

8.7 Sensitivity analysis

The value of the decomposition temperature T_D and the fractal dimension D_f are both subject to some uncertainty. The density of the solid particles might also vary significantly due to the difference in crystallinity. Therefore, the sensitivity of the model to changes in these parameters has been studied. The sensitivity of a calculated model variable ϕ towards changes in a parameter ξ is defined as:

$$Sensitivity = \frac{\partial \ln \varphi}{\partial \ln \xi} \qquad \textbf{(8)}$$

Hence, a sensitivity equal to one implies that a fractional change in ξ leads to an identical fractional change in ϕ. The sensitivity of the specific surface area and the aggregate size to T_D, D_f, ρ_p, k_0 and E_A are summarized in Table 8.4 and 8.5.

The sensitivity analysis is based on perturbations of the values of the parameters for the alumina simulations employed in section 8.2 and from appendix C. The sensitivity of the individual parameters varies depending on the parameter value. However, it seems sensible to compute the sensitivity based on the values actually obtained in the simulation/fitting procedure.

Changes in D_f primarily affect the aggregate size but are virtually without influence on the specific surface area. Therefore, the establishment of a proper value of D_f can be linked with measurements of the aggregate size and the value of D_f =1.8 used in the present investigation shows a satisfactory agreement with the measurements (cf. figure 8.7). The decomposition temperature T_D only affects the specific surface area of the double diffusion flames and only to a moderate degree. It has negligible effect on the surface area for the single diffusion flames and on the aggregate size. Evidently, the model is not significantly affected by the uncertainty of T_D and D_f. For all flames, the solid density affects the specific surface area and the aggregate size. This is to be expected, since the specific surface area is computed based on the density. It also influences the aggregate size. In both cases, a higher solid density results in a smaller specific surface area and aggregate size.

The sensitivity to changes in the coalescence parameters, k_0 and E_A, is not significant. This is due to the actual value of the two parameters. A low activation energy makes the coalescence process more residence time dependent. An activation energy level of say 400 kJ/mole would have resulted in a higher sensitivity of the coalescence parameters.

Table 8.4. *Sensitivity analysis: The effect of the decomposition temperature, T_D, and fractal dimension, D_f, on the outlet specific surface area and the aggregate size. The individual elements are computed by equation 8.2.*

	Specific surface area S_A		Aggregate collision diameter d_c	
	T_D	D_f	T_D	D_f
Flame C1	0.06	0.02	-0.15	-1.77
Flame C3	0.02	0.01	0.03	-1.59
Flame B1	0.64	-0.07	-0.12	-1.26
Flame B3	0.36	0.05	-0.04	-2.16

Table 8.5. *Sensitivity analysis: The effect of the solid particle density ρ_p and the coalescence parameters, k_0 and E_A, on the outlet specific surface area and the aggregate size. The individual elements are computed by equation 8.2.*

	Specific surface area S_A			Aggregate collision diameter d_c		
	ρ_p	k_0	E_A	ρ_p	k_0	E_A
Flame C1	-0.81	0.14	-0.10	-0.70	0.10	-0.15
Flame C3	-0.88	0.17	-0.03	-0.55	0.12	0.09
Flame B1	-0.62	0.05	0.04	-0.56	0.18	-0.44
Flame B3	-0.90	0.18	0.30	-0.31	0.17	0.09

The influence of the solid density introduces some unavoidable errors. During the coalescence process, the aggregates will change from initially amorphous clusters of monomers to dense particles with varying degree of crystallinity. Therefore, it is to be expected that the solid density will change up through the flame. In the simulations, a constant density is assumed, which causes some deviation from the real system. This is an issue that must be considered when the accuracy of the model is evaluated. The simulations cannot be expected to be more accurate than the uncertainties involved with the solid density.

8.8 A modified coalescence time: Two simultaneous mechanisms

As discussed earlier, the coalescence of particles/aggregates might be too complex to be described by a single activation energy equation. In this section we investigate a different approach to compute coalescence rates.

Several coalescence mechanisms are described in table 3.1. All of these are in principle active simultaneously but one or maybe two mechanisms may dominate. Surface diffusion in nano-particle aggregates is a mechanism, which differs highly from diffusion in bulk material.

In the following we assume that coalescence takes place by two mechanisms: Surface diffusion and bulk diffusion. Besides a difference in activation energy, the two mechanisms differ in the power of the primary particle size:

$$\tau_{f,s} = k_{0,s} d_p^4 \frac{T}{T_0} \exp\left(\frac{E_{A,s}}{R} \left(\frac{1}{T} - \frac{1}{T_0} \right) \right) \quad \textbf{(8)}$$

$$\tau_{f,b} = k_{0,b} d_p^3 \frac{T}{T_0} \exp\left(\frac{E_{A,b}}{R} \left(\frac{1}{T} - \frac{1}{T_0} \right) \right) \quad \textbf{(8)}$$

Subscript "s" denotes surface and "b" denotes bulk. Compared with the single activation energy equation up to this point, we now have four parameters: $k_{0,s}$, $k_{0,b}$, $E_{A,s}$ and $E_{A,b}$.

In order to reduce the number of new parameters, the bulk diffusion activation energy is fixed. The actual value will be discussed below.

The local coalescence rate is computed as:

$$\frac{1}{\tau_f} = \frac{1}{\tau_{f,s}} + \frac{1}{\tau_{f,b}} \quad \textbf{(8)}$$

When both characteristic times are in the same order of magnitude, both contribute to the overall characteristic time. Otherwise, the fastest of the two mechanisms determines the overall characteristic time.

8.8.1 Applying the two-mechanisms-approach to alumina simulations

The second activation energy, $E_{A,b}$, is fixed at a value close to levels, which are reported in the literature for bulk diffusion of alumina. Wang and Raj (1991) report an activation energy of 440±45 kJ/mole for sintering of pure alumina, whereas Su and Johnson (1996) report a value of 488±20 kJ/mole. The value of $E_{A,b}$ is therefore fixed at 450 kJ/mole. The remaining three parameters of equations 8.3 and 8.4 are fitted to the experimental data for the diffusion flame:

Alumina: $k_{0,s}$ = (8.3±4.5)×10^{29} m^{-4}s, $E_{A,s}$=17±11 kJ/mole, $k_{0,b}$ =(2.1±0.7)×10^{24} m^{-3}s

based on the following values of the constants in equations 8.3 and 8.4: T_0 = 1400 K and $E_{A,b}$ = 450 kJ/mole. The estimated one-σ confidence limits are shown with the parameter estimates and the estimated standard error in predicting the *SSA* by the model is 8%. There is a moderate reduction of the standard error from 10 % for the single activation energy equation (cf. section 8.2) to 8% for the modified expressions in this section. The fitting procedure yields a small activation energy for the "surface" process, which causes it to be active over a large temperature range.

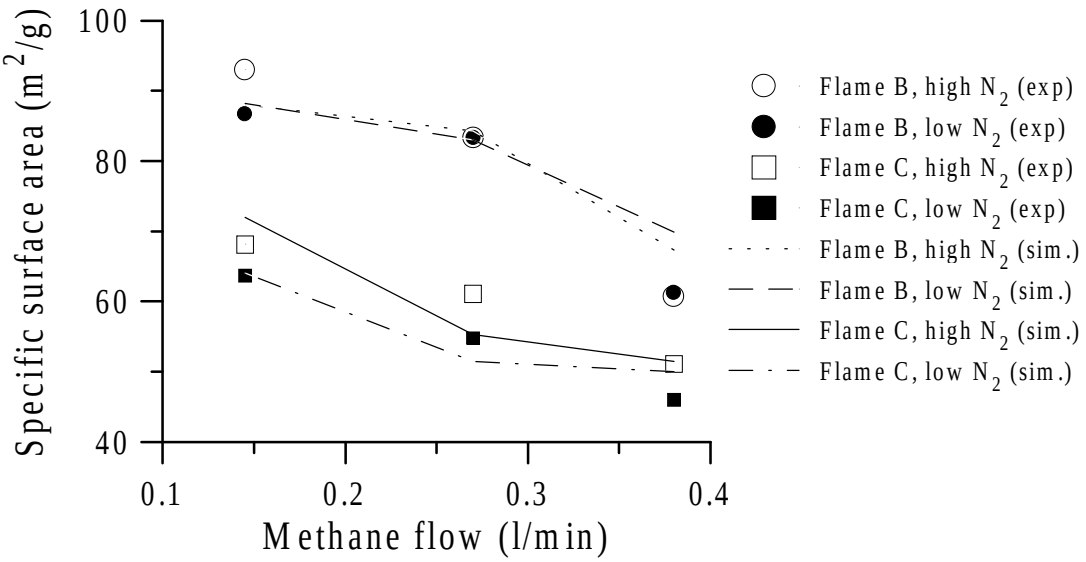

Figure 8 *The points on the graph represent experimental values of the specific surface area (SSA) of the Al_2O_3 particles manufactured in the diffusion flames at the set of operating conditions listed in table 5.1. The lines show simulated values of the SSA for the corresponding operating conditions. For the simulated lines, the two-mechanisms-approach to coalescence is applied.*

Figure 8.19 shows the trend of the simulated specific surface area compared with the experimental data. This graph should be compared with figure 8.6, which shows the original simulations. The effect of introducing the two-mechanisms-approach is a change in the "knee" on the curves of the B-flame simulations. This is an improvement compared with the appearance of figure 8.6. Still, the statistical significance of these results is too small to draw any conclusions.

8.8.2 Applying the two-mechanisms-approach to titania simulations

For the simulation of titania, the second activation energy, $E_{A,\,b}$, is fixed at 265 kJ/mole (Yang and Biswas, 1997). The remaining three parameters of equations 8.3 and 8.4 are fitted to the experimental data for the diffusion flame:

Titania: $k_{0,\,s}$ = (3.4±50)×10^{29} m^{-4}s, $E_{A,\,s}$=28±100 kJ/mole, $k_{0,\,b}$ =(1.7±12)×10^{22} m^{-3}s

based on the following values of the constants in equations 8.3 and 8.4: T_0 = 1400 K and $E_{A,\,b}$ = 265 kJ/mole. The estimated one-σ confidence limits are shown with the parameter estimates and the estimated standard error in predicting the *SSA* by the model is 23%. There is a moderate reduction of the standard error from 30 % for the single activation energy equation (cf. section 8.5) to 23% for the modified expressions in this section. However, the confidence intervals on the estimates are very large. As for alumina, the fitting procedure yields a small activation energy for the "surface" process, which causes it to be active over a large temperature range.
Figure 8.20 shows the change of the model behaviour with the modified coalescence expressions. The original simulations (cf. figure 8.12, section 8.5) are also shown on the figure. The effects on flame C and D are insignificant but the slopes for flames A and B are highly affected. Even though the values of A and B are still not completely in quantitative agreement with the experimental data, the slopes seem to improve. This indicates that the introduction of a low activation energy mechanism yields a better description of the coalescence process in the flame. Further experiments are needed to validate/improve these tests of new coalescence expressions.

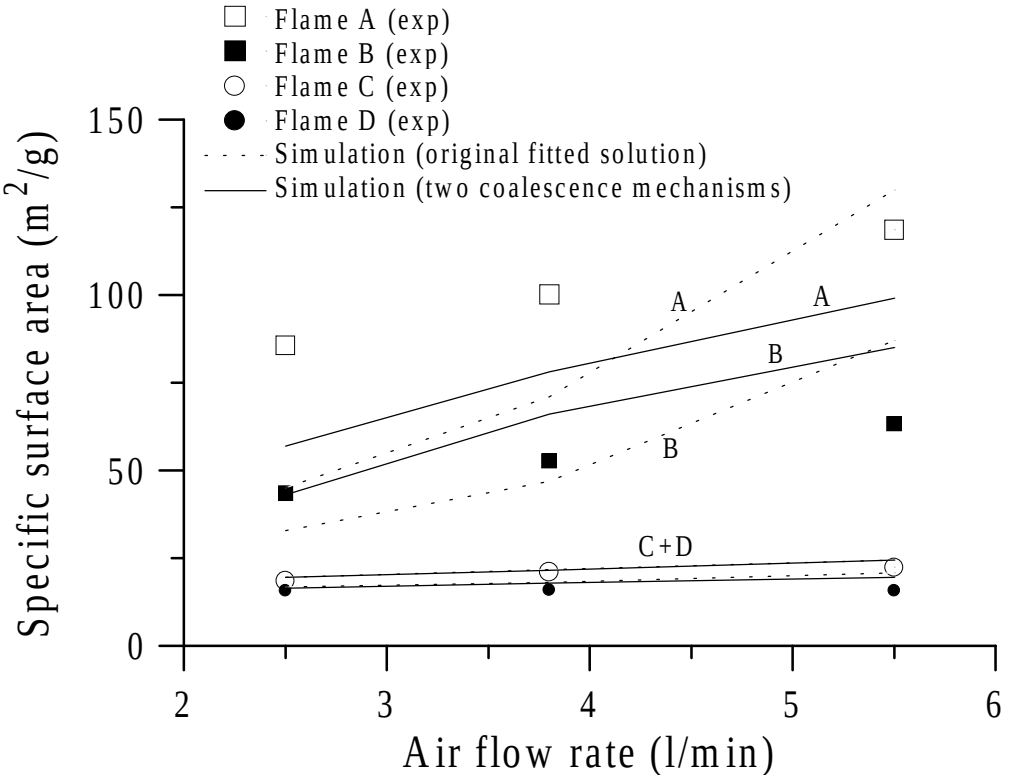

Figure 8 *Experimental data (symbols) from TiO_2 powder made in different flames (taken from Pratsinis et al., 1996). Experimental conditions are summarized in table 8.3 and the flame configuration are shown on figure 5.1. The corresponding simulations are obtained by fitting the two-mechanisms-approach parameters to the experimental data.The original simulations results are shown for comparison. Especially, the slopes of flames A and B are affected by the modification of the coalescence.*

8.9 Comparing characteristic coalescence times

The characteristic coalescence times obtained in this study for alumina and titania are compared in figure 8.21. These curves are the computed based on a primary particle size of 20 nm, i.e. they represent coalescence times for the coalescence of two particles, both 20 nm in diameter.
Also, shown on this graph is the expression obtained by the two-mechanisms-approach.
For both approaches, the coalescence time is higher for alumina, which results in smaller primary particles of alumina at operating conditions identical to titania experiments.
The curves for the two-mechanisms-approach are very different from the single-activation-

energy curves. The latter decrease monotonously with temperature whereas the two-mechanisms curves have two parts: The low and high activation energy level. At low temperature, the surface diffusion term dominates and the high activation energy term dominates at higher temperatures. This modification of the characteristic coalescence time needs to be evaluated by comparison with additional experimental data.

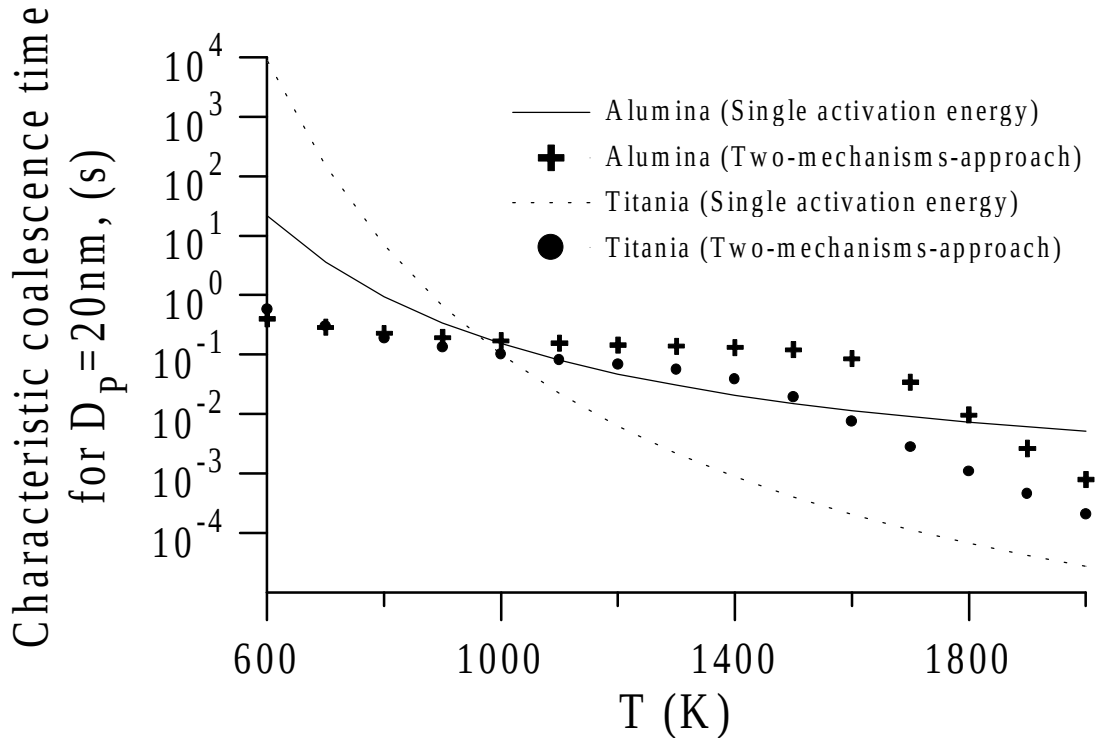

Figure 8 *A plot of characteristic coalescence times as a function of temperature for a the coalescence of two spherical 20nm primary particles. Four curves are shown: The original fitted expressions for alumina and titania and the alumina and titania expressions from the two-mechsniams-approach. The two mechanisms result in a split of the temperature domain. The low actication energy enables coalescence at lower temperatyre whereas the high bulk activation energy influences the coalescence at higher temperatures.*

An additional proposal for discussion and further work is to investigate if any hysteresis effects are involved in the coalescence rate as a function of temperature. It might be possible, that the characteristic time does not follow the same temperature curve in the cooling section above the flame as in the heating section just below the flame. Once the particles to some degree have become crystalline after the initial part of the flame, the coalescence rate might be different when the particle is cooled downstream from the flame tip.

9 Conclusion

The synthesis of nano-metre sized alumina particles from the combustion of Alumina-tri-sec-butoxide in two different burner types is studied. The two burners employed are a diffusion flame burner with the precursor entering the flame zone in a central jet and a premixed flat flame also with a precursor jet. The premixed burner is equipped with a quenching device in order to investigate the effect of rapid cooling/dilution of the product gases on the particle morphology.

The morphology of the produced particles is investigated by TEM bright field images and diffraction images, size distributions measured by an SMPS system and specific surface area measurements. Size distributions are measured by sampling in the flame process with a gas ejector, which rapidly dilutes and cools the sampled gas flow.

The particles formed in the two different flames have specific surface areas between 45 and 95 m^2/g for the diffusion flame and between 150 and 190 m^2/g for the premixed burner. Crystalline phases were clearly seen for the diffusion flame experiments but to very little extent for the particles from the premixed burner. The effect of quenching showed little effect on the primary particle size. Significant radial dispersion of aggregates was found by measuring size distributions at different lateral positions at the process outlet.

The process of particle formation in flames is studied by a novel method where a coagulation/coalescence model is integrated along trajectories describing the dispersion of particulate matter in the flame. Detailed knowledge of temperature, velocity and species concentration distribution in the flames is obtained by solving the basic equations for mass, heat, momentum and species transport in computational grids similar to the physical systems.
By fitting the expression for coalescence using the new approach to aggregate coalescence, the Points-Of-Contact model, a good agreement between simulations and experiments is seen for the diffusion flames. Large deviations are seen when the coalescence expression from the diffusion flame is employed for the simulation of the premixed burner. This is most likely caused by complex phase system for alumina, for which the coalescence probably cannot be described by a single activation energy expression. Furthermore, the difference might be caused by inaccuracies in the numerical simulations of the very heterogeneous double diffusion flames.

The simulation method developed in this study is employed to simulated experimental data of production of titania particles in a different diffusion flame burner. The simulations agree well with the data for large variations of flame configurations and operating conditions.

The new approach to particle dynamics simulation in flames show that there is a significant amount of radial dispersion of particulate matter by turbulent fluctuations. The effect of dispersion on the outlet particle properties depends on the homogeneity of the flame and on the activation energy of the coalescence process.

Future work includes the investigation of the pattern of specific surface areas obtained in the premixed burner and the simulation-based design of a novel quenching device for the premixed flame. Furthermore, by additional experiments, a more accurate description of the dependence of coalescence of alumina particles on the crystal phase and temperature history will be pursued.

References

Bartok, W. and Sarofim, A.F (1991).*Fossil Fuel Combustion,* John Wiley & Sons Inc., New York

Bird, R.B., Stewart, W.E. and Lightfoot, E.N. (1960) *Transport Phenomena,* Wiley, New York

Bolsaitis, P.P., MaCarthy, J.F. and Mohiuddin, G. (1987) Formation of Metal Oxide Aerosols for Conditions of High Supersatuarion, *Aerosol Sci. Technol.*, **6**:225

Cannon, R. M., Rhodes, W. H. and Heuer, A. H., J. Am. Ceram. Soc., 62, 45-53 (1980)

Christensen, K (1995) *The Formation of Submicron Particles from the Combuation of Straw.* Ph.D. thesis, Dept. of Chem. Eng., Technical University of Denmark.

Christensen, P.S, Wedel, S. and Livbjerg, H. (1995) The kinetics of Photolytic Aerosol Formation from SO_2 and NH_3 in humid Air., *Chem. Eng. Sci.*, **49**:24A, pp.4605-4613

Collis D. and Willams M., "Two-dimensional convection from heated wires at low Reynolds numbers", J. of Fluid Mechanics, 6, 357 (1959)

Fletcher, C.A.J (1997) *Computational Techniques for Fluid Dynamics (Sec. ed.),* Springer, New York

Fletcher, R.(1971) A modified Marquard subroutine for non-linear least squares, Harwell Report AERE.6799. (A computer code, VA07, is included in the Harwell subroutine library)

Fluent Inc. (1996). *Fluent: User's Guide*, ***1-4***, Release 4.4, Fluent Incorporated, Centerra Resource Park, 10 Cavendish Court, Lebanon, NH 03766

Friedlander, S.K. (1977), *Smoke, Dust and Haze*. Wiley, New York

Friedlander, S. K. and Wu, M. K. (1994). Linear rate law for the decay of excess surface area of a coalescing solid particle, *Phys. Rev. B*, **49**, 347

Fuchs, N.A. (1964) *Mechanics of Aerosols*. Pergamon, New York

Haanappel, H.D, van Corbach, H.D., Fransen, T. and Gellings, P.J. (1994) The Prrolytic decomposition of aluminum-tri-sec-butoxide during chemical vapour deposition of thin alumina films, *Thermochimica Acta*, **240**, pp.66-77

Handbook of Chemistry and Physics, 1977 (Rober E. Weast, Ed.) CRC Press, Cleveland, Ohio

Hines, J.O. (1975), *Turbulence*. McGraw-Hill Publishing Co., New York, NY

Kaplan, C. R. and Gentry, J. M. (1988). *Aerosol Sci. Technol*., **8**, pp. 11-28 (1988)

Kingery, W. D., Bowen, H. K. and Uhlmann, D. R.(1976) *Introduction in ceramics*, Wiley, New York

Kruis, F.E., Kusters, K.A., Pratsinis, S.E. and Scarlett, B. (1993). A Simple Model for the Characteristics of Aggregate Particles Undergoing Coagulation and Sintering, *Aerosol Sci. Technol.*, **19**, 514

Lehtinen, K.E.J, Windeler, R. and Friedlander, S.K. (1996) A Note on the Growth of Primary Particles in Agglomerate Atructures by Coalescence, *Journal of Collied and Interface Science*, **182**, pp.606-608

Lehtinen, K.E (1997) *Theoretical Studies on Aerosol Agglomeration Processes*, Ph.D thesis, VTT Technical Research Centre of Finland

Lunden, M.M. (1995). *Sintering of agglometares*. PH.D thesis. California Institute of Technology, Pasadena, Ca

Magnussen, B.F. and Hjertager, B.H. (1976), On Mathematical Model of Turbulent Combustion with Special Emphasis on Soot Formation and Combustion, *16th Symp. (Int'l) in Combustion*, Cambridge, MA, Aug. 15-20

Matsoukas, T. and Friedlander, S.K. (1991) Dynamics of Aerosol Agglomerate Formation. *Journal of Collied and Interface Science*, **146**:2, pp. 495-506

Oberlander, R.K. (1984), Alumina for Catalysts. In: *Applied Industrial Catalysis*, Vol. 3 (Bruce E. Leach, Ed.), pp. 63-111, Academic Press, New York

Okuyama, K., Kousaka, Y., Yamamoto, S., Wu, J.J., Flagan, R.C. and Sienfeld, J.H (1986) Production of Ultrafine Metal Oxide Aerosol Particles by Thermal Decomposition of Metal Alkoxide Vapor. *Aiche Journal*, **32**:12, pp. 2010-2019

Peri, J.B. and Hannan, R.B. (1960). Surface Hydroxyl Groups on g-alumina. *Journal of Physical Chemistry*, **72**, pp. 2917-2924

Phillips, W.F. (1975). Drag on a Small Sphere Moving through a Gas, *Phys. Fluids*, **1**, pp. 1089-1093

Pratsinis, S.E. (1998). Flame Aerosol Synthesis of Ceramic Powders. *Prog. Energy Combust Sci.*, **24**, pp. 197-219

Pratsinis, S. E., Zhu, W. and Vemury, S (1996). The role of gas mixing in flame synthesis of titania powders", *Powder Technology*, **86**, 87

Seinfeld, J.H. (1986) *Air Polution*, John Wiley & Sons Inc., New York

Sextl, G., H. Swarowsky, M. Koerfer, P. Kleinschmidt and R. Schwartz (1990), Ger. Offen. DE 4,009,299 (Cl. C01F/30)

Siegel, R. and Howel, J.R. (1992). *Thermal Radiation Heat Transfer*, Hemisphere Publishing Co., Washington D.C.

Sokolowski, M., Sokolowska, A., Michaelski, A. and Gokieli, B. (1977) *Journal of Aerosol Sci.*, **8**, 219

Smith, J.M. and Van Ness, H.C. (1987) *Introduction to Chemical Engineering Thermodynamics*, 4. ed., Mcgraw-Hill, New York

Su, H.H. and Johnson, D.L. (1996) Sintering of alumina in microwave-induces oxygen plasma. *J. of the Am. Ceramic. Soc.*, **79** (12), 3199-3219

Tranto, J. (1997). *Supported Ceramic Membranes for High Temperature Gas Separation*. Ph.D thesis, Dept. of Material Sci., Tech. University of Denmark

Ulrich, G.D. (1971). Theory of Particle Formation and Growth in Oxide Synthesis Flames

Combustion Sci. and Technology, **4**, 47

Vemury, S. and Pratsinis, S.E (1995) *Journal of the American Ceramic Society*, **78**, 529

Villadsen, J. and Michelsen, M.L. (1978). *Solution of Differential Equations by Polynomial Approximation*. Prentice-HAll, New York.

Wang, J.D and Raj, R. (1991) Activation-energy for the sintering of 2-phae alumina zirconia ceramics. *J. of the Am. Ceramic. Soc.*, **74** (8), 1959-1963

Windeler, R.S., Friedlander, S.K. and Lehtinen, K.E.J. (1997) Production of nanometer-sized metal oxide particles in a free jet I: Experimental system and results. *Aerosol Sci. and Technol.***27**, no. 2, pp.174-190

Wu, M.K. and Friedlander, S.K. (1992). Enhanced Agglomerate Growth in the Free Molecule Regime. *J. Aerosol Sci.*, **23** (suppl.1), pp. 71-74

Wu , M. K., Windeler, S. E., Steiner, C. K. R., Bors, T. and Friedlander, S. K. (1993). *Aerosol Sci. Technol.*, **19**, 527

Xiong, Y., and Pratsinis, S.E. (1993) *J. Aerosol Sci.*, **24**, pp.283-300

Yang, G., and and Biswas, P. (1997) Study of the Sintering of Nanosized Titania Agglomerates in Flames Using *In Situ* Light Scattering Methods. *Aerosol Sci. Technol.*, **27**:4, 507-521

Appendix A: Physical parameters for CFD simulations

This appendix serves as a list of physical data as well as data and formulas for computing physical parameters in the CFD simulations. In the following, all variables are used in SI-units unless stated.
The species involved are CH_4, O_2, H_2O, CO_2, N_2 and PM. The species PM is the component, which is used as approximation for particulate matter (alumina) in the simulations.

Aluminum-tri-sec-butoxide

Molar weight: 246.3 g/mole
Vapour pressure (Okuyama et al., 1986):

$$\ln(P[mmHg]) = 23.9 - 9809/T[K]$$

Density

Density is computed from the ideal gas law:

$$\rho_g = \frac{p_{total}}{RT\sum_i \frac{m_i}{M_i}}$$

where p_{total} is the total pressure, m_i is the mass fraction and M_i the molecular weight of species i.

Molecular weights

Species molecular weights:

Species	Molecular weight
CH_4	16.04
O_2	32.0
CO_2	44.01
H_2O	18.02
N_2	28.01
PM*	101.96

* *The value for the PM-component is not important for the CFD simulations due to the low mass fraction of the PM-component. However, the molecular weight for aluminum oxide is assigned the PM-component.*

Lennard-Jones parameters

The Lennard-Jones parameters σ_i [Å] and $(\varepsilon/k)_i$ [K] which are used for kinetic theory of gases (KToG) are listed below:

Species	σ_i **[Å]**	$(\varepsilon/k)_i$ **[K]**
CH_4	3.7580	148.6
O_2	3.4670	106.7
CO_2	3.9410	195.2
H_2O	2.6410	809.1
N_2	3.7980	71.4
PM**	3.7980	71.4

** *The values for the PM-component are not important for the simulations, since the diffusion coefficient for PM is not calculated by KToG. The thermal conductivity and viscosity are computed by KToG, but due to the very low mass fraction of the PM-component, the actual values are without effect on the results. The values for nitrogen are assigned PM as a "default" value.*

Viscosity

Viscosity of the gas mixture is computed from the kinetic theory of gases (Bird et al., 1960):

$$\mu_g = \sum_i \frac{X_i \mu_i}{\sum_i X_i \varphi_{ij}}$$

where X_i is the mole fraction and μ_i the viscosity for species i. φ_{ij} is computed as

$$\varphi_{ij} = \frac{\left[1 + \left(\frac{\mu_i}{\mu_j}\right)^{1/2} \left(\frac{M_i}{M_j}\right)^{1/4}\right]^2}{\left[8\left(1 + \frac{M_i}{M_j}\right)\right]^{1/2}}$$

and the individual viscosities are computed by

$$\mu_i = 2.67 \cdot 10^{-6} \frac{\sqrt{M_i T}}{\sigma_i^2 \Omega_\mu}$$

where σ_i is in Ångstrøm and Ω_μ is a function (listed in table B-2, Bird et al, 1960) of a dimensionless temperature, T^*:

$$T^* = \frac{T}{(\varepsilon/k)}$$

Thermal conductivity

The thermal conductivity of the gas mixture is computed from the kinetic theory of gases (Bird et al., 1960):

$$k_{c,g} = \sum_i \frac{X_i k_{ci}}{\sum_i X_i \varphi_{ij}}$$

where X_i is the mole fraction and $k_{ci'}$ the thermal conductivity for species i. φ_{ij} is computed as

$$\varphi_{ij} = \frac{\left[1 + \left(\frac{k_{ci}}{k_{cj}}\right)^{1/2} \left(\frac{M_i}{M_j}\right)^{1/4}\right]^2}{\left[8\left(1 + \frac{M_i}{M_j}\right)\right]^{1/2}}$$

and the individual thermal conductivities are computed by

$$k_{ci} = \frac{15}{4} \frac{R}{M_i} \mu_i \left(\frac{4}{15} \frac{c_{pi} M_i}{R} + \frac{1}{3}\right)$$

where c_{pi} is the specific heat capacity for species i.

Specific heat capacities

The specific heat capacity for the gas mixture is computed from the KToG mixture rule (Bird et al., 1960):

$$c_{p,g} = \sum_i \frac{X_i c_{pi}}{\sum_i X_i \varphi_{ij}}$$

where $X_{i'}$ is the mole fraction and $k_{ci'}$ the thermal conductivity for species i'. $\varphi_{ij'}$ is computed as

$$\varphi_{ij} = \frac{\left[1 + \left(\frac{c_{pi}}{c_{pj}}\right)^{1/2} \left(\frac{M_i}{M_j}\right)^{1/4}\right]^2}{\left[8\left(1 + \frac{M_i}{M_j}\right)\right]^{1/2}}$$

The individual specific heat capacities are computed as temperature functions from data in Smith and Van Ness (1987).

Diffusion coefficients

Diffusion coefficients are computed from KToG, with exception of the PM-component. The diffusion coefficient for the particles is lower than the coefficient for gases. The diffusion coefficient for PM, D_{PM}, is set to $1 \cdot 10^{-8}$ m^2/s.
For the other species, the diffusion coefficients are computed from the Chapman-Enskog equation (e.g. Bird at al., 1960):

$$D_{ij} = 0.0188 \frac{\left[T^3 \left(\frac{1}{M_i} + \frac{1}{M_j}\right)\right]^{1/2}}{p_{total} \sigma_{ij}^2 \Omega_D}$$

where Ω_D is a function (listed in table B-2, Bird et al, 1960) of a dimensionless temperature, T^*:

$$T^* = \frac{T}{(\varepsilon/k)_{ij}}$$

where

$$(\varepsilon/k)_{ij} = \sqrt{(\varepsilon/k)_i (\varepsilon/k)_j}$$

and

$$\sigma_{ij} = \frac{1}{2}(\sigma_i + \sigma_j)$$

Appendix B: Interpolation method for 2D gridded data: B2INK

AUTHOR: BOISVERT, RONALD, NBS
SCIENTIFIC COMPUTING DIVISION
NATIONAL BUREAU OF STANDARDS
WASHINGTON, DC 20234

REFERENCES: CARL DE BOOR, A PRACTICAL GUIDE TO SPLINES, SPRINGER-VERLAG, NEW YORK, 1978.
CARL DE BOOR, EFFICIENT COMPUTER MANIPULATION OF TENSOR PRODUCTS, ACM TRANSACTIONS ON MATHEMATICAL SOFTWARE, VOL. 5 (1979), PP. 173-182.

Below is the description of the program from the program code, B2INK

```
      SUBROUTINE B2INK(X,NX,Y,NY,FCN,LDF,KX,KY,TX,TY,BCOEF,WORK,IFLAG)

C***DATE WRITTEN   25 MAY 1982
C***REVISION DATE  25 MAY 1982
C***CATEGORY NO.  E1A
C***KEYWORDS  INTERPOLATION, TWO-DIMENSIONS, GRIDDED DATA, SPLINES,
C             PIECEWISE POLYNOMIALS
C***AUTHOR  BOISVERT, RONALD, NBS
C             SCIENTIFIC COMPUTING DIVISION
C             NATIONAL BUREAU OF STANDARDS
C             WASHINGTON, DC 20234
C***PURPOSE  B2INK DETERMINES A PIECEWISE POLYNOMIAL FUNCTION THAT
C            INTERPOLATES TWO-DIMENSIONAL GRIDDED DATA. USERS SPECIFY
C            THE POLYNOMIAL ORDER (DEGREE+1) OF THE INTERPOLANT AND
C            (OPTIONALLY) THE KNOT SEQUENCE.
C***DESCRIPTION
C
C   B2INK determines the parameters of a function that interpolates the
C   two-dimensional gridded data (X(i),Y(j),FCN(i,j)) for i=1,..,NX and
C   j=1,..,NY. The  interpolating  function  and  its  derivatives  may
C   subsequently be evaluated by the function B2VAL.
C
C   The interpolating  function  is  a  piecewise  polynomial  function
C   represented as a tensor product of one-dimensional  B-splines.  The
C   form of this function is
C
C                          NX   NY
C             S(x,y)  =  SUM  SUM  a   U (x) V (y)
C                        i=1  j=1   ij  i     j
C
C   where the functions U(i)  and  V(j)  are  one-dimensional  B-spline
C   basis functions. The coefficients a(i,j) are chosen so that
C
C         S(X(i),Y(j)) = FCN(i,j)   for i=1,..,NX and j=1,..,NY
C
C   Note that  for  each  fixed  value  of  y  S(x,y)  is  a  piecewise
C   polynomial function of x alone, and for each fixed value of x  S(x,
C   y) is a piecewise polynomial function of y alone. In one  dimension
```

```
C   a piecewise polynomial may  be  created  by  partitioning  a  given
C   interval into subintervals and defining a distinct polynomial piece
C   on each one. The points where adjacent subintervals meet are called
C   knots. Each of the functions U(i) and V(j)  above  is  a  piecewise
C   polynomial.
C
C   Users of B2INK choose the order (degree+1) of the polynomial pieces
C   used to define the piecewise polynomial in each  of  the  x  and  y
C   directions (KX and KY).  Users  also  may  define  their  own  knot
C   sequence in x and y separately (TX and TY).  If  IFLAG=0,  however,
C   B2INK will choose sequences of knots that  result  in  a  piecewise
C   polynomial interpolant with KX-2 continuous partial derivatives  in
C   x and KY-2 continuous partial derivatives in y. (KX knots are taken
C   near each endpoint, not-a-knot end conditions  are  used,  and  the
C   remaining knots are placed at data points  if  KX  is  even  or  at
C   midpoints between data points if KX is  odd.  The  y  direction  is
C   treated similarly.)
C
C   After a call to B2INK, all  information  necessary  to  define  the
C   interpolating function are contained in the parameters NX, NY,  KX,
C   KY, TX, TY, and BCOEF. These quantities should not be altered until
C   after the last call of the evaluation routine B2VAL.
C
C
C   I N P U T
C   ---------
C
C   X       Real 1D array (size NX)
C           Array of x abcissae. Must be strictly increasing.
C
C   NX      Integer scalar (.GE. 3)
C           Number of x abcissae.
C
C   Y       Real 1D array (size NY)
C           Array of y abcissae. Must be strictly increasing.
C
C   NY      Integer scalar (.GE. 3)
C           Number of y abcissae.
C
C   FCN     Real 2D array (size LDF by NY)
C           Array of function values to interpolate. FCN(I,J) should
C           contain the function value at the point (X(I),Y(J))
C
C   LDF     Integer scalar (.GE. NX)
C           The actual leading dimension of FCN used in the calling
C           calling program.
C
C   KX      Integer scalar (.GE. 2, .LT. NX)
C           The order of spline pieces in x.
C           (Order = polynomial degree + 1)
C
C   KY      Integer scalar (.GE. 2, .LT. NY)
C           The order of spline pieces in y.
C           (Order = polynomial degree + 1)
C
C
C   I N P U T   O R   O U T P U T
C   -----------------------------
C
C   TX      Real 1D array (size NX+KX)
C           The knots in the x direction for the spline interpolant.
C           If IFLAG=0 these are chosen by B2INK.
C           If IFLAG=1 these are specified by the user.
C                      (Must be non-decreasing.)
C
C   TY      Real 1D array (size NY+KY)
C           The knots in the y direction for the spline interpolant.
C           If IFLAG=0 these are chosen by B2INK.
```

```
C           If IFLAG=1 these are specified by the user.
C                      (Must be non-decreasing.)
C
C
C   O U T P U T
C   -----------
C
C   BCOEF   Real 2D array (size NX by NY)
C           Array of coefficients of the B-spline interpolant.
C           This may be the same array as FCN.
C
C
C   M I S C E L L A N E O U S
C   -------------------------
C
C   WORK    Real 1D array (size NX*NY + max( 2*KX*(NX+1),
C                                 2*KY*(NY+1) ))
C           Array of working storage.
C
C   IFLAG   Integer scalar.
C           On input:  0 == knot sequence chosen by B2INK
C                      1 == knot sequence chosen by user.
C           On output: 1 == successful execution
C                      2 == IFLAG out of range
C                      3 == NX out of range
C                      4 == KX out of range
C                      5 == X not strictly increasing
C                      6 == TX not non-decreasing
C                      7 == NY out of range
C                      8 == KY out of range
C                      9 == Y not strictly increasing
C                     10 == TY not non-decreasing
C
C***REFERENCES  CARL DE BOOR, A PRACTICAL GUIDE TO SPLINES,
C                 SPRINGER-VERLAG, NEW YORK, 1978.
C               CARL DE BOOR, EFFICIENT COMPUTER MANIPULATION OF TENSOR
C                 PRODUCTS, ACM TRANSACTIONS ON MATHEMATICAL SOFTWARE,
C                 VOL. 5 (1979), PP. 173-182.
C***ROUTINES CALLED  BTPCF,BKNOT
C***END PROLOGUE  B2INK
```

Appendix C: Initial conditions for alumina and titania particles

Alumina, Al_2O_3

The decomposition of the precursor is assumed instantaneous once the precursor enters the flame zone and the initial number concentration of alumina monomers is computed as half the initial mole fraction of the precursor, because two precursor molecules yield one Al_2O_3 unit.

The volume of a single Al_2O_3 unit is approximated as a sphere computed from the molecular volume of alumina, which is computed from the density of alumina, 3.97 g/cm^3 (Handbook of Chemistry and Physics, 1997). The value is computed as:

$$v_{mono} = M_{alumina}/(\rho_{alumina}\, N_{Avogadro})$$

The diameter and surface area of an Al_2O_3 unit is computed based on a sphere with the volume, v_{mono}.

Titania, TiO_2

The initial conditions for titania are computed in the same manner, only based on the density of titania, 4.17g/cm^3 (Handbook of Chemistry and Physics, 1997).